Development of Fluorescent Semi-conductor Nanocrystal Conjugates for *in vitro* and *in vivo* Imaging Applications

by

Hee-Sun Han

B.A. Chemistry,
Seoul National University, Seoul, South Korea
2006

Submitted to the Department of Chemistry in
Partial Fulfillment of the Requirements for the Degree of

Doctor of Philosophy

at the

MASSACHUSETTS INSTITUTE OF TECHNOLOGY

February 2012

Author_____
Department of Chemistry
December 20, 2011

Certified by_____
Moungi G. Bawendi
Lester Wolfe Professor of Chemistry
Thesis Supervisor

Accepted by_____
Robert W. Field
Chairman, Department Committee of Graduate Students

This doctoral thesis has been examined by a committee of the Department of Chemistry as follows:

Professor Keith A. Nelson

Professor of Chemistry
Thesis Committee Chair

Professor Moungi G. Bawendi

Professor of Chemistry
Thesis Supervisor

Professor Troy Van Voorhis

Professor of Chemistry
Thesis Committee Member

Development of Fluorescent Semi-conductor Nanocrystal Conjugates for *in vitro* and *in vivo* Imaging Applications

by

Hee-Sun Han

Submitted to the Department of Chemistry on January 27, 2012 in partial fulfillment of the requirements for the degree of Doctor of Philosophy in Chemistry

ABSTRACT

Semiconductor nanocrystals, also known as quantum dots (QDs), are promising imaging probes with characteristic optical properties: tunable bandgap from visible to infrared, narrow and symmetric emission features, broad absorption, high quantum yield (QY), excellent photostability, and a large two-photon absorption cross section. However, unlike other imaging probes, the surface ligands determine the solubility, stability, quantum yield (QY), biocompatibility, and derivatizability of QDs. Therefore, to use QDs for *in vitro* and *in vivo* imaging, QD ligands need to be elaborately engineered for each experiment. Single cell labeling *in vivo* requires extremely strict criteria for the QD conjugates to be used such as minimal nonspecific cell/serum binding, maintenance of high QY in complex *in vivo* environments, and compact size.

The focus of this thesis is the synthesis of high quality QD conjugates that can be used for single molecule imaging *in vivo* and *in vivo* imaging studies that demonstrate the broad and powerful applicability of our new methods. We incorporated novel conjugation methods employing highly strained cycloolefins and a serum stable tetrazine derivative into newly developed polymeric imidazole ligands (PILs) to efficiently couple biomolecules on QDs. Unlike traditional conjugation methods, tetrazine-norbornene cycloaddition benefits from the non-interacting properties of the functional groups to the QD surface, and yields the high conjugation efficiencies on QDs. In addition, the rapid kinetics, absence of catalyst, and bio-orthogonality of the cycloaddition allowed us to achieve *in situ* conjugation of the norbornene-bearing QDs to tetrazine-bearing epidermal growth factor (EGF) proteins on the HeLa cell surface. On the *in vivo* front, we accomplished single endogenous cell imaging in live mice. The ability to target single cells using multiple biomarkers and track them for the extended periods of time allowed us to study the microenvironment of the endogenous hematopoietic stem cells (HSCs), which was not possible using conventional techniques engaging dye conjugated antibodies.

Lastly, a new class of QD ligands containing betaine moieties was developed to reduce the size of QD conjugates, which we expect will be greatly beneficial for *in vitro* and *in vivo* targeting in dense environments. We successfully demonstrated functionalization of the sulfonate betaine

poly imidazole ligands (SBPILs) with biomolecules, and the biocompatibility of SBPIL QDs both *in vitro* and *in vivo*.

Thesis Supervisor: Moungi G. Bawendi, Ph.D.
Title: Lester Wolfe Professor of Chemistry

Preface

Chapters from this dissertation were reproduced in part from the following references:

Han H-S, Devaraj NK, Lee J, Hilderbrand SA, Weissleder R, and Bawendi MG. Development of a Bioorthogonal and Highly Efficient Conjugation Method for Quantum Dots using Tetrazine-Norbornene Cycloaddition. *J Am Chem Soc* 2010, **132**: 7838–7839. Copyright 2010 American Chemical Society

Han H-S, Bhaumik J, Kamoun WS, Niemeyer E, Chen Y, Cui J, Martin JD, Fukumura D, Duda DG, Jain RK, and Bawendi MG. Development of quantum dot antibody conjugates for *in vivo* imaging of single endogenous cells. *Submitted*

Kamoun WS*, Niemeyer E*, **Han H-S***, Gillissen M, Roberge S, Lanning R, Martin JD, Bawendi MG, Munn LL, Fukumura D, Duda DG, and Jain RK. Multiplexed cytometric immunoimaging reveals normoxia in hematopoietic stem cell niche, submitted

Han H-S, Martin JD, Jungmin Lee, Daniel K. Harris, Jain RK, and Bawendi MG. Synthesis of compact and biocompatible quantum dots with a zwitterionic polymer coating, submitted

* Equal contribution

To My Family and Friends

Table of Contents

List of Figures

Chapter 1. Introduction to Semiconductor Nanocrystals and Their Applications in Biology

1.1 Colloidal Quantum Dots: Background, Theory, and Properties

Quantum dots (QDs), semiconductor nanocrystals, have gained much attention as a new class of fluorescence probes for cellular and biomolecular imaging with their unique optical properties such as tunable bandgap from visible to infrared, narrow and symmetric emission features, broad absorption features, high quantum yield (QY), high photostability, and large two-photon absorption cross section. In this chapter, we provide a basic theoretical background of QDs and their optical properties, and compare QDs with organic dyes to demonstrate the advantage of using QDs for bio-imaging.

1.1.1 Theory and the Physical Properties of Quantum Dots

1.1.1.1 Quantum confinement effect

Quantum dots are nanoscale crystalline assemblies of semiconducting materials consisting of a few hundred to several thousand atoms. Their size ranges from 1.5 nm to 10 nm. The small size of QDs confines spatial distribution of electrons and holes to the physical dimension of the QDs. Because the size of QDs is usually comparable to or smaller than the Bohr exciton radius of the particular semiconductor materials (ex. 5.6 nm for CdSe), quantum confinement effects become critical in QDs. Confinement effects can be explained by simple

extension of a quantum mechanical particle in a one-dimensional box to a three-dimensional sphere. As in a particle-in-a-box model, we expect the energy band diagram of QDs to be discrete and the energy band gap to be influenced by the size of QDs, with the relation of $1/r^2$.

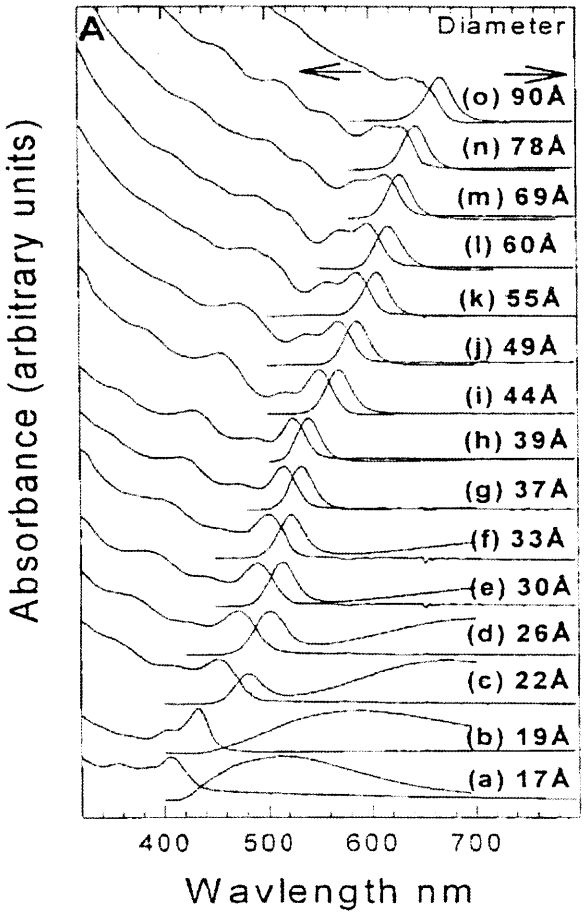

Figure 1-1 Absorbance and emission spectra of a CdSe size series. Broad emission features of the small QDs are originated from deep trap emission instead of bandedge emission. Figure reproduced from C.B. Murray, Ph.D. Thesis, MIT, 1995.

Figure 1-1 confirms the theoretical prediction. As the size of CdSe QDs decreases, the first absorption peaks and the bandedge emission peaks become blue-shifted. More detailed theoretical explanations about quantum confinement effects in QDs are described in references

[1, 2]. Tunability of bandgap as a function of size is one of the properties that make QDs attractive for a wide range of applications.

1.1.1.2 Blinking (Fluorescence intermittency)

In 1996, Nirmal et al. reported fluorescence intermittency of a single CdSe QD under continuous laser excitation [3]. As shown in Figure 1-2, the time-dependent fluorescence signal from single nanocrystals exhibits a sequence of "on" and "off" periods; "on" and "off" times can be as short as microseconds and as long as several minutes. It has been shown that the blinking behavior of QDs is universal for various types of QDs [4-7] at various temperatures [8-10]. The origin of QD blinking has not been fully explained, but it has been speculated that blinking is related to charging of QDs. This hypothesis is strongly supported by previous experiments showing that charged QDs are "dark", blinking and spectral shift are correlated [10], and local electric field fluctuations trigger spectral shifts of single QDs [11]. A popular theoretical model on blinking involves Auger recombination as a main cause of the blinking phenomenon. According to this model, a "dark" state is triggered by extra charge formation in QDs via Auger autoionization or thermal or tunnel autoionization of a nanocrystal and the ejected charge is localized in a trap in the surrounding matrix [12].

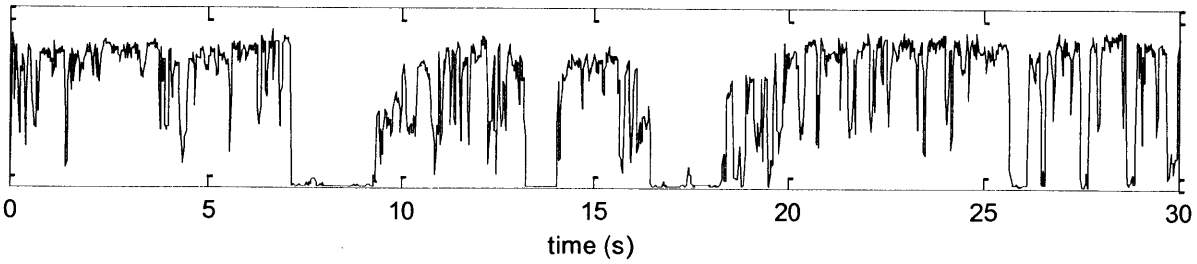

Figure 1-2 Time-dependent fluorescence signal from single CdSe/CdS QD. Y axis is I(t). Image reproduced from G. Nair PhD Thesis, MIT 2009.

Fluorescence intermittency is a serious drawback to the QD applications in single molecule tracking and quantum informatics. Various efforts have been made to suppress blinking. The first approach is adding "anti-blinking reagents." Since the blinking behavior is believed to be related to charging of QDs, small molecules that can act as charge compensators or charge mediators were added to stop blinking. Oligo(phenylene vinylene) [13] or thiol containing short chains such as mercaptoethylamine [14], β-mercaptoethanol [15], dithiothreitol [15], and thiopropionic acid [16] are reported to be effective in blinking reduction. For instance, 80% of QDs show two or less blinking events for 80 seconds when 1mM of β-mercaptoethanol was delivered. [15] The second approach is adding a thick inorganic shell layer around the QD core to physically isolate the wavefunction of the QD core from the QD surface and environments. Mahler et al. deposited 5.5 nm of crystalline CdS shell on CdSe cores that were 2.5 nm in diameter to yield 13 nm diameter core-shell nanocrystals [17]. When the time-dependent fluorescence traces of the single CdSe-CdS QD were recorded, only 5% of the QDs spent more than 1% of their time in the "off" state. Similarly, Chen et al. also observed greatly suppressed blinking behaviors in "giant" multishell CdSe nanocrystals (g-NQDs) [18]. They showed that adding thicker shells can effectively decouple the wavefunction of the QD core from the surface environments by showing constant quantum yield of the QDs after repeated precipitation/redissolution (or crash-out) processes or phase transfer to water via ligand exchange with mercaptosuccinic acid. In addition, they also showed that g-NQDs did not exhibit photo-brightening or photo-darkening under intensive UV illumination for several hours. Wang et al. took somewhat different route to illuminate blinking in QDs [19]. Instead of adding a thick crystalline shell on the QD cores, they synthesized a graded alloy of CdZnSe/ZnSe core/shell

QDs. Strikingly, these QDs exhibit no blinking over tens of minutes. They explained this blinking-free phenomenon as a result of radiative recombination of a trion.

Synthesizing non-blinking, water-soluble, stable, derivatizable, and bio-compatible QDs will enlarge the scope of QD applications as a single light source or as a probe for single molecule imaging.

1.1.2 Comparison of Quantum Dots with Organic Dyes

QDs are thought to be excellent probes for fluorescent imaging. In this section, physicochemical properties of organic dyes and QDs will be compared [20]. A summary of the comparison between QDs and organic dyes is presented in Table 1-1.

Table 1-1 Comparison of properties of organic dyes and QDs.

Property	**Organic dye**	**QD**
Size	Small molecule, less than 1 nm	6-60 nm (hydrodynamic diameter)
Molar extinction coefficient	0.25-2.5×10^5 M^{-1} cm^{-1} at the maximum absorbance	0.5-5×10^6 M^{-1} cm^{-1} at 350 nm[21] (CdSe: 0.4 ×10^5 M^{-1} cm^{-1} unit $cell^{-1}$ CdTe: 0.3 ×10^5 M^{-1} cm^{-1} unit $cell^{-1}$ CdS: 0.5 ×10^5 M^{-1} cm^{-1} unit $cell^{-1}$)*
Absorption spectra	Discrete bands, Shape is generally similar with the emission feature	Continuous absorption below the band edge to UV. Increase toward shorter wavelengths
Emission spectra	Asymmetric, often has a long tail toward long wavelengths, FWHM 35-100nm	Symmetric, Gaussian profile, FWHM Visible (25-45 nm), NIR (60-100 nm)

* Because QDs are composed of hundreds and thousands of unit cells, we showed the normalized molar extinction coefficients and two-photon action cross sections per unit cell of a variety of QDs for better comparison with those of organic dye molecules. Note that the normalized molar extinction coefficients of QDs are in the lower range of the organic dye values, while the normalized two-photon action cross sections of QDs are in the upper range of the organic dye values.

Quantum yield	Visible (0.5-1.0), NIR (0.01-0.10)	Visible (0.3-1.0), NIR (0.1-0.6)
Two-photon action cross-section	$1\times10^{-52} \sim 5\times10^{-48}$ cm^4 s $photon^{-1}$ (typically $\sim 1\times10^{-49}$ cm^4s $photon^{-1}$)	$2\times10^{-47} \sim 5\times10^{-46}$ cm^4s $photon^{-1}$ (CdSe: $1.2 \sim 2.0 \times10^{-49}$ cm^4s unit $cell^{-1}$ CdTe: $\sim1.0 \times10^{-49}$ cm^4s unit $cell^{-1}$)*
Photochemical stability	Usually photo-bleaches within several seconds under intense laser illumination for single molecule spectroscopy, extremely bad for NIR dyes	Does not photo-bleach under laser illumination, photo-brightening or -darkening can occur under extremely high power excitation
Thermal stability	Depends on dye class, bad for NIR dyes	High, depends on the shell and the ligands
Fluorescence Lifetimes	1~ 5 ns	10 ns ~ >1μs, even longer for type II QDs
Functionalization	Easy, usually monovalent (by proper molecule design)	Has to work through ligand chemistry, usually multivalent

1.1.2.1 Size

Figure 1-3 shows the relative size of fluorophores compared to bio-compartments.

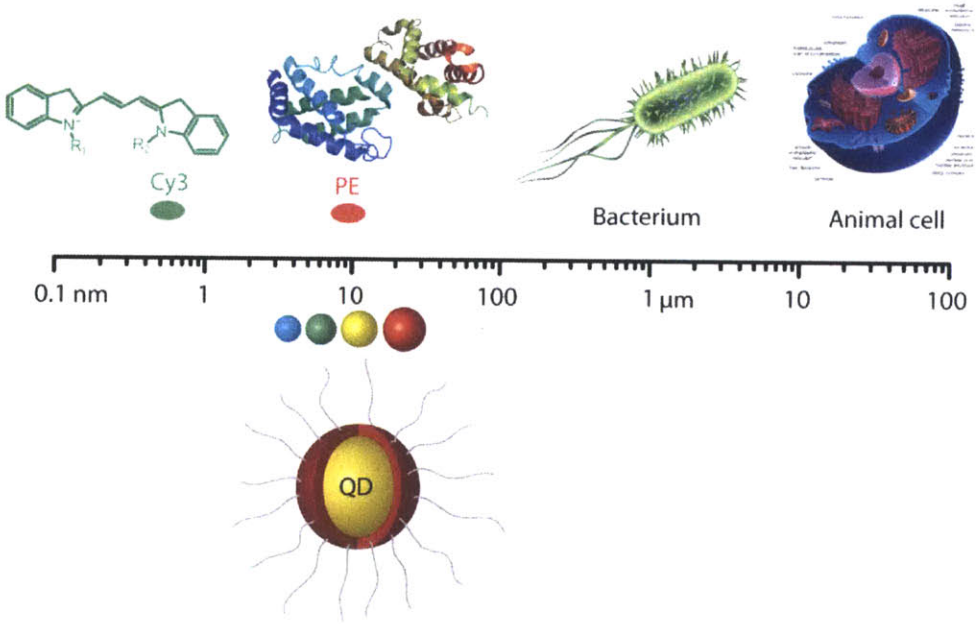

Figure 1-3 Relative size of fluorophores. Cy3 represents organic dye molecules (less than 1 nm) and PE (phycoerythrin) represents fluorescent proteins (~ 10 nm). Hydrodynamic diameter of QDs ranges from 6 nm to 50 nm depending on the size of the cores or the coatings.

Organic dyes are small molecules which usually have length less than 1 nm, while hydrodynamic diameters of QDs range from 6 nm to 60 nm. Due to the large size of QDs, QD attachments can change the dynamics of target molecules or trigger undesired biological pathways. Therefore, when QDs are attached to relatively small bio-molecules, control experiments always have to be performed by attaching smaller fluorescent probes instead of QDs to the target molecules. Previous literature has shown that *in vitro* labeling of individual glycine receptors (GlyRs) using QDs did not alter the diffusion dynamics of GlyRs in neurons [22]. However, our recent *in vivo* studies indicate that labeling the endothelial cell surface using QD antibody conjugates (QD-Ab) can change the endocytotic behavior of the cells (refer to Chapter 4).

1.1.2.2 Absorption features

The difference of QDs and dyes in their absorption features comes from different molecular structures. QDs are nanoscale crystalline assemblies, which have both bulk-like and atomic-like properties, while organic dyes are well-defined small molecules that have well-defined molecular orbitals. As illustrated in Figure 1-4, energy diagram of QDs consists of discretized energy levels near the bandedge and almost continuous bands far from the bandedge. In contrast, organic dyes have well defined discretized energy levels consisting of electronic energy states, vibrational energy states, and rotational energy states. Rotational energy states are not illustrated in Figure 1-4. The bulk semiconductor-like band structure of QDs contributes to the broad absorption features. In contrast, the discrete energy states of organic dyes result in narrow and more discretized absorption features (Figure 1-5). The broad absorption features of QDs are beneficial for their applications in multiplexing, because QDs of different colors can be

excited simultaneously with a single light source. In the case of organic dyes, each dye often needs its own excitation source since they have narrow absorbance features.

In addition, because QDs are composed of hundreds and thousands of repeated unit cells, each of which acts as a dipole oscillator, QDs intrinsically have higher absorption cross sections than organic molecules. Since brightness is defined by QY × absorption cross section at the excitation wavelength, QDs can be brighter than dyes under the same excitation conditions.

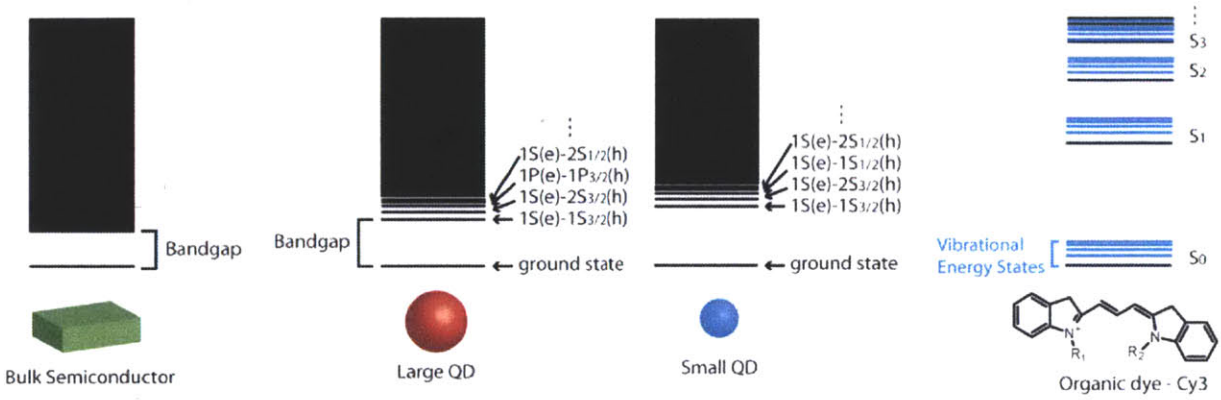

Figure 1-4 Representative band diagram of bulk semiconductor, small QD, large QD, and organic dye. Note that QDs have larger bandgap than bulk semiconductor and smaller QD has bigger bandgap. Organic molecules have additional vibrational states.

1.1.2.3 Emission features

As well-defined molecules, dyes have discrete electronic states, vibrational energy states, and rotational energy states (Figure 1-4). When a dye molecule is excited, the excited electron decays to the ground vibrational level of the excited state via intraband relaxation. Then, the excited electron radiatively decays to various vibrational states in the ground electronic state as shown in Figure 1-5. This phenomenon leads to an emission spectrum containing multiple peaks or shoulders. In contrast, QDs do not have defined vibrational energy states because of their

bulk-like nature, and excited electrons can only decay to one ground state. Therefore, the emission profile of QDs is usually narrow and Gaussian shape. (Figure 1-6)†

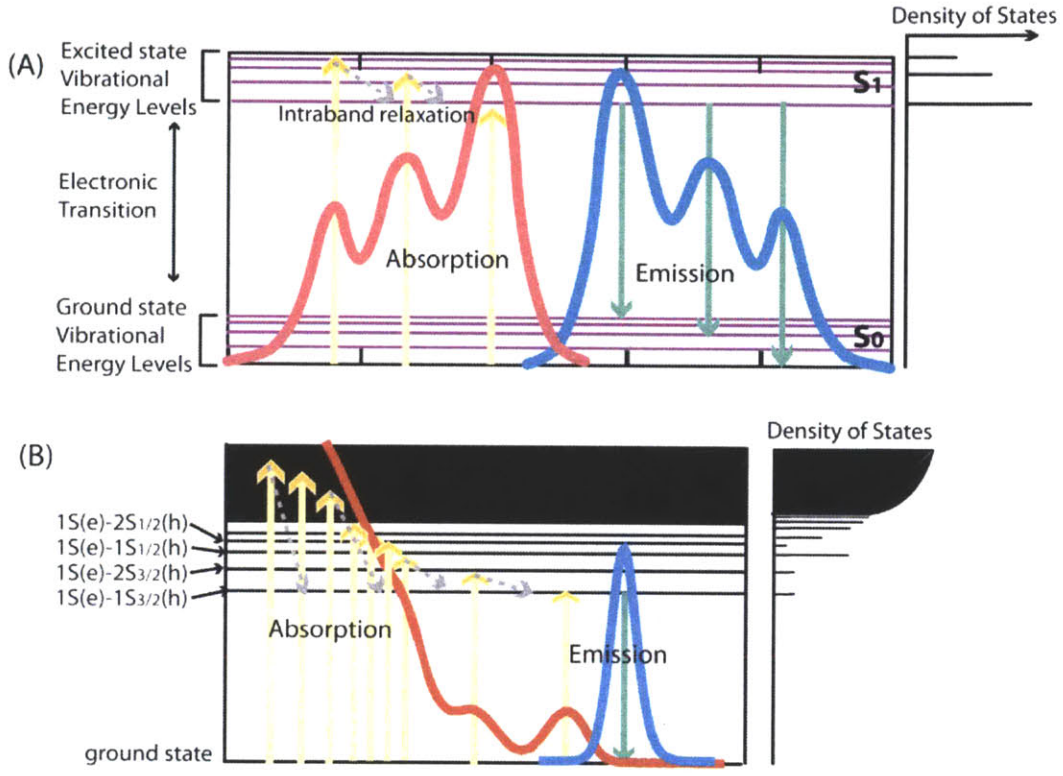

Figure 1-5 Representative electron transition diagram of (A) organic dyes and (B) QDs after UV excitation. Red curves represent spectra absorption and blue curves represent emission spectra.

Because of their narrow and symmetric emission profile, more colors of QDs can be used for multiplexed labeling without causing significant signal overlap. The ability to label multiple cells or bio-molecules simultaneously is crucial for parallel analysis of different analytes or for cell labeling in complex environments because multiple biomarkers are required to identify

† Emission profile of QDs starts to show multi-peak features when they are excited with high power laser to intentionally generate multi-excitons. However, a typical photon flux used for *in vitro* and *in vivo* imaging is much lower and does not generate large population of multi-excitons.

targeting cells [23-26]. In Chapter 4, we will demonstrate single hematopoietic stem cell labeling using multiple biomarkers.

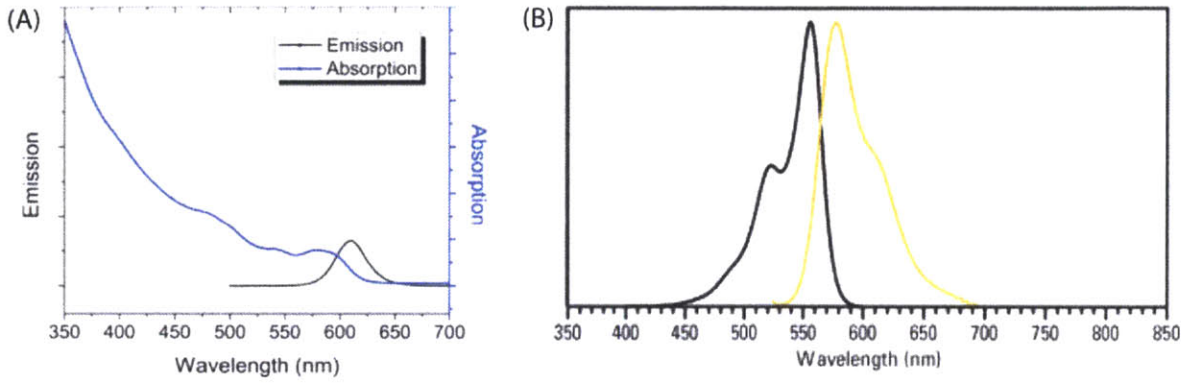

Figure 1-6 Representative absorption and emission spectra of (A) QDs (CdSe/CdZnS) and (B) organic dye (Dylight 550).

1.1.2.4 Stability

Fluorescence stability in buffers, blood serum and cell media under typical excitation fluxes is one of the most important properties of fluorophores. However, organic dyes tend to decompose under intense or long-term illumination and lose their photoluminescence. Recently, much effort has been made to develop new classes of organic dyes with higher photostability[27, 28], but our unpublished work shows even newly developed dyes (ex. Alexa) photobleach within several seconds under laser illumination with a typical photon flux that is used for cell imaging. In contrast, core-shell QDs show exceptionally stable emission intensity profile under intense illumination [29-31]. Our previous work shows that single QD labeling wild-type low density lipoprotein receptors can be imaged for at least an hour [32]. This result is consistent with what has been reported previously. Proper engineering of ligands might be crucial for QDs to retain high QY for extended period of time *in vitro* and *in vivo* [33].

1.1.2.5 Lifetime

QDs have comparatively longer radiative life than organic dyes; QDs have a lifetime of five to hundreds of ns while visible dyes have lifetime of about 5 ns and NIR dyes have one of about 1 ns. Within QDs made of the same materials, larger QDs have a longer fluorescence lifetime (several hundred ns for CdSe emitting in red and tens of ns for CdSe emitting in green) and type I QDs generally exhibit shorter lifetime than type II QDs. The significant difference in lifetime allows us to separate QD fluorescence from background fluorescence through time-domain imaging.[34]

1.2 Quantum Dot Applications in Biology

QDs have multiple advantages as imaging probes compared to organic dyes, such as high photostability, broad absorption features, and narrow emission features. High-photostability allows bio-molecule tracking that requires extended periods of viewing, and characteristic absorption and emission features enable simultaneous imaging of different targets. In this chapter, we are going to discuss various types of QD applications in biology.

1.2.1 Quantum Dots for Flow Cytometry Applications [35, 36]

With narrow and symmetric emission features and a large Stokes shift (up to 400 nm), QDs are useful for multicolor flow cytometry. Signal leak-through to neighboring color channels

is significantly less in case of QDs compared to organic dyes having the emission profiles with the same full-width-half-maximum, since dyes commonly have red tails in their emission. In addition, the large absorption cross section of QDs contributes to the high signal-to-noise value in flow cytometry experiments. Figure 1-7 shows that cells labeled with Qdot655-CD4 display signal-to-noise value that is 2 orders of magnitude bigger than cells labeled with AmCyan(orgnanic dye)-CD4.

The effect of attachments of QDs (10 ~ 20 nm) to antibodies (~12 nm) on the avidity of the antibodies should be checked since large QDs can alter the dynamics of antibody labeling. However, Figure 1-7 shows the concentrations of Qdot655-CD4 and AmCyan-CD4 required to achieve half-saturation are very similar (1-2 nM). Based on this result, we can conclude that QDs and organic dyes can be interchangeably used as fluorophores for flow cytometry experiments.

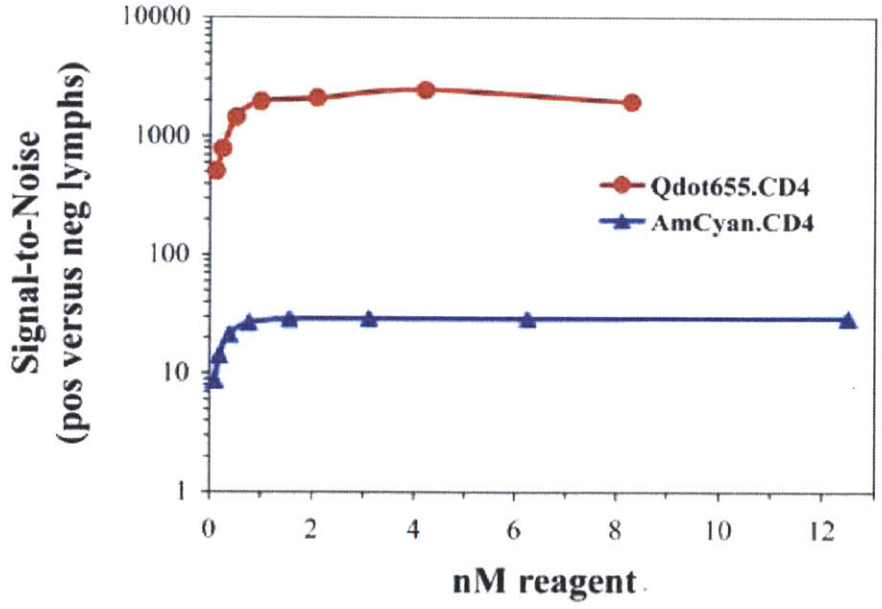

Figure 1-7 Comparative titrations of Qdot655-CD4 and AmCyan-CD4. Red curve represents labeling experiments using Qdot655-CD4 and blue curve represents labeling experiments using AmCyan-CD4.

1.2.2 Quantum Dots for *in vitro* Imaging

In early 2004, QD antibody conjugates (QD-Ab) became commercially available and numerous publications on *in vitro* labeling of cells or bio-molecules using QDs and QD conjugates have been reported. Targeting bio-molecules in cells using QD conjugates can be achieved by two different methods

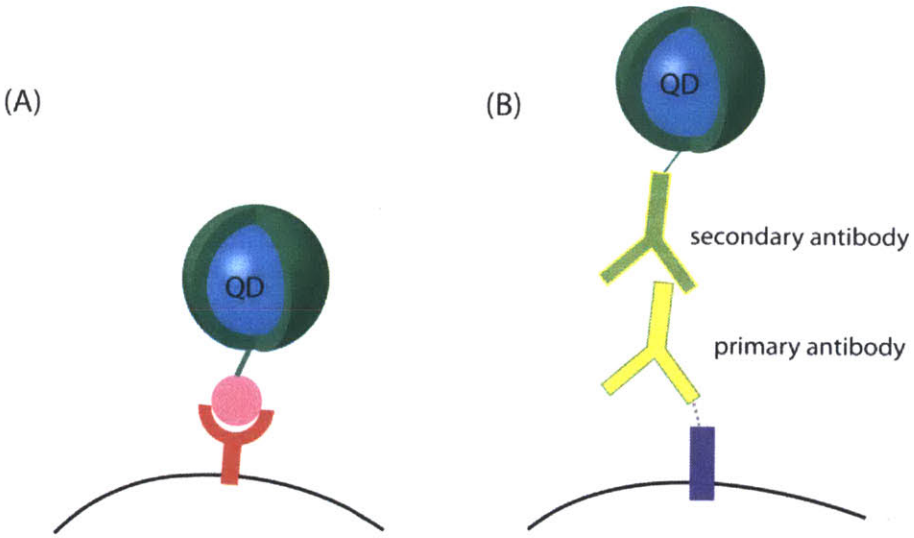

Figure 1-8 Two different routes to target biomarkers on the cell surface. (A) a receptor on the cell surface is labeled with a QD conjugated to the molecule that targets the receptor (B) an antigen on the cell surface is first labeled with a primary antibody which is targeted by a QD secondary antibody conjugate.

(Figure 1-8). In the first method (Figure 1-8A), target molecules are labeled with QDs that are directly coupled to molecules that interact with target molecules (aiming molecules). QD-streptavidin conjugates targeting biotinylated acceptor peptide (AP) Tag on cell surface is a typical example [32]. In the second method (Figure 1-8B), cells of interest or antigens are first

labeled using a primary antibody, followed by a QD secondary antibody conjugate. Secondary antibodies bind to all of the primary antibodies that were raised in the same type of animals (host); therefore, the same QD-secondary antibody conjugates can be used to label various types of antigens. Commercially available QD-antibody conjugates involve this method.

1.2.2.1 Imaging of fixed cells and tissues [37-47]

The easiest method to deliver QDs into cytosol to label intra cellular bio-molecules is through cell fixation followed by permeabilization treatments. The detergent used to remove cell membranes has to be chosen carefully so that the cellular structure of interest can be preserved and the sites of interest can be labeled efficiently. Detailed procedures to fix and permeabilize cells have to be optimized for each cell line and target.

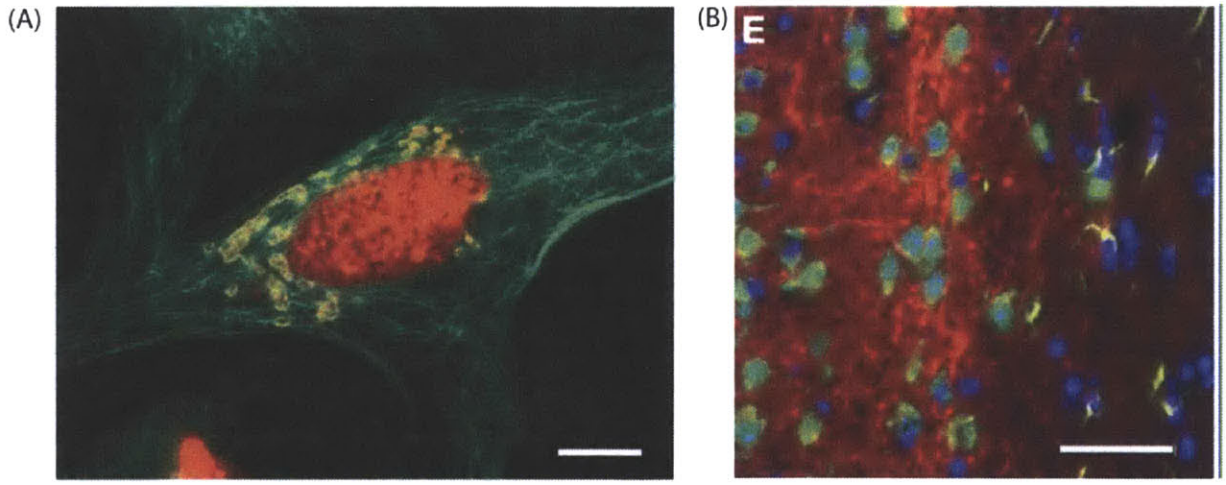

Figure 1-9 QD labeling on fixed cells. (A)HeLa cells are fixed with cold methanol/acetone and labeled with QD secondary antibody conjugates. Green signal represents microtubules labeled with a rat anti-tubulin antibody and a 525 nm QD anti-rat secondary antibody conjugate, yellow signal represent golgi apparatus labeled with a rabbit anti-giantin antibody and a 585 nm QD anti-rabbit secondary antibody conjugate, and red signal represents nucleus labeled with a mouse anti-nuclesome antibody and a 655 nm QD anti-mouse secondary antibody conjugates. Scale bar = 5 μm. Image reproduced from Methods Mol Bio,2007, 374: p 5. (B) Immunostained section of

adult mouse brain. Green signal represents NeuN, a marker of mature neurons, labeled with TSA and QD525 streptavidin conjugate, yellow signal represents glial fibrillary-associated protein labeled with a ribbit polyclonal antiserum and QD565 donkey anti-rabbit secondary antibody, red signal represents microtubule-associated protein-2 labeled with a mouse monoclonal antibody and QD605 goat anti-mouse seconday antibody, and blue signal represents nuclei labeled with Hoescht33258 dye. Scale bar = 40 μm. Image reproduced from Methods Mol Bio, 2007, 374: p 24.

Figure 1-9A shows HeLa cells fixed and labeled with primary antibodies and QD secondary antibody conjugates. Three different compartments in cells (microtubules, golgi apparatus, and nuclei) were labeled using the different color QD conjugates. To simultaneously label multiple types of biomarkers with QD conjugates of different colors, each set of biomarkers should be labeled with primary antibodies that were raised in different animal host species. Then, QDs conjugated to secondary antibodies that were raised against the host animals should be incubated with the cells to target the corresponding primary antibodies.

QD conjugates can also be used for immunohistochemistry, the process of detecting antigens in a tissue section. Immunohistochemical (IHC) staining is useful to understand spatial distribution of biomarkers or proteins in different parts of tissues. To achieve the IHC staining, harvested tissues were fixed, sectioned, treated with primary antibodies and lastly incubated with QD secondary antibody conjugates (Figure 1-8B). Figure 1-9B shows a typical IHC staining using QDs.

1.2.2.2 Imaging of live cells [22, 32, 48-52]

Most publications on live cell imaging using QD conjugates demonstrate labeling target molecules that are on the cell surface [22, 32, 48-52]. The exceptional photostability of QDs

allows researchers to study detailed dynamics of the target molecules for extended periods of time. Toxicity studies have shown that QDs do not affect the viability of cells when they are coated with well-engineered ligands [24, 53, 54]. Criteria of the QD ligands to use the QDs for *in vitro* applications are: neutral or slightly negative charge to prevent non-specific interaction with cells and proteins, and possession of strong binding groups to the QD surface to prevent detachment of the ligands.

Various efforts have been made to deliver QDs into the cytosol of live cells: electroporation, microinjection, and endocytosis combined with the use of endosomal burst reagents. The last method, utilizing endocytosis of QDs, is the most common approach because electroporation and microinjection are destructive to cells. However, more studies need to be done to promote QD release from endosomes while minimizing the cytotoxicity.

1.2.3 Quantum Dots for *in vivo* Imaging

Highly scattering and absorbing *in vivo* environments can benefit from the usage of near infrared (NIR) QDs as probes. As shown in Figure 1-10, biological media exhibit low scattering and absorption in 750~900 nm region. As a result, deeper tissues can be imaged using NIR fluorophores than visible fluorephores [55]. Unfortunately, NIR organic dyes have extremely bad thermal- and photostability [20], and therefore, developing biocompatible NIR QDs is of great interest. Some of the works presented in the following sections utilize NIR QDs and demonstrate deep organ or tumor detection.

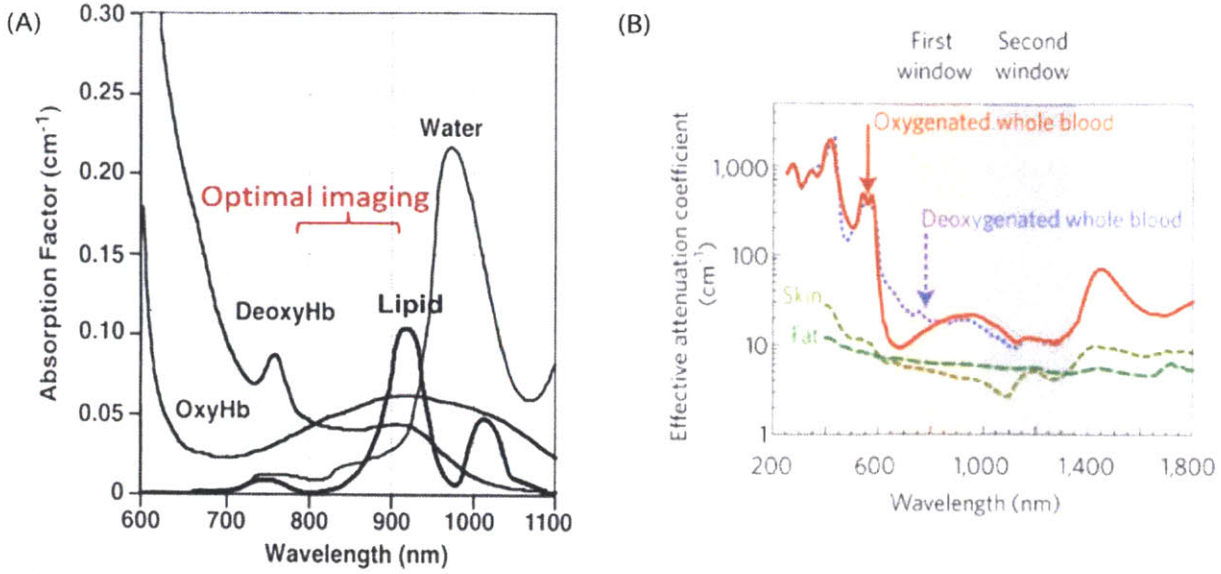

Figure 1-10 Absorbance spectra of the bio-molecules or bio-compartments in the NIR region. (A) Absorption spectra for exygenated and deoxygenated hemoglobin, lipid and water. With the absence of intense absorbing features, 750 ~ 850 nm is optimal for *in vivo* imaging. Figure reproduced from W. Liu, Ph.D. Thesis, MIT, 2010. (B) Two NIR windows with low absorption by biological media. Water Raman band exist around 1,000 nm. Image reproduced with permission from Nat Nano, 2009. 4(11): p. 710-711. Copyright 2009 Nature Publishing Group [56].

In vivo environments are much more complex than *in vitro* environments and contain a variety of bio-molecules that can interact with QDs and quench their fluorescence or trigger undesirable biological pathways. Therefore, elaborate engineering of ligands is critical to use QDs for *in vivo* imaging. The following are the basic requirements for the ligands: 1) strong binding to the QD surface to prevent detachment of the ligands which causes fluorescence quenching, 2) controllable derivatizability to efficiently couple molecules that target the molecules of interest (antibodies, peptides, DNA strands, etc.), and 3) minimal non-specific binding nature (stealthy nature) of the ligand coated QDs to cells and serum proteins. In addition, more requirements are added depending on specific *in vivo* applications. Due to the strict

restrictions on the properties of ligands, new *in vivo* applications of QDs usually accompany new ligand developments. In the following sections, we summarize previous reports on QD applications in *in vivo* imaging and ligand developments.

1.2.3.1 Sentinel lymph node mapping [57-60]

Sentinel lymph node (SLN) is the first lymph node to which metastasizing cancer cells from a primary tumor are drained. It is believed that some types of cancer cells spread through the lymphatic system--first to regional lymph nodes, then to other lymph nodes and so on. Therefore, identifying and resecting the sentinel lymph node, known as sentinel lymph node biopsy, is a common treatment to prevent further spread of the cancer cells.

In 2003, Kim et al. reported the use of NIR CdTe(CdSe) core(shell) type II QDs for sentinel lymph node mapping. [60] QDs coated with oligomeric phosphine organic coatings were injected intradermally and the QDs migrated to SLN within minutes. By using the NIR QDs, they were able to identify SLNs that were approximately 1 cm below the skin surface with low power NIR excitation (5 mW/cm^2). They also showed that the fluorescence level of QDs stayed constant over long period of time (at least up to 20 minutes) under laser illumination unlike the dye-based SLN trackers.

The ligands used for this experiment, oligomeric phosphine organic coatings, were synthesized by cross-linking monomeric alkyl phosphines and introducing functionality. The multi-dentate binding moiety provides strong binding of the ligands to the QD surface, and the carboxyliate moiety provides water-solubility and derivatizability. For the SLN mapping experiments, QDs were injected without further functionalization.

1.2.3.2 Tumor targeting [61]

Taking a step further from the previous SLN experiments, QDs can be conjugated to antibodies and used for targeting specific cells or receptors *in vivo*. For the specific targeting experiments, the blood circulation half-life of QDs should be extended to promote active targeting. Extending the circulation half-life of QDs can be achieved by coating the QD surface with poly(ethylene glycol) (PEG) and making them non interactive with the environments.

In 2004, Gao et al. synthesized a new class of amphiphilic polymers to prepare water-soluble QDs that can be used for tumor targeting *in vivo*. The encapsulating polymers contain hydrophobic alkyl chains that intercalate with the native hydrophobic QD ligands, PEG chains that provide water-solubility and biocompatibility, and carboxylic acid groups for further functionalization. Using the newly developed encapsulated QD-antibody conjugates (eQD-Ab), they targeted C4-2 human prostate tumors implanted in live mice after the systemic injection of the QDs via the tail vein. Targeting solid tumors using QD conjugates involves ensemble measurements of QD signals. Therefore, criteria for the QDs for such applications are not as strict as the criteria for the QDs for single cell imaging *in vivo*. Single cell imaging *in vivo* has not been achieved yet.

1.3 Quantum Dots for Other Biochemical Applications

With large absorption cross sections, high QY, narrow emission features and high photostability, QDs are also useful for fluorescence based assays such as reverse-phase protein micro arrays, multicolor sandwich immunoassays, multicolor genotyping assays, and

competition immunoassays. In these examples, target molecules are detected by the fluorescent signals coming from the QDs bound to the analytes. Representative examples can be found in references [62-67].

Taking a step further from the previous examples, QDs themselves can be engineered so that their emission profiles change in the presence of analytes. To synthesize such QD sensors, QDs are conjugated to dyes that change the absorbance profile when bound to analytes (ex. pH, pO_2, etc.). Because Förster resonance energy transfer (FRET) rate is highly dependent on the spectral overlap between donor emission and acceptor absorbance, the change of the absorbance spectra of the acceptor dyes will strongly influence the FRET efficiencies. Figure 1-11 is the representative emission profile of a QD pH sensor. As we can see, the ratio between QD emission and dye emission changes depending on the pH of the buffers. More detailed information about the QD sensors can be found in reference [68].

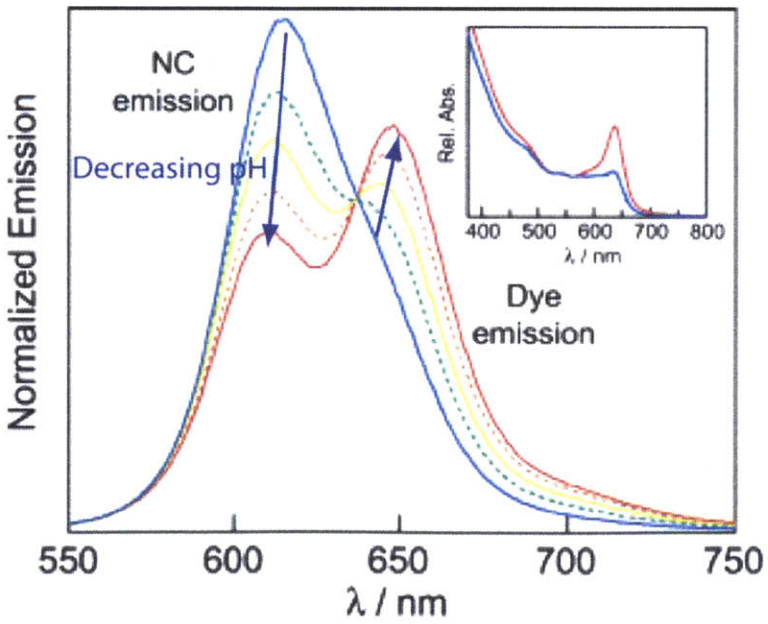

Figure 1-11 Emission profile of a QD pH sensor (QD squaraine dye conjugates) in different pH buffers. As pH of buffers decrease, QD emissions (NC emission) are quenched and dye emissions are enhanced.

1.4 Thesis Overview

1.4.1 Background and Motives

The theme of this thesis is the development of bio-compatible ligands and conjugation methods to synthesize QD conjugates that can be used for single cell imaging *in vivo*. Imaging endogenous single cells in live animals can provide much information about cellular interactions and their native environments *in vivo*. However, developing the QD conjugates for such applications has been a big challenge because of the high standards required for the imaging probes. Single cell imaging requires the tracking of single or few probes for extended periods of time, while meso-sized object detection (solid tumor, sentinel lymph node, etc.) involves ensemble measurements of the fluorescent signals over a large area at a certain time point. Following are the detailed requirements for the QD conjugates to achieve single cell imaging *in vivo*. First, QDs have to maintain high QY for extended periods of time in *in vivo* environments which contain high concentrations of proteins, small molecules, and salts. Since ligand detachment is thought to be the primary cause of the QY drop in such complex environments, we need to develop ligands containing binding groups that have high binding affinity to the QD surface and are chemically stable. Second, QD conjugates have to show minimal nonspecific binding to cells and proteins to achieve specific targeting *in vivo*. Low nonspecific binding nature (or the stealthy nature) of the probes becomes critical for single cell imaging, since even small numbers of nonspecifically absorbed QDs can provide false signals or raise the background signals. Third, efficient conjugation methods need to be developed to efficiently couple QDs to the molecules that target the molecule of interest (aiming molecules). Traditional

conjugation methods involve carboxylic acids, amines or thiols that are known to interact with the QD surface. Therefore, only a small number of derivatizable groups is available for further conjugation and conjugation efficiencies and reproducibility become low. Lastly, a smaller hydrodynamic diameter for QD conjugates is better for efficient targeting. Reference [69, 70] shows that small particles are known to diffuse faster in dense *in vivo* environments than larger particles. Therefore, developing small particles can enhance targeting efficiencies in dense environments such as solid tumor or bone marrow.

Recently developed PEG containing poly imidazole ligands (PEGPILs) are great candidates for QD ligands. PEGPILs possess multidentate binding groups that are chemically stable and strongly binding to the QD surface, and long poly (ethylene glycol) (PEG) chains that provide exceptionally low protein/cell binding properties. However, the development of new conjugation methods on PEGPIL QDs is required since traditional conjugations utilizing primary amine groups are known to yield irreproducible and low conjugation efficiencies. Conjugation efficiencies can be improved by incorporating more amines to the PILs, but increased number of primary amines causes significant increase of nonspecific binding of the QD conjugates to cells and proteins through positive charges on the QD surface. Therefore, in this thesis we incorporated a new type of conjugation methods involving neutral molecules into the PEGPIL ligand system. By combining all the recent advances in QD synthesis, ligand development and conjugation method developments, we were able to demonstrate single endogenous cell labeling using multiple QD antibody conjugates in live mice.

1.4.2 Thesis Summary

In Chapter 2, we employ tetrazine-norbornene cycloaddition as a new conjugation scheme on QDs. This catalyst-free click chemistry benefits from rapid kinetics, irreversibility, bio-orthogonality, and non-interacting nature of the functional groups with the QD surface. In addition, the reaction involves neutral molecules so that incorporation of more norbornene groups on QDs do not affect the level of nonspecific protein/cell binding of the QDs. Taking these advantages, we were able to show 1) highly efficient coupling of organic dyes, and proteins on QDs using the tetrazine-norbornene cycloaddition as a conjugation method, and 2) achievement of in situ clicking of QD-EGF to target EGFR on the HeLa cell surface.

In Chapter 3, we took a step forward and optimized the conjugation chemistry to synthesize compact QD antibody conjugates (QD-Ab) that can be used for *in vivo* labeling. Comparison with the commercial Qdot® 625 showed that our QDs are more compact and possess far less nonspecific protein binding nature. Through *in vivo* vessel labeling, we were able to optimize the ratio between QDs and antibodies in the QD conjugates to yield the best imaging results and check the effect of the attachment of nano-sized QDs to antibodies. Finally, single endogenous hematopoietic stem cells (HSCs) in bone marrow were successfully labeled and imaged with high signal to noise ratio in live mice after systemic injection of the QD-Ab.

In Chapter 4, using the newly synthesized QD-Ab, we studied the microenvironment of endogenous HSCs. This could not have been done with traditional dye-conjugated antibodies due to the broad and assymetric emission features, and the low two photon cross section of organic dyes. A series of experiments proved that HSCs preferentially reside in single vessel cavities, and have normoxic niches. HSC niches being normoxic contradicts the generally accepted hypothesis that HSC niches are hypoxic. These results highlight the importance of the *in vivo*

QD-Ab labeling technique we presented in this thesis in studying cellular environment and dynamics in live animals which was hard to achieve with the traditional techniques.

In Chapter 5, we explored a new type of ligands than traditionally used PEG based ligands. Recent studies have shown that zwitterionic ligands exhibit extremely low bio-fouling properties owing to the strong hydration capacity via electrostatic interactions. If we synthesize bio-compatible zwitterioinc ligands, the hydrodynamic diameter of the zwitterionic QDs can be significantly reduced from PEG containing QDs due to the absence of long PEG chains. Therefore, in this chapter, betaine PILs were synthesized and the biological behaviors of betaine PIL QDs were studied both *in vitro* and *in vivo.* The studies showed that betaine PIL QDs have low nonspecific cell/protein binding nature and can be useful for *in vitro* targeting and *in vivo* vessel tracing. However, long PEG chains seem to perform better at passivating QDs than the betaine moieties since PEG PIL QDs exhibited more stealthy nature than betaine PIL QDs both *in vitro* and *in vivo.*

In summary, this thesis explores new conjugation methods on QDs, synthesis of QD-conjugates used for *in vivo* single cell imaging, the usage of the QD conjugates for *in vitro* and *in vivo* imaging, and a new type of QD ligands.

1.5 References

1. Ekimov AI, Onushchenko AA: **Quantum dize effect in the optical spectra of semiconductor microcrystals**. *Sov Phys Semicond* 1982, **16**:775.

2. Efros AL, Efros AL: **Interband adsorption of light in a semiconductor sphere**. *Sov Phys Semicond* 1982, **16**:772-775.

3. Nirmal M, Dabbousi BO, Bawendi MG, Macklin JJ, Trautman JK, Harris TD, Brus LE: **Fluorescence intermittency in single cadmium selenide nanocrystals**. *Nature* 1996, **383**(6603):802-804.

4. Tittel J, Göhde W, Koberling F, Basché T, Kornowski A, Weller H, Eychmüller A: **Fluorescence Spectroscopy on Single CdS Nanocrystals**. *The Journal of Physical Chemistry B* 1997, **101**(16):3013-3016.

5. Koberling F, Mews A, Basché T: **Single-dot spectroscopy of CdS nanocrystals and CdS/HgS heterostructures**. *Physical Review B* 1999, **60**(3):1921-1927.

6. Shimizu KT, Neuhauser RG, Leatherdale CA, Empedocles SA, Woo WK, Bawendi MG: **Blinking statistics in single semiconductor nanocrystal quantum dots**. *Physical Review B* 2001, **63**(20):205316.

7. Kuno M, Fromm DP, Hamann HF, Gallagher A, Nesbitt DJ: **"On"/"off" fluorescence intermittency of single semiconductor quantum dots** *J Chem Phys* 2001, **115**:1028-1040.

8. Banin U, Bruchez M, Alivisatos AP, Ha T, Weiss S, Chemla DS: **Evidence for a thermal contribution to emission intermittency in single CdSe/CdS core/shell nanocrystals** *J Chem Phys* 1999, **110**:1195-1201.

9. Kuno M, Fromm DP, Hamann HF, Gallagher A, Nesbitt DJ: **Nonexponential "blinking" kinetics of single CdSe quantum dots: A universal power law behavior** *J Chem Phys* 2000, **112**:3117-3120.

10. Neuhauser RG, Shimizu KT, Woo WK, Empedocles SA, Bawendi MG: **Correlation between Fluorescence Intermittency and Spectral Diffusion in Single Semiconductor Quantum Dots**. *Physical Review Letters* 2000, **85**(15):3301-3304.

11. Empedocles SA, Norris DJ, Bawendi MG: **Photoluminescence Spectroscopy of Single CdSe Nanocrystallite Quantum Dots**. *Physical Review Letters* 1996, **77**(18):3873-3876.

12. Efros A: **Semiconductor Nanocrystals: From Basic Principles to Applications**. New York: Kluwer Academic / Plenum Publishers; 2003.

13. Hammer NI, Early KT, Sill K, Odoi MY, Emrick T, Barnes MD: **Coverage-Mediated Suppression of Blinking in Solid State Quantum Dot Conjugated Organic Composite Nanostructures**. *The Journal of Physical Chemistry B* 2006, **110**(29):14167-14171.

14. Biebricher A, Sauer M, Tinnefeld P: **Radiative and Nonradiative Rate Fluctuations of Single Colloidal Semiconductor Nanocrystals**. *The Journal of Physical Chemistry B* 2006, **110**(11):5174-5178.

15. Hohng S, Ha T: **Near-Complete Suppression of Quantum Dot Blinking in Ambient Conditions**. *Journal of the American Chemical Society* 2004, **126**(5):1324-1325.

16. He H, Qian H, Dong C, Wang K, Ren J: **Single Nonblinking CdTe Quantum Dots Synthesized in Aqueous Thiopropionic Acid**. *Angewandte Chemie International Edition* 2006, **45**(45):7588-7591.

17. Mahler B, Spinicelli P, Buil S, Quelin X, Hermier J-P, Dubertret B: **Towards non-blinking colloidal quantum dots**. *Nat Mater* 2008, **7**(8):659-664.

18. Chen Y, Vela J, Htoon H, Casson JL, Werder DJ, Bussian DA, Klimov VI, Hollingsworth JA: **"Giant" Multishell CdSe Nanocrystal Quantum Dots with Suppressed Blinking**. *Journal of the American Chemical Society* 2008, **130**(15):5026-5027.

19. Wang X, Ren X, Kahen K, Hahn MA, Rajeswaran M, Maccagnano-Zacher S, Silcox J, Cragg GE, Efros AL, Krauss TD: **Non-blinking semiconductor nanocrystals**. *Nature* 2009, **459**(7247):686-689.

20. Resch-Genger U, Grabolle M, Cavaliere-Jaricot S, Nitschke R, Nann T: **Quantum dots versus organic dyes as fluorescent labels**. *Nature Methods* 2008, **5**(9):764-775.

21. Leatherdale CA, Woo WK, Mikulec FV, Bawendi MG: **On the Absorption Cross Section of CdSe Nanocrystal Quantum Dots**. *J Phys Chem B* 2002, **106**(31):7619-7622.

22. Dahan M, Levi S, Luccardini C, Rostaing P, Riveau B, Triller A: **Diffusion Dynamics of Glycine Receptors Revealed by Single-Quantum Dot Tracking**. *Science* 2003, **302**(5644):442-445.

23. Kobayashi H, Hama Y, Koyama Y, Barrett T, Regino CAS, Urano Y, Choyke PL: **Simultaneous Multicolor Imaging of Five Different Lymphatic Basins Using Quantum Dots**. *Nano Letters* 2007, **7**(6):1711-1716.

24. Jaiswal JK, Mattoussi H, Mauro JM, Simon SM: **Long-term multiple color imaging of live cells using quantum dot bioconjugates**. *Nat Biotech* 2003, **21**(1):47-51.

25. De Rosa SC, Brenchley JM, Roederer M: **Beyond six colors: A new era in flow cytometry**. *Nat Med* 2003, **9**(1):112-117.

26. Goldman ER, Clapp AR, Anderson GP, Uyeda HT, Mauro JM, Medintz IL, Mattoussi H: **Multiplexed Toxin Analysis Using Four Colors of Quantum Dot Fluororeagents**. *Analytical Chemistry* 2003, **76**(3):684-688.

27. Panchuk-Voloshina N, Haugland RP, Bishop-Stewart J, Bhalgat MK, Millard PJ, Mao F, Leung W-Y, Haugland RP: **Alexa Dyes, a Series of New Fluorescent Dyes that Yield Exceptionally Bright, Photostable Conjugates**. *Journal of Histochemistry & Cytochemistry* 1999, **47**(9):1179-1188.

28. Berlier JE, Rothe A, Buller G, Bradford J, Gray DR, Filanoski BJ, Telford WG, Yue S, Liu J, Cheung C-Y *et al*: **Quantitative Comparison of Long-wavelength Alexa Fluor Dyes to Cy Dyes: Fluorescence of the Dyes and Their Bioconjugates**. *Journal of Histochemistry & Cytochemistry* 2003, **51**(12):1699-1712.

29. Sun YH, Liu YS, Vernier PT, Liang CH, Chong SY, Marcu L, Gundersen MA: **Photostability and pH sensitivity of CdSe/ZnSe/ZnS quantum dots in living cells**. *Nanotechnology* 2006, **17**(17):4469.

30. Medintz I, Uyeda H, Goldman E, Mattoussi H: **Quantum dot bioconjugates for imaging, labelling and sensing**. *Nat Mater* 2005, **4**:435-446.

31. Wu X, Liu H, Liu J, Haley KN, Treadway JA, Larson JP, Ge N, Peale F, Bruchez MP: **Immunofluorescent labeling of cancer marker Her2 and other cellular targets with semiconductor quantum dots**. *Nat Biotechnol* 2003, **21**(1):41-46.

32. Howarth M, Liu W, Puthenveetil S, Zheng Y, Marshall LF, Schmidt MM, Wittrup KD, Bawendi MG, Ting AY: **Monovalent, reduced-size quantum dots for imaging receptors on living cells**. *Nat Methods* 2008, **5**(5):397-399.

33. Nida DL, Nitin N, Yu WW, Colvin VL, Richards-Kortum R: **Photostability of quantum dots with amphiphilic polymer-based passivation strategies**. *Nanotechnology* 2008, **19**(3):035701.

34. Clapp AR, Medintz IL, Fisher BR, Anderson GP, Mattoussi H: **Can Luminescent Quantum Dots Be Efficient Energy Acceptors with Organic Dye Donors?** *Journal of the American Chemical Society* 2005, **127**(4):1242-1250.

35. Chattopadhyay PK, Price DA, Harper TF, Betts MR, Yu J, Gostick E, Perfetto SP, Goepfert P, Koup RA, De Rosa SC *et al*: **Quantum dot semiconductor nanocrystals for immunophenotyping by polychromatic flow cytometry**. *Nat Med* 2006, **12**(8):972-977.

36. Abrams B, Dubrovsky T: **Quantum dots in flow cytometry**. *Methods Mol Biol* 2007, **374**:185-203.

37. Ornberg RL, Liu H: **Immunofluorescent labeling of proteins in cultured cells with quantum dot secondary antibody conjugates**. *Methods Mol Biol* 2007, **374**:3-10.

38. Shi C, Zhou G, Zhu Y, Su Y, Cheng T, Zhau HE, Chung LW: **Quantum dots-based multiplexed immunohistochemistry of protein expression in human prostate cancer cells**. *Eur J Histochem* 2008, **2**:127-134.

39. Ness JM, Akhtar RS, Latham CB, Roth KA: **Combined Tyramide Signal Amplification and Quantum Dots for Sensitive and Photostable Immunofluorescence Detection**. *Journal of Histochemistry & Cytochemistry* 2003, **51**(8):981-987.

40. Giepmans BNG, Deerinck TJ, Smarr BL, Jones YZ, Ellisman MH: **Correlated light and electron microscopic imaging of multiple endogenous proteins using Quantum dots**. *Nat Meth* 2005, **2**(10):743-749.

41. Xing Y, Chaudry Q, Shen C, Kong KY, Zhau HE, Chung LW, Petros JA, O'Regan RM, Yezhelyev MV, Simons JW *et al*: **Bioconjugated quantum dots for multiplexed and quantitative immunohistochemistry**. *Nat Protocols* 2007, **2**(5):1152-1165.

42. Wu X, Liu H, Liu J, Haley KN, Treadway JA, Larson JP, Ge N, Peale F, Bruchez MP: **Immunofluorescent labeling of cancer marker Her2 and other cellular targets with semiconductor quantum dots**. *Nat Biotech* 2003, **21**(1):41-46.

43. Matsuno A, Itoh J, Takekoshi S, Nagashima T, Osamura RY: **Three-dimensional Imaging of the Intracellular Localization of Growth Hormone and Prolactin and Their mRNA Using Nanocrystal (Quantum Dot) and Confocal Laser Scanning Microscopy Techniques**. *Journal of Histochemistry & Cytochemistry* 2005, **53**(7):833-838.

44. Ghazani AA, Lee JA, Klostranec J, Xiang Q, Dacosta RS, Wilson BC, Tsao MS, Chan WCW: **High Throughput Quantification of Protein Expression of Cancer Antigens in Tissue Microarray Using Quantum Dot Nanocrystals**. *Nano Letters* 2006, **6**(12):2881-2886.

45. Akhtar RS, Latham CB, Siniscalco D, Fuccio C, Roth KA: **Immunohistochemical detection with quantum dots**. *Methods Mol Biol* 2007, **374**:11-28.

46. Itoh J, Osamura RY: **Quantum Dots for Multicolor Tumor Pathology and Multispectral Imaging**. *Methods Mol Biol* 2007, **374**:29-42.

47. Knoll JH: **Human Metaphase Chromosome FISH Using Quantum Dot Conjugates**. *Methods Mol Biol* 2007, **374**:55-66.

48. Medintz IL, Pons T, Delehanty JB, Susumu K, Brunel FM, Dawson PE, Mattoussi H: **Intracellular Delivery of Quantum Dot–Protein Cargos Mediated by Cell Penetrating Peptides**. *Bioconjugate Chemistry* 2008, **19**(9):1785-1795.

49. Lidke DS, Nagy P, Jovin TM, Arndt-Jovin DJ: **Biotin-Ligand Complexes With Streptavidin Quantum Dots for In Vivo Cell Labeling of Membrane Receptors**. *Methods Mol Biol* 2007, **374**:69-79.

50. Wylie PG: **Multiple cell lines using quantum dots**. *Methods Mol Biol* 2007, **374**:113-123.

51. Gu W, Pellegrino T, Parak WJ, Boudreau R, Gros MA, Alivisatos AP, Larabell CA: **Measuring Cell Motility Using Quantum Dot Probes**. *Methods Mol Biol* 2007, **374**:125-131.

52. Jaiswal JK, Goldman ER, Mattoussi H, Simon SM: **Use of quantum dots for live cell imaging**. *Nat Meth* 2004, **1**(1):73-78.

53. Voura EB, Jaiswal JK, Mattoussi H, Simon SM: **Tracking metastatic tumor cell extravasation with quantum dot nanocrystals and fluorescence emission-scanning microscopy**. *Nat Med* 2004, **10**(9):993-998.

54. Hanaki K-i, Momo A, Oku T, Komoto A, Maenosono S, Yamaguchi Y, Yamamoto K: **Semiconductor quantum dot/albumin complex is a long-life and highly photostable endosome marker**. *Biochemical and Biophysical Research Communications* 2003, **302**(3):496-501.

55. Allen PM, Liu W, Chauhan VP, Lee J, Ting AY, Fukumura D, Jain RK, Bawendi MG: **InAs(ZnCdS) Quantum Dots Optimized for Biological Imaging in the Near-Infrared**. *J Am Chem Soc* 2009, **132**(2):470-471.

56. Smith AM, Mancini MC, Nie S: **Bioimaging: Second window for in vivo imaging**. *Nat Nano* 2009, **4**(11):710-711.

57. Tanaka E, Choi HS, Fujii H, Bawendi MG, Frangioni JV: **Image-guided oncologic surgery using invisible light: Completed pre-clinical development for sentinel lymph node mapping**. *Ann Surg Oncol* 2006, **13**(12):1671-1681.

58. Soltesz EG, Kim S, Laurence RG, DeGrand AM, Parungo CP, Dor DM, Cohn LH, Bawendi MG, Frangioni JV, Mihaljevic T: **Intraoperative sentinel lymph node**

mapping of the lung using near-infrared fluorescent quantum dots. *Ann Thorac Surg* 2005, **79**(1):269-277.

59. Soltesz EG, Kim S, Kim SW, Laurence RG, De Grand AM, Parungo CP, Cohn LH, Bawendi MG, Frangioni JV: **Sentinel lymph node mapping of the gastrointestinal tract by using invisible light**. *Annals of Surgical Oncology* 2006, **13**(3):386-396.

60. Kim S, Lim YT, Soltesz EG, De Grand AM, Lee J, Nakayama A, Parker JA, Mihaljevic T, Laurence RG, Dor DM *et al*: **Near-infrared fluorescent type II quantum dots for sentinel lymph node mapping**. *Nat Biotechnol* 2004, **22**(1):93-97.

61. Gao X, Cui Y, Levenson RM, Chung LWK, Nie S: **In vivo cancer targeting and imaging with semiconductor quantum dots**. *Nat Biotechnol* 2004, **22**(8):969-976.

62. Lingerfelt BM, Mattoussi H, Goldman ER, Mauro JM, Anderson GP: **Preparation of Quantum Dot−Biotin Conjugates and Their Use in Immunochromatography Assays**. *Analytical Chemistry* 2003, **75**(16):4043-4049.

63. Chen W, Peng C, Jin Z, Qiao R, Wang W, Zhu S, Wang L, Jin Q, Xu C: **Ultrasensitive immunoassay of 7-aminoclonazepam in human urine based on CdTe nanoparticle bioconjugations by fabricated microfluidic chip**. *Biosensors and Bioelectronics* 2009, **24**(7):2051-2056.

64. Bae PK, Kim KN, Lee SJ, Chang HJ, Lee CK, Park JK: **The modification of quantum dot probes used for the targeted imaging of his-tagged fusion proteins**. *Biomaterials* 2009, **30**(5):836-842.

65. Geho DH, Killian JK, Nandi A, Pastor J, Gurnani P, Rosenblatt KP: **Fluorescence-Based Analysis of Cellular Protein Lysate Arrays Using Quantum Dots**. *Methods Mol Biol* 2007, **374**:229-237.

66. Karlin-Neumann G, Sedova M, Falkowski M, Wang Z, Lin S, Jain M: **Application of Quantum Dots to Multicolor Microarray Experiments**. *Methods Mol Biol* 2007, **374**:239-251.

67. Yu G, Liang J, He Z, Sun M: **Quantum Dot-Mediated Detection of γ-Aminobutyric Acid Binding Sites on the Surface of Living Pollen Protoplasts in Tobacco**. *Chemistry & Biology* 2006, **13**(7):723-731.

68. Somers RC, Bawendi MG, Nocera DG: **CdSe nanocrystal based chem-/bio- sensors**. *Chemical Society Reviews* 2007, **36**(4):579-591.

69. Wong C, Stylianopoulos T, Cui J, Martin J, Chauhan VP, Jiang W, Popovic Z, Jain RK, Bawendi MG, Fukumura D: **Multistage nanoparticle delivery system for deep penetration into tumor tissue**. *Proceedings of the National Academy of Sciences* 2011, **108**(6):2426-2431.

70. Popović Z, Liu W, Chauhan VP, Lee J, Wong C, Greytak AB, Insin N, Nocera DG, Fukumura D, Jain RK *et al*: **A Nanoparticle Size Series for In Vivo Fluorescence Imaging**. *Angewandte Chemie International Edition* 2010, **49**(46):8649-8652.

Chapter 2. Development of a Bioorthogonal and Highly Efficient Conjugation Method for Quantum Dots using Tetrazine-Norbornene Cycloaddition[1]

2.1 Background and Motivation

Conventional quantum dot (QD) conjugation methods rely on functional groups such as amines, carboxylic acids, and thiols that are known to interact with the QD surface [1, 2]. Surface coordination of functional groups can limit the number of available groups for further coupling, resulting in low conjugation efficiencies [3]. An attractive alternative is to employ coupling chemistry that requires functional groups that do not coordinate to the QD surface. Click chemistries, such as the popular copper catalyzed azide-alkyne cycloaddition, are potential alternative conjugation strategies [4-6]. However, for catalyzed "click" chemistry, the requisite copper catalyst irreversibly quenches QD fluorescence (Figure 2-1). Additionally, catalyst-free strain-promoted click reactions are limited by poor aqueous solubility of substrates and tedious syntheses [7, 8]. Recently, there have been a number of examples that use inverse-electron-demand Diels-Alder cycloadditions involving tetrazine and strained alkenes as an alternative bioorthogonal conjugation method [9-11]. This chemistry benefits from sufficiently rapid kinetics in that no catalyst is required. Recently, our collaborators have developed a tetrazine derivative [3-(4-benzylamino)-1,2,4,5-tetrazine] (BAT) that shows good stability in buffer and serum, and high reaction rate when reacted with strained olefins such as norbornene (Scheme 1, 2 $M^{-1}s^{-1}$ at 20 °C) [12] or *trans*-cyclooctene (~6000 $M^{-1}s^{-1}$ at 37 °C) [13].

[1] Much of this chapter has appeared in print. It is reproduced with permission from *J Am Chem Soc* 2010, **132**: 7838-7839

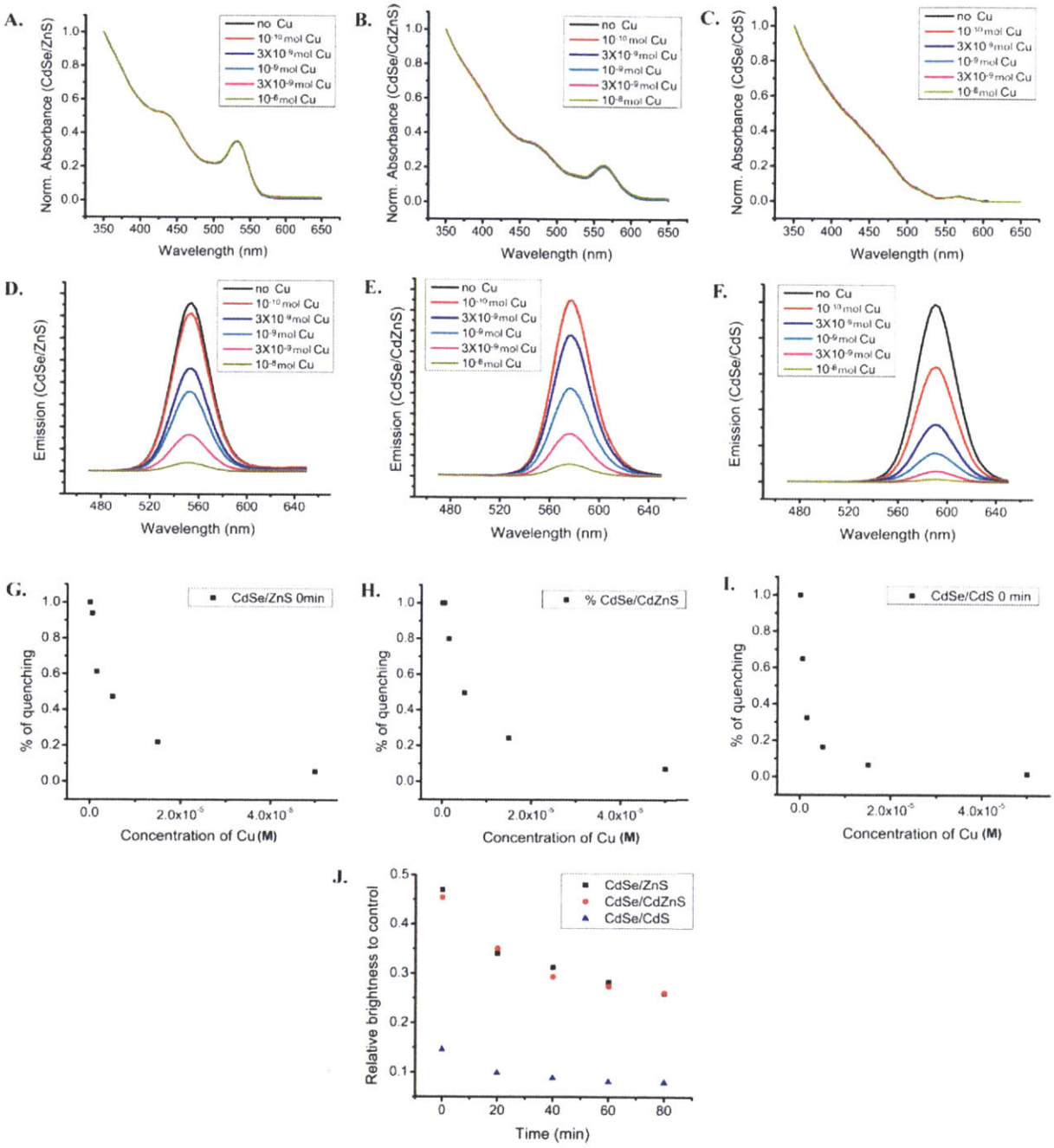

Figure 2-1 Quenching of QDs using Cu (I) ions. Absorption (A-C) and emission (D-F) spectra of 1μM of QDs (in 200μL 0.1× PBS) after adding varying concentrations of Cu(I) (0 min). (G-I) Relative emission intensity of the samples with varying concentration of Cu(I) to the control sample without Cu(I) (0min). (J) Drop of the relative emission intensity of the QD samples with 1×10^{-9} mol of Cu(I) over time. (A, D, and G) are for CdSe/ZnS (5 monolayers of ZnS), (B, E, and H) are for CdSe/$Cd_{0.3}Zn_{0.7}S$ (5 monolayers of $Cd_{0.3}Zn_{0.7}S$) and (C, F, and I) are for CdSe/CdS(4 monolayers of CdS). The experimental data shows that CdS coated CdSe is most prone to quenching by Cu(I). For all samples, an immediate drop of fluorescence is followed by

a gradual decay of the emission intensity after the copper addition and the quenching is irreversible. In general procedures for "click" chemistry [5, 14-16] on nanoparticles, $>10^{-6}$ mol of Cu(I) is used as a catalyst for ~ 10^{-10} mole of nanoparticles. With 10^{-6} mol of Cu(I), we observed almost no emission from CdSe/ZnS, CdSe/$Cd_{0.3}Zn_{0.7}S$, or CdSe/CdS.

Utilizing the non-coordinating properties of the substrates and the fast reaction rate, we explored norbornene-tetrazine cycloaddition as a new, efficient conjugation method on QDs (Scheme 1). Carboxylic acid modified norbornene (bicyclo[2.2.1]hept-5-en-2-yl acetic acid) was selected for this study as it is commercially available and the carboxylic acid group allows further conjugation to other molecules.

Scheme 1 Click chemistry between BAT and norbornene.

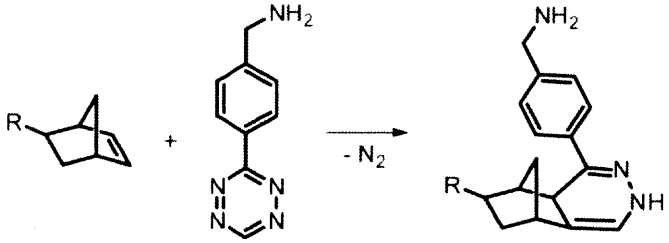

BAT

In this chapter, we present a bioorthogonal and modular conjugation method to efficiently couple organic dyes and bio-molecules to QDs using a norbornene and tetrazine cycloaddition. The use of non-coordinating functional groups combined with the rapid rate of the cycloaddition leads to highly efficient conjugation. We apply this method to the *in situ* targeting of norbornene coated QDs to live cancer cells that are labeled with tetrazine modified proteins.

2.2 Synthesis of Norbornene Modified Polymeric Imidazole Ligands (NB-PIL) and 3-(4-benzylamino)-1,2,4,5-tetrazine

The cycloaddition was achieved by functionalizing QDs with norbornene and reacting with BAT-modified substrates. Polymeric imidazole ligands (PILs) were used to prepare norbornene-coated water soluble QDs. PILs are random copolymers incorporating poly(ethylene) glycol (PEG), amino-PEG_{11}, and imidazole groups for water solubilization, functionalization, and QD binding, respectively [3]. The modularity of the polymer and commercial availability of the norbornene allows facile incorporation of norbornene groups on the polymer in gram scale. For this study, poly(amino-PEG_{11})$_{20\%}$-PIL (NH_2-PIL), composed of 30% poly(ethylene) glycol (PEG_{12}), 20% amino-PEG_{11}, and 50% imidazole groups, was further modified with n-hydroxysuccinimide(NHS) activated bicyclo[2.2.1]hept-5-en-2-yl acetic acid (norbornene) via amide coupling (Figure 2-2A). Complete conversion of amines to norbornenes was confirmed by probing free amine in the polymer before and after the conjugation with fluorescamine, an amine-reactive fluorogenic probe (Figure 2-3). Norbornene-coated QDs were prepared by ligand exchange of natively capped QDs with the norbornene modified PIL (NB-PIL) (Figure 2-2B). Gel filtration chromatography (GFC) data confirm that norbornene-coated QDs are well dispersed in buffers without forming aggregates (Figure 2-4).

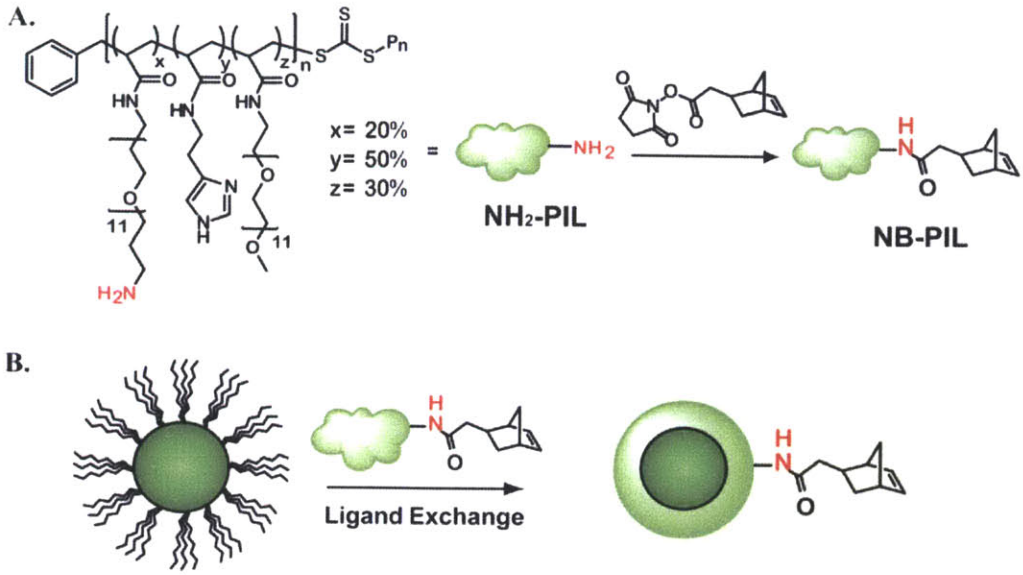

Figure 2-2 (A) Conjugation of norbornene to 20% NH_2-PIL polymer (B) Ligand exchange of the native ligands of the QDs with the NB-PILs.

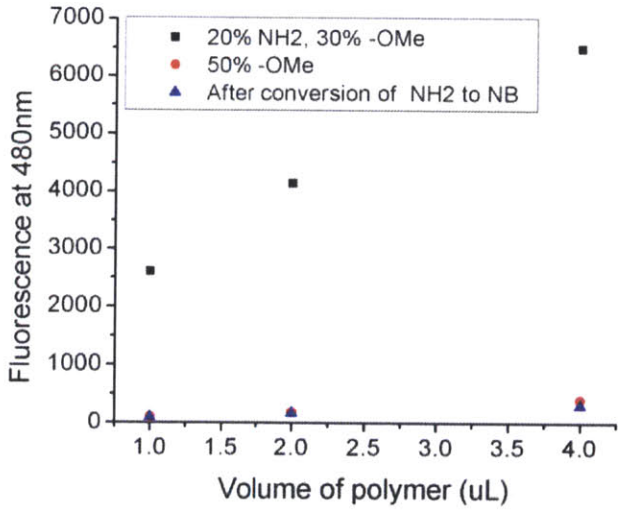

Figure 2-3 Probing free amines in different polymer samples using fluorescamine. Black square is poly(amino-PEG_{11})$_{20\%}$-PIL, red circle is poly(PEG_{12})-PIL, blue triangle is after converting the amine of poly(amino-PEG_{11})$_{20\%}$-PIL to norbornene (NB-PIL). Fluorescence of NB-PIL being similar level as poly(PEG_{12})-PIL proves that the conversion was complete.

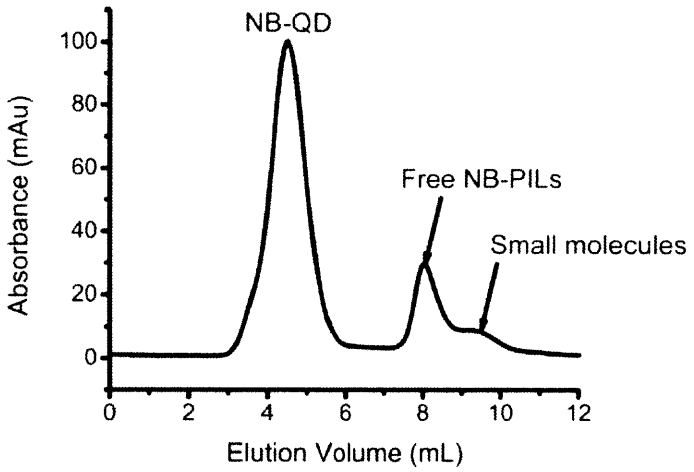

Figure 2-4 A representative GFC trace of NB-PIL QDs with a retention time of 4.5 minutes corresponding to a hydrodynamic radius of ~11 nm. The peak at 8 min corresponds to the free NB-PIL ligand, and the peak at 9.4 min corresponds to the small molecule byproducts that are formed during the modification of the poly(amino-PEG_{11})$_{20\%}$-PILs to NB-PILs.

2.3 Conjugation of Organic Dyes Using Tetrazine-Norbornene Cycloaddition

To determine conjugation efficiencies of the cycloaddition on QDs, norbornene-coated QDs were conjugated with BAT modified Alexa594 (Alexa-BAT) (Figure 2-5A). Representative absorption and emission spectra of the QD-Alexa conjugates are shown in Figure 2-5B and C. Coupling yields were determined through knowledge of the extinction coefficients of the dye and QDs, along with measurement of the product absorption spectra. The number of Alexa dyes conjugated to the norbornene coated QDs varied depending on the excess of Alexa-BAT (Figure 2-6A and B). The ratio of QDs to Alexa594 in the QD-Alexa conjugates was calculated using the absorption values of the QDs and Alexa594 at 350 nm and 590 nm respectively (Table 1).

Increasing the dye concentration to 100× excess led to a saturation coupling yield of ~16 dyes/QD. We believe that this number effectively represents the average number of reactive

norbornene molecules on the surface of each QD. One should be able to increase the number of coupled dyes by further increasing the composition of norbornenes in the starting polymer.

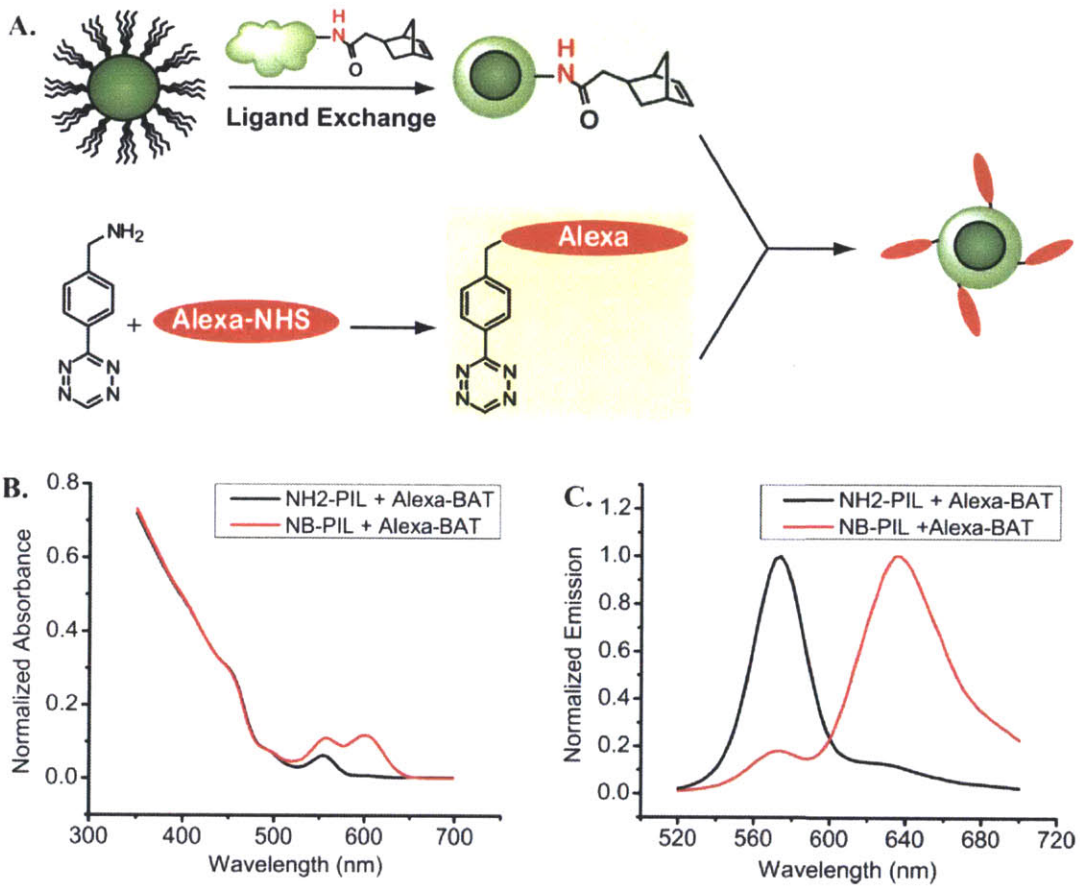

Figure 2-5 (A) Conjugation of BAT modified Alexa 594 to QDs using tetrazine-norbornene cycloaddition. Representative (B) absorption and (C) emission spectra of the QD-dye conjugates (~4 dye/dot) and the control samples without norbornene.

Table 1 QD-Alexa 594 conjugation ratios. Concentrations were measured based on ε_{dye} = 90,000 $cm^{-1}M^{-1}$ at 590nm for Alexa 594, and ε_{QD} = 2,630,000 $cm^{-1}M^{-1}$ at 350nm for QD570.

Mixed Dye:QD Ratio	QD Abs @ 350 nm	QD Conc. (μM)	Dye Abs @ 590 nm	Dye Conc. (μM)	Dye:QD Ratio
10	0.251	0.0954	0.0350	0.388	4.07
40	0.425	0.162	0.165	1.83	11.3
100	0.431	0.164	0.245	2.72	16.6
200	0.442	0.168	0.232	2.58	15.4

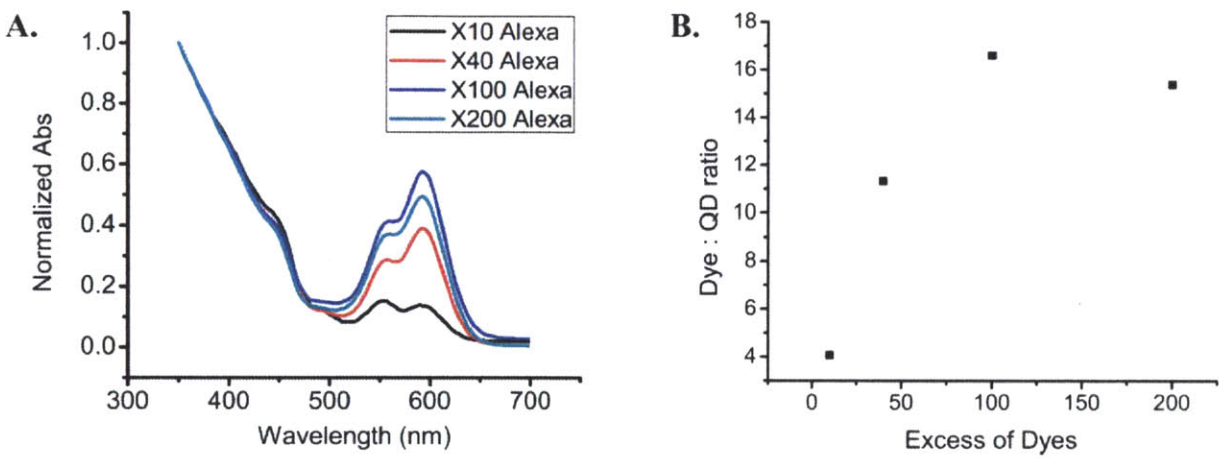

Figure 2-6 (A) Absorbance spectra of QD-Alexa conjugates which were prepared by mixing carrying concentrations of the dye (B) Calculated Alexa to QD ratios for the purified conjugates.

2.4 *In vitro* Labeling Using QD-Protein Conjugates Prepared Using Tetrazine-Norbornene Cycloaddition

To illustrate the utility of the coupling chemistry for live cell imaging with QDs, we labeled epidermal growth factor receptors (EGFRs) overexpressed on the surface of human skin cancer cells. Cellular labeling was achieved either directly through use of pre-formed QD-EGF conjugates (Figure 2-7B) or by performing *in situ* conjugation of the norbornene-coated QDs to BAT modified EGFs on the cell surface (Figure 2-7C). For direct labeling, the norbornene coated QDs were coupled with BAT modified EGF (Figure 2-7A), and 50 nM of the resulting QD-EGF conjugates were added to the A-431 human carcinoma cells at 4 °C for 30 mins (Figure 2-8). Note that the quantum yield (QY) of the QDs stayed constant before and after the conjugation of EGF to the QDs (Figure 2-9). By using low concentration of the QDs, we observed single QDs that are characterized by their fluorescence intermittency (Figure 2-10). For *in situ* conjugation, cells were incubated with 200 nM BAT modified EGF (BAT-EGF) at 4 °C for 30 minutes and

labeled with 800 nM of norbornene coated QD at 37 °C for 30 mins (Figure 2-8D). Control experiments using the same procedures but with QDs coated with poly(PEG_{12})-PIL, composed of 50 % imidazole and 50% PEG_{12} (without norbornene), are shown in Figure 2-8A and 2-8C.

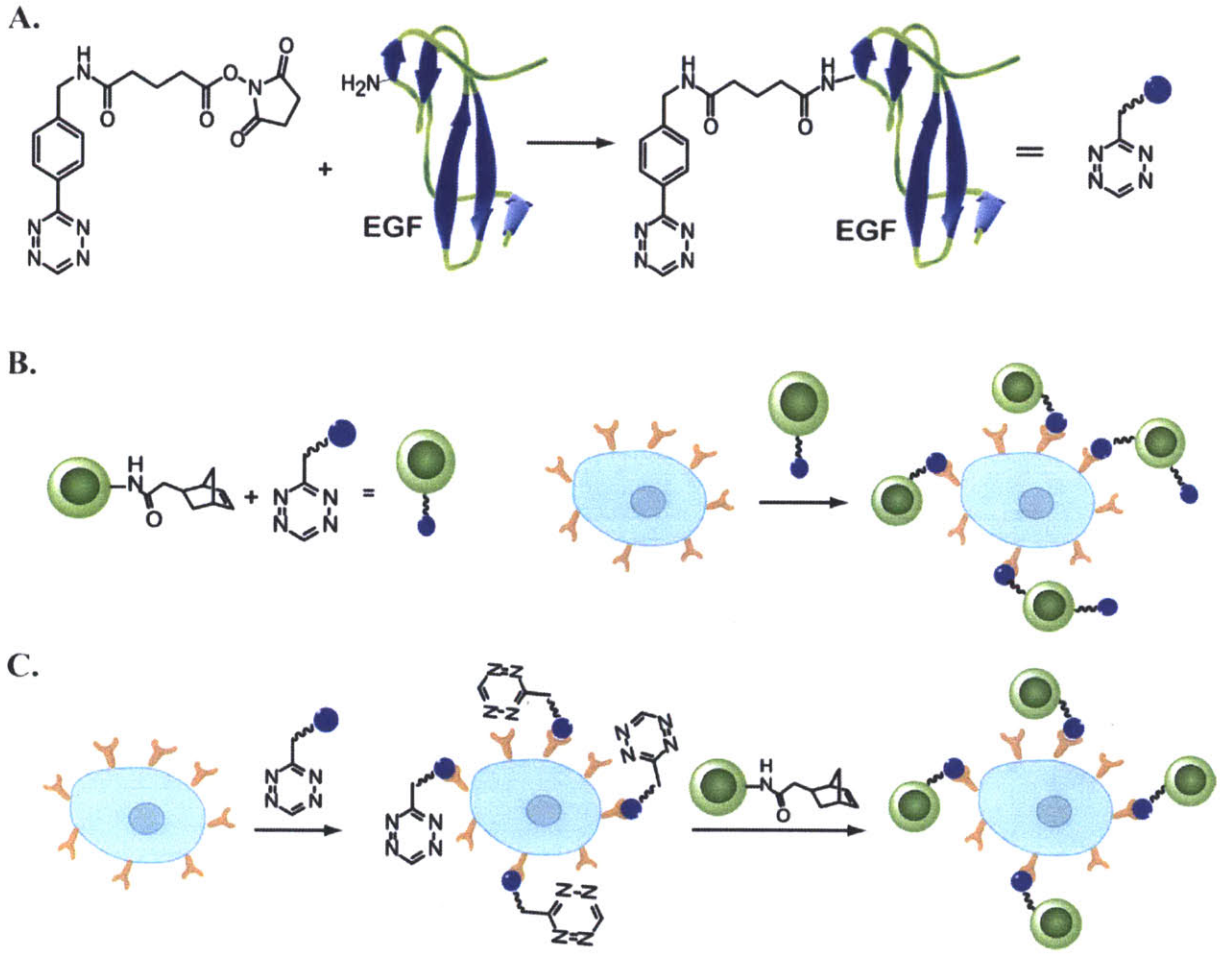

Figure 2-7 (A) Conjugation of NHS-activated BAT to EGF. (B) Labeling of cells with pre-formed QD-EGF constructs. (C) *In situ* conjugation of norbornene-functionalized QDs to BAT-EGF on live cells.

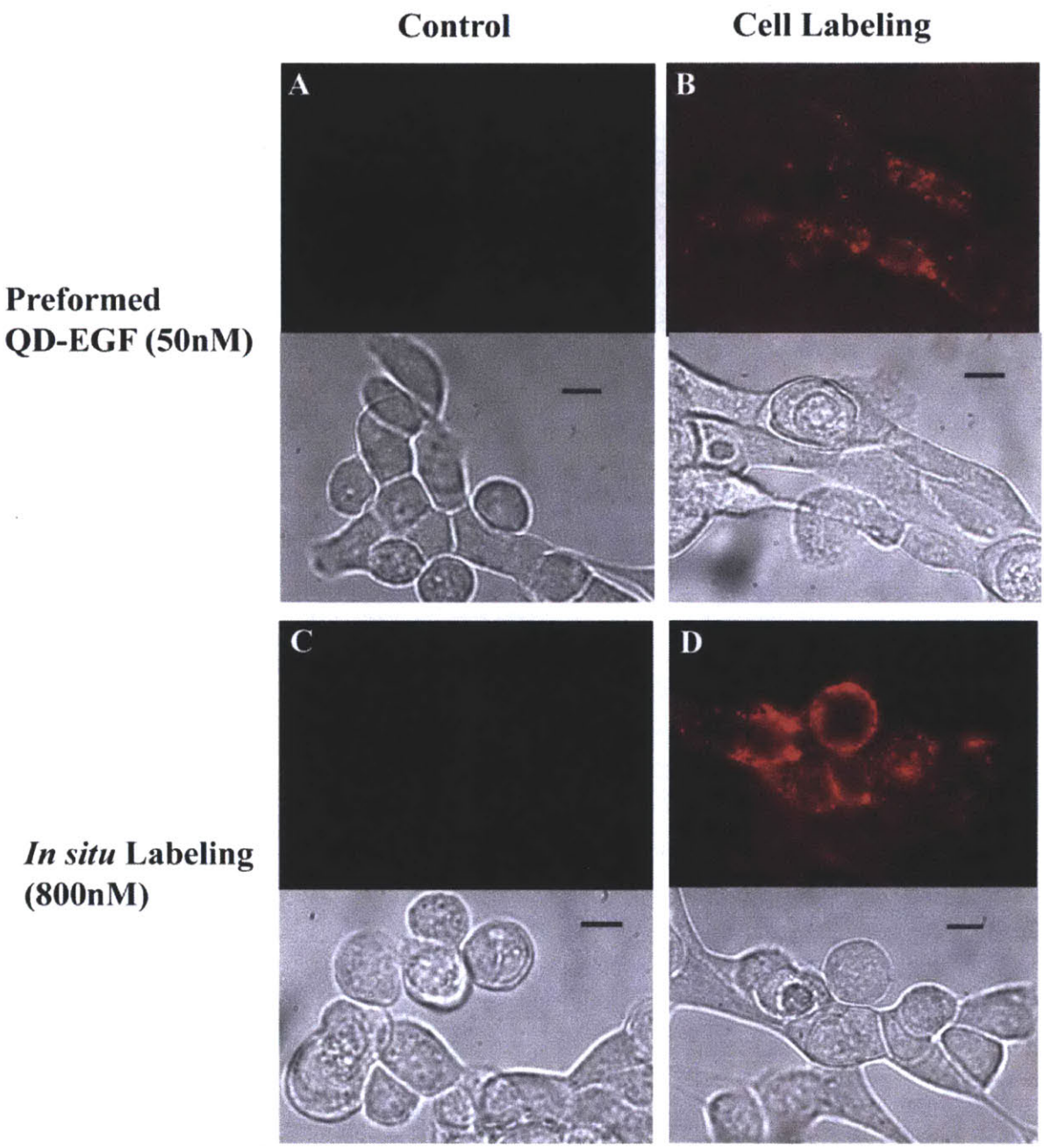

Figure 2-8 Targeting of QDs to A431 squamous cancer cells using norbornene-tetrazine cycloaddition. Top: QD fluorescence at 605 nm with excitation at 488 nm. Bottom: corresponding DIC images (scale bar 10 μm). Cells were targeted either by (B) using preformed QD-EGF complexes (50 nM) for single QD tracking or by (D) performing *in situ* conjugation using norbornene-functionalized QDs (800 nM) on BAT-EGF-modified cell surfaces for ensemble labeling. (A) and (C) are control experiment with poly(PEG_{12})-PIL QDs (without norbornene).

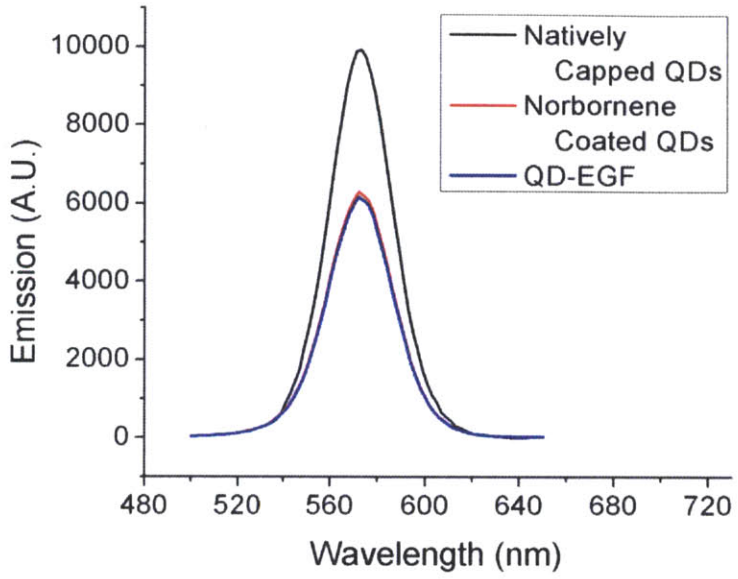

Figure 2-9 Emission spectra of native QDs (black, QY ~100% in octane) and norbornene coated QDs before (red, QY ~60% in 1×PBS) and after conjugation with EGF *via* norbornene-tetrazine cycloaddition (blue, QY ~60% in 1×PBS). The initial quantum yield of norbornene coated QDs is retained after the norbornene-tetrazine cycloaddition.

Figure 2-8 shows that successful labeling is achieved using either type of labeling technique. The fast rate of the coupling reaction in serum allowed for *in situ* conjugation of norbornene-coated QDs to BAT-EGF labeled cells. In addition, this method does not result in an increased QD size, and in general works on cells with endogenously expressed receptors.

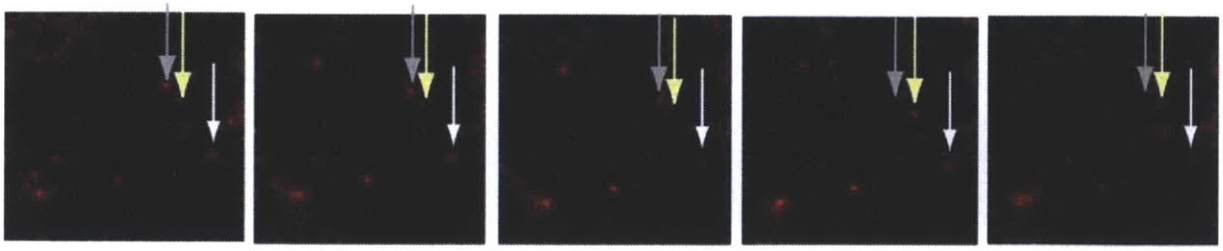

Figure 2-10 Time series of (from left to right) single QDs (arrows) bound to the surface of A431 squamous cancer cells showing blinking. Each frame was acquired with a 200 ms exposure time.

2.5 Conclusion

In summary, we developed an efficient conjugation method for QDs utilizing the inverse Diels-Alder cycloaddition between tetrazine and norbornene. The rapid kinetics combined with the tolerance of the reaction to functional groups abundant in cells allows labeling of proteins of interest on cells *in situ*. The conjugation approach presented here is modular and can be extended to many biological imaging applications, as tetrazine and norbornene functionalities can be easily conjugated to carboxylic acid or amine containing molecules.

2.6 Experimental Section

2.6.1 Materials and Instrumentation

All chemicals were purchased from Sigma Aldrich unless noted and were used as received. Selenium shot, cadmium oxide 99.999%, and n-tetradecylphosphonic acid (TDPA) were purchased from Alfa Aesar (Ward Hill, MA). Trioctylphosphine (TOP) and tributylphospine (TBP) were purchased from Strem Chemicals (Buchs, Switzerland). Epithermal Growth Factor (EGF, Human recombinant) and Alexa Fluor® 594 carboxylic acid, succinimidyl ester was purchased from Invitrogen. (1S,2S,4S)-bicyclo[2.2.1]hept-5-en-2-yl acetic acid was purchased from ChemBridge. All solvents were of reagent grade or higher and were used without further purification.

Tributylphosphine selenide (TBP-Se) was prepared by dissolving 0.15 mmol of selenium shot in 100 mL of TBP under inert atmosphere and stirring vigorously overnight, forming a 1.5 M TBP-Se solution. All air sensitive materials were handled in an Omni-Lab VAC glove box

under dry nitrogen atmosphere with oxygen levels < 0.2 ppm. All solvents were spectrophotometric grade and purchased from EMD Biosciences.

Analytical HPLC and LC/MS were performed on a Waters 2695 HPLC equipped with a 2996 diode array detector, a Micromass ZQ4000 ESI-MS module, and a Grace-Vydac RPC18 column (model 218TP5210) at a flow rate of 0.3 mL/min. Preparative HPLC was performed on a Varian ProStar model 210 instrument equipped with a model 335 diode array detector, a model 701 fraction collector, and a Varian RPC18 column (model A6002250X212) at a flow rate of 21 mL/min. All UV/vis spectra were recorded on an Agilent 8453 diode array UV/vis spectrophotometer.

Photoluminescence and absorbance spectra were recorded with a BioTek Synergy 4 Microplate Reader. The absorbance of all solutions was kept below 0.1 OD to avoid inner-filter effects. Flash column chromatography was performed on a Teledyne Isco CombiFlash Companion. Polymer molecular weights were determined in DMF solutions on an Agilent 1100 series HPLC/GPC system with three PLgel columns (103, 104, 105 Å) in series against narrow polystyrene standards.

2.6.2 Synthesis

Synthesis of CdSe(CdS). CdSe cores with 480nm first absorption peak were synthesized using a previously reported method [17]. To summarize, 0.4 mmol (54.1mg) of CdO, 0.8 mmol (0.2232g) of TDPA, 9.6mmol (3.72g) of TOPO were placed in 25mL round bottom flask. The solution was degassed for 1 hr at 160 °C and heated to 300 °C under argon until the CdO dissolved and formed a clear homogenous solution. This was followed by putting the solution under vacuum at

160 °C to remove the evolved water. The solution was reheated to 360°C under argon and a TBP-Se solution (1.5mL of 1.5M TBP-Se in 1.5mL of TOP) was rapidly added to give CdSe cores with the first absorption feature at 468nm. The cores were then grown further at 260°C to produce cores with the desired wavelength for the first absorption feature.

CdS shells were deposited on CdSe cores via modification of previously reported procedures [3]. Cores isolated by repeated precipitations from hexane with acetone were brought to 180 °C in a solvent mixture of oleylamine (3 mL) and octadecene (6 mL). Aliquots of Cd and S precursor solutions were then introduced alternately starting with the metal (Cd) and waiting 15 min between the start of each addition. The Cd precursor consisted of 0.33 mmol Cd-oleate and 0.66 mmol oleylamine in a solvent mixture of octadecene (1.5 mL) and TOP (3 mL). The S precursor consisted of 0.3 mmol hexamethyldisilathiane [$(TMS)_2S$] in 6 mL TOP. The dose of each overcoating precursor aliquot corresponds to adding a single monolayer of atoms to the QD surface. Addition of a total of 4 aliquots each of Cd and S yielded QDs with emission at 570 nm and a quantum yield close to unity when diluted in octane. A similar procedure was performed on larger CdSe cores [18, 19] to obtain CdSe(CdS) QDs emitting at 605 nm. The extinction coefficient of CdSe(CdS) was calculated using the extinction coefficient of CdSe cores from the literature4 and assuming that 100% of the CdSe cores were retained during the overcoating step. Figure 2-11shows a transmission electron microscopy (TEM) image of the resulting CdSe(CdS) QDs.

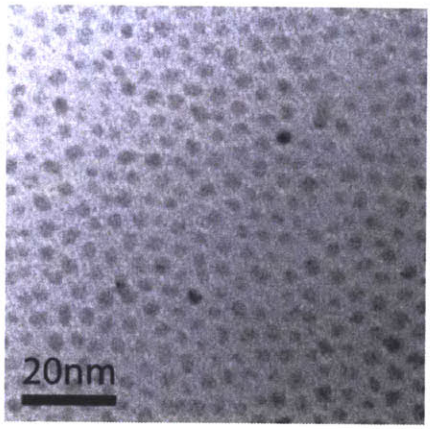

Figure 2-11 TEM of CdSe(CdS) (λ_{em}=570nm) with inorganic size ~4.6 nm.

Preparation of amine-reactive tetrazine (Tz-NHS). 2,5-dioxopyrrolidin-1-yl 5-(4-(1,2,4,5-tetrazin-3-yl)benzylamino)-5-oxopentanoate (Tz-NHS) was prepared from 3-(4-benzylamino)-1,2,4,5-tetrazine (Tz-benzylamine) that was synthesized as previously described [12]. Tz-benzylamine (10 mg) was added to a solution of methylene chloride containing 6 mg glutaric anhydride. The solution was stirred overnight at 50°C. The methylene chloride was removed by rotary evaporation and the crude mixture was purified by column chromatography resulting in 5-(4-(1,2,4,5-tetrazin-3-yl)benzylamino)-5-oxopentanoic acid (Tz-acid) in quantitative yield. This acid was then immediately introduced to an acetonitrile (2 mL) solution of N, N'-disuccinimidyl carbonate (68 mg) and triethylamine (30 mg) and allowed to stir at room temperature until the reaction reached completion (monitored by TLC). The acetonitrile was removed by rotary evaporation and the crude mixture purified by column chromatography yielding 17 mg (80% yield) of the desired Tz-NHS. 1HNMR (400 MHz CDCl3): δ 10.3-10.2 (s, 1H), 8.7-8.5 (d, 2H), 7.6-7.4 (d, 2H), 6.6-6.2 (br, 1H), 4.7-4.4 (m, 2H), 3.1-2 (m, 10H). LR-MS [M+H]+ calc mass 399.1 found mass 399.2.

Synthesis of norbornene conjugated polymeric imidazole ligands (NB-PIL). Poly(amino-PEG11)20%-PIL was synthesized using a previously reported method [3]. (1S,2S,4S)-bicyclo[2.2.1]hept-5-en-2-yl acetic acid (norbornene) was activated by reacting 0.05 moles of (1S,2S,4S)-bicyclo[2.2.1]hept-5-en-2-yl acetic acid with 0.06 moles n-hydroxysuccinimide (NHS) and 0.06mol N,N'-Dicyclohexylcarbodiimide (DCC) in anhydrous tetrahydrofuran (THF) for 2 hours at room temperature. NHS activated norbornene was reacted with Poly(amino-PEG11)20%-PIL in dry THF overnight (2 times excess of norbornene was added to the number of the amine groups in the polymer). After the reaction was completed, THF was removed by vacuum and the reaction mixture was redissolved in ethylacetate to precipitate the byproducts. Precipitates were filtered out using a 0.2 μM PTFE syringe filter. This workup was repeated several times until no precipitate was observed after removal of the solvent.

Preparation of norbornene coated water soluble QDs. Ligand exchange of native QDs with NB-PIL was performed as described in literature [3]. To summarize, QDs (1 nmol) were precipitated using hexanes (30 μL), CHCl3 (30 μL) and EtOH(200 μL) and brought into 50 μL of CHCl3. The QD stock solution was mixed with a solution of NB-PIL (4 mg) in CHCl3 (30 μL), and stirred for 20 min at RT, after which 30 μL of MeOH was added followed by stirring for an additional 20 min. QD samples were precipitated by the addition of EtOH (30 μL), CHCl3 (30 μL), and excess hexanes. The sample was centrifuged at 4,000 g for 2 minutes. The clear supernatant was discarded, and the pellet dried *in vacuo*, followed by the addition of PBS (500 μL, pH 7.4). The aqueous sample was then filtered through a 0.2 μm syringe filter before use. Prior to any conjugation chemistry or cell studies, free ligand was removed by three cycles of dilution/concentration through an Amicon Ultra Ultracel 50,000 Da MW cutoff filter (Millipore).

The quantum yield of norbornene coated QDs was about 60%. (Quantum yield of natively capped QDs was ~100%).

Synthesis of 3-(4-benzylamino)-1,2,4,5-tetrazine conjugated Alexa 594. Alexa Fluor® 594 carboxylic acid, succinimidyl ester (Alexa 594) was reactivated with n-hydroxysuccinimide by adding 1.2equiv of NHS and 1.2equiv of DCC in dry DMF and reacted for 2 hours at room temperature. 1 equiv of 3-(4-benzylamino)-1,2,4,5-tetrazine was added to the solution and reacted overnight at room temperature. Completion of the reaction was confirmed using ninhydrin staining.

Synthesis of EGF-BAT. Amine reactive tetrazine (4mg/mL) was reactivated with n-hydroxysuccinimide by adding 1.2 equiv of NHS and 1.2 equiv of DCC in dry DMF and reacted for 2 hours at room temperature. 50μg of EGF was dissolved in 200μL 1X PBS and 1.2 equiv of NHS activated tetrazine was added to the solution and reacted overnight at room temperature. The conjugates were dialyzed three times with an Amicon Ultra Ultracel 3,000 Da Mw cutoff filter (Millipore) to remove excess NHS, DCC and byproducts.

Synthesis of QD-Alexa594 conjugates. 200μL of ~1μM norbornene coated QDs were mixed with different concentrations of Alexa594 tetrazine in 1X PBS and reacted for 4 hrs at 37 °C. Excess reagents were removed by gel filtration chromatography and dialyzed three times with 1× PBS using Amicon Ultra Ultracel 50,000 Da MW cutoff filter. The control experiments were performed using Poly(amino-PEG_{11})$_{20\%}$-PIL coated QDs. Final materials were analyzed by UV-Vis absorption to determine the number of dyes on the QD surface. Concentrations of QDs and Alexa 594 were measured based on ε_{dye} = 90,000 $cm^{-1}M^{-1}$ at 590nm for Alexa 594, and ε_{QD} = 2,630,000 $cm^{-1}M^{-1}$ at 350nm for QD570.

Synthesis of QD-EGF. 0.2nmol of norbornene coated QDs and 0.4 nmol of EGF-tetrazine were mixed in 1X PBS with a final concentration of 1μM for QDs and incubated for 2 hrs at 37 °C. Unreacted EGF was removed by three cycles of dilution/concentration through an Amicon Ultra Ultracel 50,000 Da MW cutoff filter (Millipore).

2.6.3 Characterization Methods

Fluorescamine Assay of Amine Reactivity PILs. Stock solutions of amine-containing PIL polymers were made at 20 mg/mL concentration. A serial dilution was made using 1, 2, and 4 μL of polymer stock into 240 μL of PBS buffer, followed by addition of 10 μL of a 30 mg/mL solution of fluorescamine in acetone. This mixture was vortexed and incubated at room temperature for 1 hour before fluorescence analysis on a BioTek plate reader with excitation at 380 nm and detection at 480 nm. The recorded fluorescence intensity signals were calibrated against solutions of known concentrations of methoxyPEG11-NH2.

Quantum yield (QY) of QDs. The QY of QD570 was measured relative to Rhodamine 610 (QY 68% in ethanol) with excitation at 505 nm and the QY of QD605 was measured relative to Rhodamine 640 (QY 100% in ethanol with excitation at 535nm). Solutions of QDs in octane (native CdSe/CdS QDs) or PBS (QDs after ligand exchange with either Poly(amino-PEG_{11})$_{20\%}$-PIL or NB-PIL) and dye in ethanol were optically matched at the excitation wavelength. Fluorescence spectra of QD and dye were taken under identical spectrometer conditions in quadruplicate and averaged. The optical density was kept below 0.1 at the λ_{max}, and the integrated intensities of the emission spectra, corrected for differences in index of refraction and concentration, were used to calculate the quantum yields using the expression QY_{QD} =

$(Absorbance)_{dye}/(Absorbance)_{QD} \times (Peak\ Area)_{QD} /(Peak\ Area)_{Dye} \times (nQD\ solvent)^2/(nDye\ solvent)^2 \times QY_{Dye}$.

Gel Filtration Chromatography (GFC). GFC was performed using an ÄKTAprime Plus chromatography system from Amersham Biosciences equipped with a self-packed Superdex 200 10/100 column. PBS (pH 7.4) was used as the mobile phase with a flow rate of 1.0 mL/min. Detection was achieved by measuring the absorption at 280 nm.

Transmission Electron Microscopy. The inorganic size of CdSe(CdS) QDs was determined using a JEOL 200CX TEM operating at 200 kV. One drop of a dilute sample of QDs in hexane precipitated two times using acetone was placed onto a Formvar coated copper grid, allowed to settle for 20 seconds, and wicked away using an absorbent tissue. Size analysis was performed on captured digital images using ImageJ 1.34s.

Cell culture and labeling. A-431 human epidermoid carcinoma cells were grown in DMEM (Invitrogen) with 10% Fetal Bovine Serum (Invitrogen), 50 μg /mL penicillin and 50 μg /mL streptomycin (Invitrogen). When labeling cells with preformed QD-EGF conjugates (Figure 2B), cells were rinsed with 4 °C 1% Bovine Serum Albumin (BSA) in PBS and incubated with 50 nM QD-EGF conjugates at 4 °C for 30 minutes. For *in situ* click conjugation between tetrazine and norbornene on cells (Figure 2C), cells were rinsed with 4 °C 1% BSA in PBS, incubated with 200 nM EGF-BAT at 4°C for 30 minutes, and then rinsed three times with 1% BSA in PBS to block non-specific binding. Subsequently, norbornene coated QDs at varying concentrations were added to the cells and incubated for 30 minutes at 37°C. The cells were then washed three times with 25°C PBS to remove excess QDs.

Fluorescence imaging. Cells were imaged with an epifluorescence microscope (Nikon) with a 60× water-immersion objective and Princeton instruments MicroMax Camera with a 1.5× magnification tube lens. Bright field images were collected using differential interference contrast with an exposure time of 100 ms and fluorescence images were collected by exciting with a 488 nm Argon-ion laser line combined with a D605/30M emission filter. Exposure times for fluorescence imaging were 200 ms for QD blinking time-lapse imaging and 500 ms for all others. All fluorescence image frames were background corrected using Matlab.

Copper quenching. To verify that copper (I) ions quench the QD fluorescence irreversibly, 2×10^{-10} mol of CdSe/ZnS (5 monolayers of ZnS), CdSe/$Cd_{0.3}Zn_{0.7}S$ (5 monolayers of $Cd_{0.3}Zn_{0.7}S$) and CdSe/CdS (4 monolayers of CdS) coated with poly (PEG_{12})-PIL in 0.1×PBS were incubated with varying concentrations of Cu(I). Cu(I) was generated *in situ* by reducing Cu(II) with sodium ascorbate.

100 mmol of $CuSO_4$ and 500 mmol of sodium ascorbate were dissolved in 1mL of 0.1× PBS (Solution A). 1 μL, 3 μL, 10μL, 30μL, and 100 μL of solution A was added to 2×10^{-10} mmol of QDs and the final volume was adjusted to 200 μL (0.1× PBS). Absorption and emission spectra of the samples were measured at 0min, 20min, 40min, 60min, and 80min after the copper addition.

2.7 References

1. Medintz I, Uyeda H, Goldman E, Mattoussi H: **Quantum dot bioconjugates for imaging, labelling and sensing**. *Nat Mater* 2005, **4**:435-446.

2. Allen PM, Liu W, Chauhan VP, Lee J, Ting AY, Fukumura D, Jain RK, Bawendi MG: **InAs(ZnCdS) Quantum Dots Optimized for Biological Imaging in the Near-Infrared.** *J Am Chem Soc* 2009, **132**(2):470-471.

3. Liu W, Greytak AB, Lee J, Wong CR, Park J, Marshall LF, Jiang W, Curtin PN, Ting AY, Nocera DG *et al*: **Compact Biocompatible Quantum Dots via RAFT-Mediated Synthesis of Imidazole-Based Random Copolymer Ligand.** *J Am Chem Soc* 2010, **132**(2):472-483.

4. Hartmuth CK, Finn MG, Sharpless KB: **Click Chemistry: Diverse Chemical Function from a Few Good Reactions.** *Angew Chem Int Ed* 2001, **40**(11):2004-2021.

5. Binder WH, Sachsenhofer R, Straif CJ, Zirbs R: **Surface-modified nanoparticles via thermal and Cu(i)-mediated "click" chemistry: Generation of luminescent CdSe nanoparticles with polar ligands guiding supramolecular recognition.** *J Mater Chem* 2007, **17**(20):2125-2132.

6. Brennan JL, Hatzakis NS, Tshikhudo TR, Razumas V, Patkar S, Vind J, Svendsen A, Nolte RJM, Rowan AE, Brust M: **Bionanoconjugation via Click Chemistry: The Creation of Functional Hybrids of Lipases and Gold Nanoparticles.** *Bioconjug Chem* 2006, **17**(6):1373-1375.

7. Baskin JM, Prescher JA, Laughlin ST, Agard NJ, Chang PV, Miller IA, Lo A, Codelli JA, Bertozzi CR: **Copper-free click chemistry for dynamic in vivo imaging.** *Proc Natl AcadSci* 2007, **104**(43):16793-16797.

8. Codelli JA, Baskin JM, Agard NJ, Bertozzi CR: **Second-Generation Difluorinated Cyclooctynes for Copper-Free Click Chemistry.** *J Am Chem Soc* 2008, **130**(34):11486-11493.

9. Soloducho J. DJ, Cabaj J., Roszak S.: **Practical synthesis of bis-substituted tetrazines with two pendant 2-pyrrolyl or 2-thienyl groups, precursors of new conjugated polymers.** *Tetrahedron* 2003, **59**:4761–4766.

10. Kämpchen T. MW, Overheu W., Schmidt R., Seitz G.: **Zur kenntnis von reaktionen des 1,2,4,5-tetrazin-3,6-dicarbonsäure-dimethylesters mit nucleophilen.** *Chem Ber* 1982, **115**:683–694.

11. Blackman ML, Royzen M, Fox JM: **Tetrazine Ligation: Fast Bioconjugation Based on Inverse-Electron-Demand Diels'Alder Reactivity.** *J Am Chem Soc* 2008, **130**(41):13518-13519.

12. Devaraj NK, Weissleder R, Hilderbrand SA: **Tetrazine-Based Cycloadditions: Application to Pretargeted Live Cell Imaging**. *Bioconjug Chem* 2008, **19**(12):2297-2299.

13. Devaraj NK, Upadhyay R, Haun JB, Hilderbrand SA, Weissleder R: **Fast and Sensitive Pretargeted Labeling of Cancer Cells through a Tetrazine *trans*-Cyclooctene Cycloaddition**. *Angew Chem Int Ed* 2009, **48**(38):7013-7016.

14. Boisselier E, Salmon L, Ruiz J, Astruc D: **How to very efficiently functionalize gold nanoparticles by "click" chemistry**. *Chem Commun* 2008(44):5788-5790.

15. Brennan JL, Hatzakis NS, Tshikhudo TR, Razumas V, Patkar S, Vind J, Svendsen A, Nolte RJM, Rowan AE, Brust M: **Bionanoconjugation via Click Chemistry: The Creation of Functional Hybrids of Lipases and Gold Nanoparticles**. *Bioconjugate Chem* 2006, **17**(6):1373-1375.

16. Polito L, Monti D, Caneva E, Delnevo E, Russo G, Prosperi D: **One-step bioengineering of magnetic nanoparticles via a surface diazo transfer/azide-alkyne click reaction sequence**. *Chem Commun* 2008(5):621-623.

17. Peng ZA, Peng X: **Formation of High-Quality CdTe, CdSe, and CdS Nanocrystals Using CdO as Precursor**. *J Am Chem Soc* 2001, **123**(1):183-184.

18. Snee PT, Chan Y, Nocera DG, Bawendi MG: **Whispering-Gallery-Mode Lasing from a Semiconductor Nanocrystal/Microsphere Resonator Composite**. *Adv Mater* 2005, **17**(9):1131-1136.

19. Leatherdale CA, Woo WK, Mikulec FV, Bawendi MG: **On the Absorption Cross Section of CdSe Nanocrystal Quantum Dots**. *J Phys Chem B* 2002, **106**(31):7619-7622.

Chapter 3. Development of Quantum Dot Antibody Conjugates for *in vivo* Imaging of Single Endogenous Cells

3.1 Background and Motivation

Imaging single endogenous cells in a live animal for an extended period of time can provide much information about cellular interactions and the microenvironment of the cells in a living organism. However, the requirements for fluorescent probes used in single molecule imaging *in vivo* are very restrictive due to the complexity of *in vivo* environments. Quantum dots (QDs) are ideal candidates, possessing unique optical properties: a tunable bandgap ranging from the visible to infrared, high quantum yield (QY), narrow and symmetric emission features, broad absorption features below the band edge, large two-photon absorption cross sections, and high photo-stability [1-4]. The tunability of emission wavelength enables the use of the near infrared (NIR) window for *in vivo* imaging where there is low absorption and minimal scattering by tissues and blood [5, 6]. Utilizing the NIR window has been difficult with organic dyes because they tend to have low QY and low thermal- and photo- stability in the NIR [7-11]. Furthermore, the narrow and symmetric emission features of QDs enable distinction of multiple bio-markers and the broad absorption features allow simultaneous excitation of QDs with a single light source [12-14]. Lastly, QDs generally have a two-photon absorption cross section that is two to five orders of magnitude larger than organic dyes, making QDs favorable for two photon imaging [7, 15-17].

Antibody (Ab) is a Y-shaped protein used by the immune system to recognize and bind to foreign objects (antigens). Antibody can be raised to recognize any antigenic target of interest (proteins, peptide, carbohydrate, or other small molecules), and therefore, is widely used for targeting experiments. QD-Ab conjugates have been used to target cells or receptors of interest both in vitro and in vivo [18-21]. However, most *in vivo* imaging studies using QD-Ab conjugates have involved ensemble measurements of QD signals over large volumes such as solid tumors.[21-24] This macro-environment context is due to a lack of technology for synthesizing QD conjugates optimal for single cell microenvironment imaging. Previous reports on single molecule tracking in live mice using commercial QD antibody conjugation kits have shown the great potential of QDs as probes for *in vivo* imaging [25, 26]; however, the dearth of publications in this field indicates the difficulty of obtaining reproducible *in vivo* data with high signal to noise ratios using the existing techniques.

This chapter describes the development of quantum dot-antibody (QD-NB-Ab) conjugates suitable for *in vivo* imaging by combining recent advances in QD synthesis, ligand development and conjugation chemistry. The first enabling piece of our synthetic technology lies in advanced QD synthesis. Recently developed core-shell QD syntheses produce QDs that are small, bright, stable, and display narrow emission bands [6, 27, 28]. These properties of the QDs make them optimal for multi-color imaging in highly scattering and biologically crowded environments. The second enabling piece is the water solubilization technique employing newly developed poly(imidazole) ligands (PILs) [27]. PILs are random co-polymers that incorporate imidazole for QD binding, methoxy poly(ethylene glycol) (PEG) for water solubility and bio-compatibility, and amino PEG for further derivitization. QDs that are ligand exchanged with the PILs have small hydrodynamic diameters because PILs are directly coordinated to the QD

surface. This is in stark contrast to the generally used encapsulated QDs that have an extra hydrophobic ligand layer between amphiphilic polymers and the QD surface. The small size of the PIL QDs enhances their diffusion in a biologically crowded environment [23]. In addition, the multidentate imidazole motifs of PILs are chemically stable and exhibit a high affinity towards the Cd and Zn-rich QD surfaces. Therefore, PILs passivate the QD surface effectively to achieve high QY (80-90% [29]) in aqueous solution, greatly enhanced stability in buffers and serum, and extremely low non-specific binding to serum and cells [27]. The third enabling piece of our technology lies in the employment of the norbornene-tetrazine cycloaddition for the conjugation of bio-molecules on QDs. Unlike functional groups involved in traditional conjugations such as carboxyl groups, amine groups and thiols, tetrazine and norbornene show minimal interactions with the QD surface and are therefore more accessible for the PIL QD conjugation step. As shown previously, this catalysis-free click chemistry on QDs yield efficient coupling of organic molecules and proteins to the QDs [30]. In this chapter, we utilized a modified version of thisthis conjugation method to synthesize compact QD-NB-Ab conjugates.

3.2 Synthesis of QD-NB-Ab Conjugates

To prepare the QD-NB-Ab conjugates, norbornene-modified poly imidazole ligands (NB-PIL) coated QDs (QD-NB) were conjugated with tetrazine modified antibodies as shown in Figure 3-1. The NB-PILs were prepared by modifying primary amines of poly(amino-$PEG_{11})_{20\%}$–PIL (NH_2–PIL) with an amine-reactive norbornene species. We then exchanged the native QD ligands with NB-PILs as described previously [30]. Tetrazine-modified antibodies were prepared by reacting amine-reactive tetrazine with the lysine groups of antibodies. These

were immediately conjugated to the NB-PIL coated QDs simply by mixing the two components at room temperature for 22-24 hours; this step needs to be performed rapidly since tetrazine degrades over time in aqueous solution [31]. After conjugation, unreacted tetrazine on the antibodies were quenched to prevent aggregation. This conjugation scheme can be extended to any QDs containing Cd or Zn on the surface and any antibodies containing lysine residues. In this study, diverse combinations of QDs (CdSe/CdZnS, CdSe/CdS and InAs/CdZnS) and antibodies (CD31, CD45, C-kit, Sca-1, and IgG) were synthesized and used for imaging experiments. All synthesized QDs used in this study are represented as $QD_{\text{emission wavelength (nm)}}$.

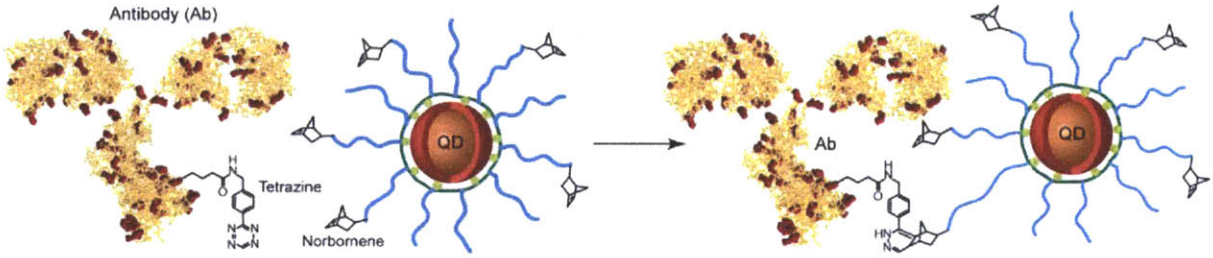

Figure 3-1 Conjugation of QDs to antibodies (Ab). Ab is represented by IgG_{2a} and Lys residues of IgG are marked by red balls.

3.3 Characterization

3.3.1 Nonspecific Serum Binding Studies for *in vivo* Experiments

Prior to using any QD-NB-Ab constructs for specific targeting *in vivo*, we first validated the bio-compatibility of the NB-PIL coated QDs (QD_{612}-NB) by incubating the QDs with fetal bovine serum (FBS) at 37°C for 4 to 6 hours. The size of the QD samples before and after incubation was measured using fluorescent correlation spectroscopy (FCS, Figure 3-2) and dynamic light scattering (DLS). The measurements show that the size of the particles does not

change after the serum incubation, in contrast to commercial Qdot® 625 that are encapsulated with amphiphilic polymers (Invitrogen) which showed a significant size increase after serum incubation (Table 3-1). Furthermore, the standard deviation of the QD_{612}-NB size remained the same after incubation, indicating that they do not exhibit non-specific adsorption of serum proteins (Table 3-1).

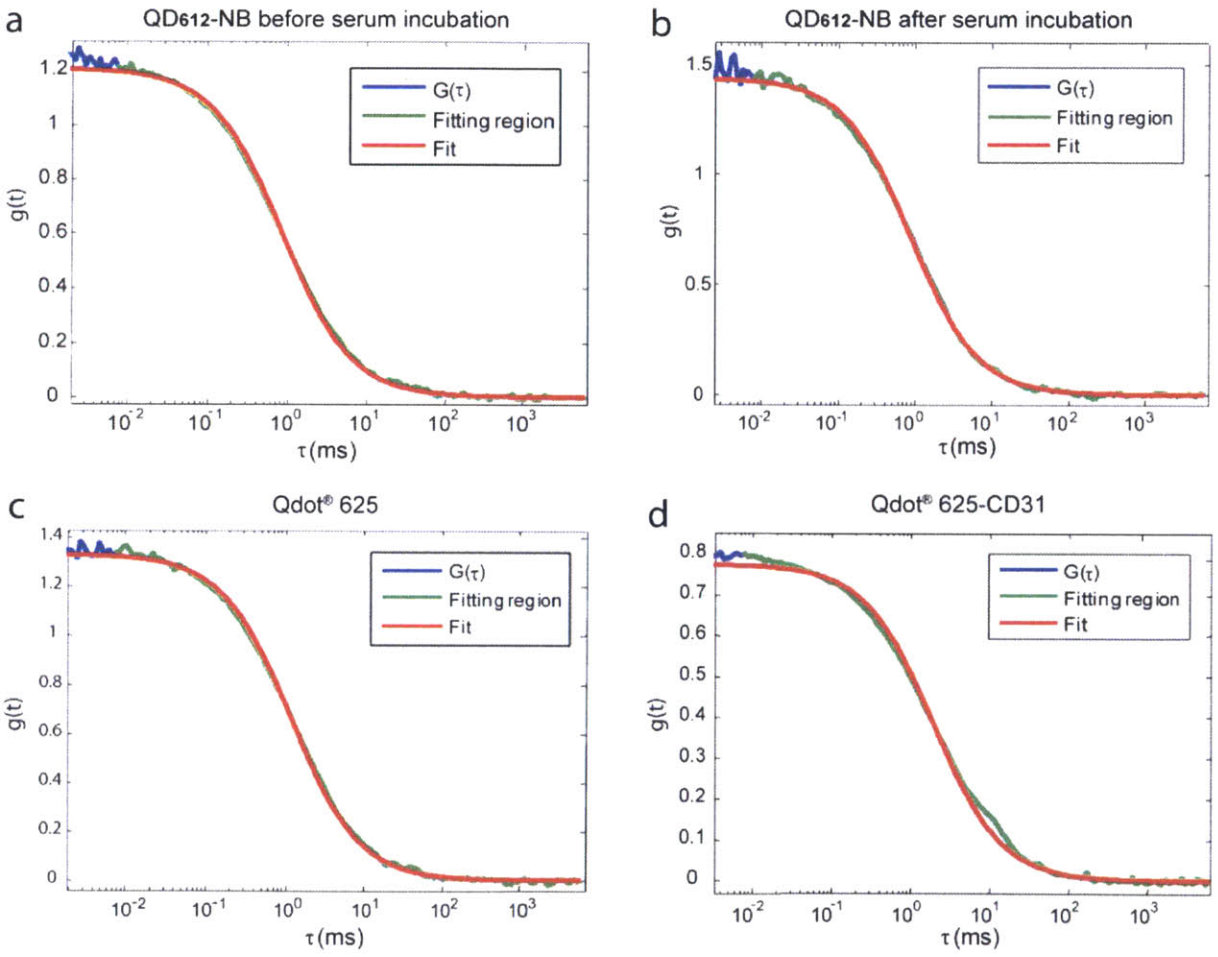

Figure 3-2 Representative curves for Fluorescence Correlation Spectra measurements. The solid blue lines are correlation factors $G(\tau)$, the solid green lines are fitting regions, and the solid red lines are fits of each measurements (a) NB-PIL coated QD_{612} before serum incubation, (b)NB-PIL coated QD_{612} after serum incubation, (c) Qdot® 625 before serum incubation, and (d) Qdot® 625 after serum incubation.

Table 3-1 Hydrodynamic Diameter of the QD samples measured using DLS and FCS.

	Inorganic Diameter (nm)	Average Hydrodynamic Diameter (nm)
QD_{612}-NB	5.8 ± 0.5	12.5 ± 0.2
QD_{612}-NB + FBS at 37°C for 4 hours (measured using FCS)		12.6 ± 0.2
QD_{612} : CD31 = 1 : 1		14.5 ± 0.4
QD_{612} : CD31 = 3 : 1		15.3 ± 0.8
Qdot® 625 (Invitrogen)	9.0 ± 1.0	20.0 ± 0.5
Qdot® 625 + FBS at 37°C for 4 hours (measured using FCS)		33.4 ± 2.6
Qdot® 625 -CD31		20.5 ± 0.6

3.3.2 Stability

In addition to the bio-compatibility, we observed that the PIL coated QD_{612} is more stable in solution versus Qdot® 625. A simple test for stability is to centrifuge an aqueous solution of QDs. If the QDs are aggregated or unstable, they will form precipiates at the bottom. Qdot 625 rapidly started forming preciptates after centrifugation for 5600 rcf for 3 minutes, while the QD_{612}-NB QDs remained dispersed and homongenous in solution. This can be explained by strong interactions between the multidentate imidazole moieties of the PILs and the Cd/Zn atoms on the QD surface in QD_{612}-NB, in contrast to the weak hydrophobic interaction between amphiphilic polymers and the native hydrophobic ligands of QDs in Qdot® 625. Strong binding of ligands to the QD surface is an important factor for maintaining high QY *in vivo* because surface defects caused by ligand detachment can promote fluorescent quenching [32-34].

3.3.3 Size

Another crucial factor for *in vivo* labeling using QDs is the hydrodynamic size of a QD-NB-Ab construct. This hydrodynamic size will influence the bioavailability and clearance properties of the particle in a live animal [22, 35]. The size of the QDs and the QD conjugates was measured by DLS (Figure 3-3(b) and Table 3-1). As expected, both QD_{612}-NB and QD_{612}-NB-Ab were more compact than Qdot® 625 and Qdot® 625-Ab. The compact size of the QD-NB-Ab conjugates enhances access to biologically crowded regions and increases their diffusion rate throughout densely packed *in vivo* environments.

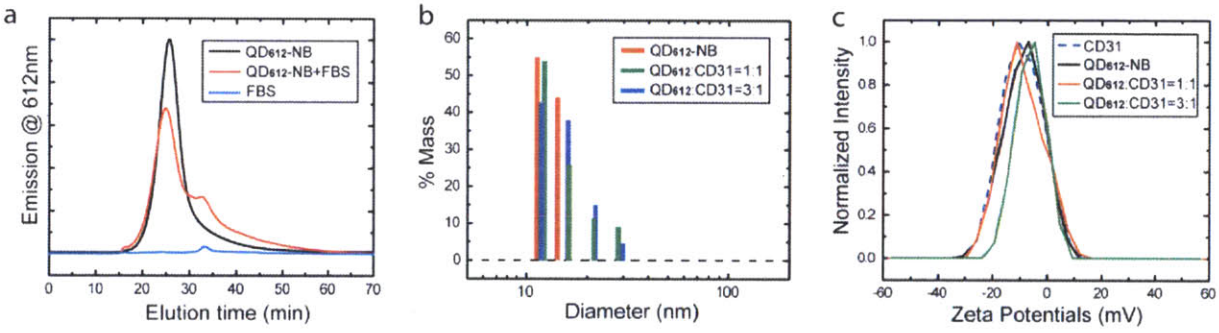

Figure 3-3 (a) DLS Data of the QDs and the QD-Ab conjugates. (b) Zeta potential measurement of the QDs and the QD-Ab conjugates. (c) GFC traces of the NB-PIL coated QD_{612} before and after the serum incubation.

3.3.4 Zeta potential

The charge of QDs also has a major effect on the transport behavior of nanoparticles *in vivo* and *in vitro* [36]; high surface charge of nanoparticles, either positive or negative, tends to cause non-specific uptake by macrophages which in turn cause more accumulation of the particles in the liver rather than the targeted region after systemic administration. Zeta potential measurements indicated that the surface charge of the QD-NB and the QD conjugates were

relatively neutral (Figure 3-3(c) and Table 3-2). With the low nonspecific binding, small hydrodynamic size, and neutral surface charge, the QD-PILs and the QD-NB-Ab conjugates developed here appear optimal for *in vivo* labeling.

Table 3-2 Zeta potential measurement of the QDs and the QD-Ab conjugates.

	Zeta Potential (mV)
QD_{612}-NB	-7.9 ± 1.2
QD_{612} : CD31 = 3 : 1	-6.3 ± 1.2
QD_{612} : CD31 = 1 : 1	-9.0 ± 2.1
Qdot® 625 (Invitrogen)	-18.5 ± 3.5
Qdot® 625 -CD31	-7.7 ± 1.6

3.4 Flow Cytometry Experiments

After the characterization of the QD complex, we tested the specificity of the QD-NB-Ab conjugates *in vitro* using flow cytometry (Figure 3-4). Blood cells (excluding red blood cells) were purified and used for labeling. First, non-specific binding of the QD-NB and the QD-NB-Ab conjugates to cells was tested by incubating blood cells with QD_{570}-NB, QD_{612}-NB, and QD_{570}-NB-IgG. As shown in Figure 3-4(a-c), no non-specific labeling was observed. Then, QD_{612}-NB-CD45 was incubated with the blood cells to label leukocytes. After incubation, >50% of the blood cells showed high intensity of the QD_{612} emission; this number corresponds approximately to the percentage of leukocytes out of all blood cells in the sample (Figure 3-4(d)). Next, the blood cells were co-incubated with PE-Cy7 labeled CD45 (CD45-PE-Cy7) and QD_{570}-NB-IgG to verify that QD_{570}-NB-IgG does not interfere with the interaction between leukocytes and CD45-PE-Cy7. As expected, leukocytes were labeled only with CD45-PE-Cy7. A small population of the cells shows up in the QD_{570} channel because a small portion of the emission from PE-Cy7 leaks into the QD_{570} channel (Figure 3-4(e)). Finally, the blood cells were

incubated with QD_{612}-NB-CD45 and CD45-PE-Cy7. A good correlation between the signal from CD45-PE-Cy7 and QD_{612}-NB-CD45 was observed, which indicates that the QD_{612} conjugated antibodies label leukocytes specifically (Figure 3-4(f)).

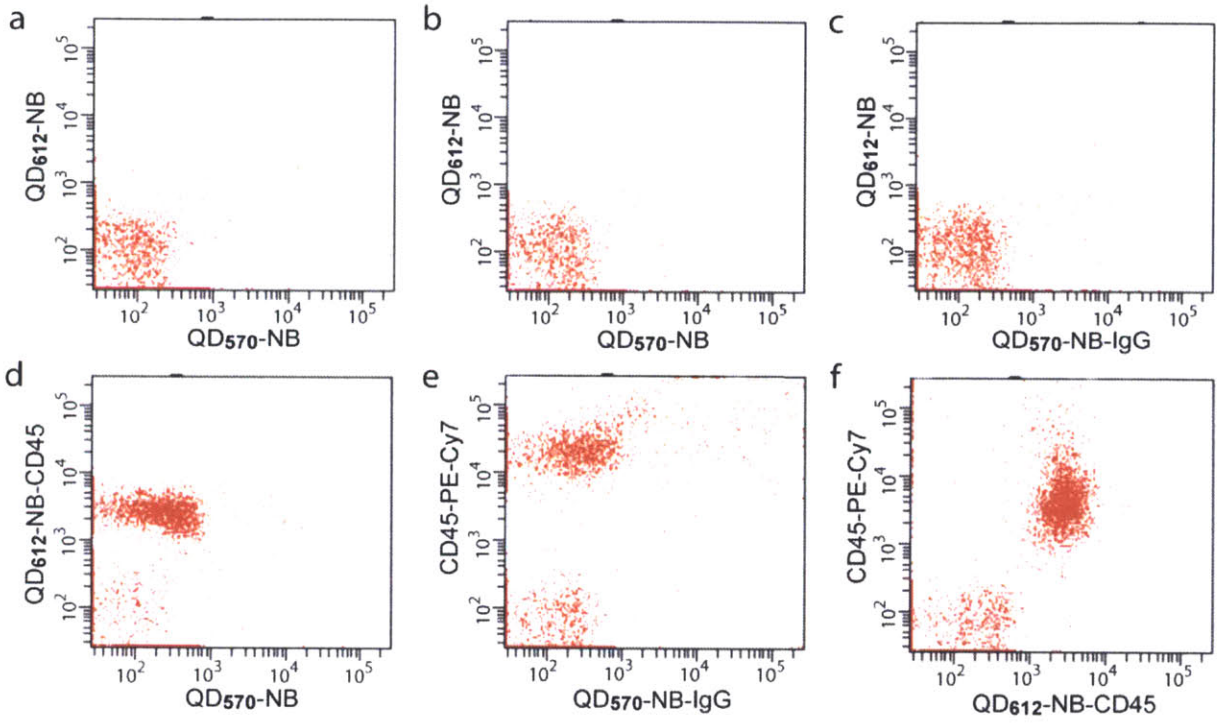

Figure 3-4 Flow cytometry data on the QDs and the QD conjugates incubated with blood cells (excluding red blood cells). (a-c) Non-speficic binding test for NB PIL coated QD_{612} (QD_{612}-NB), QD_{570}-NB and QD_{570}-NB-IgG (d) Specific binding of QD_{612}-NB-CD45 to leukocytes. (e) Specific binding of CD45-PE-Cy7 to leukocytes. QD_{570}-NB-IgG was co-incubated to prove that QD_{570}-NB-IgG does not interfere with the labeling of the dye labeled antibodies. (There is some leakage of PE-Cy7 emission into QD_{570} channel) (f) co-incubation of QD_{612}-NB-CD45 and the CD45-PE-Cy7 with blood cells. A good correlation between the signal from CD45-PE-Cy7 and QD_{612}-NB-CD45 indicates that the QD_{612}-NB-CD45 specifically label leukocytes in the same manner as the dye labeled antibodies(CD45-PE-Cy7).

3.5 *In vivo* Labeling Experiments

3.5.1 Preparation of the QD-Ab Samples for Vessel Labeling

Following the *in vitro* labeling experiments, which showed a high degree of specific binding with very low background, we labeled vessels (meso-scale objects) in live mice with QD_{612}-NB-CD31 antibody conjugates (QD_{612}-NB-CD31) and optimized the ratio between QDs and antibodies to yield the best in-vivo imaging results in terms of the brightness and the stability of the signal. The immuno-conjugates containing higher number of QDs will provide brighter signals, but the large size of QDs can initiate undesired bio-pathways *in vivo* or cause detachment of QD-Ab conjugates from labeling objects. For this study, samples with three different ratios of QD and Ab were synthesized by incubating 3:1, 1:1, and 1:3 ratio of QD-NB to tetrazine modified antibodies. After the synthesis, the QD-Ab conjugates were purified using gradient centrifugation (Figure 3-5) and the ratio between QD and Ab were measured using BCA assay (Figure 3-6 and Table 3-3).

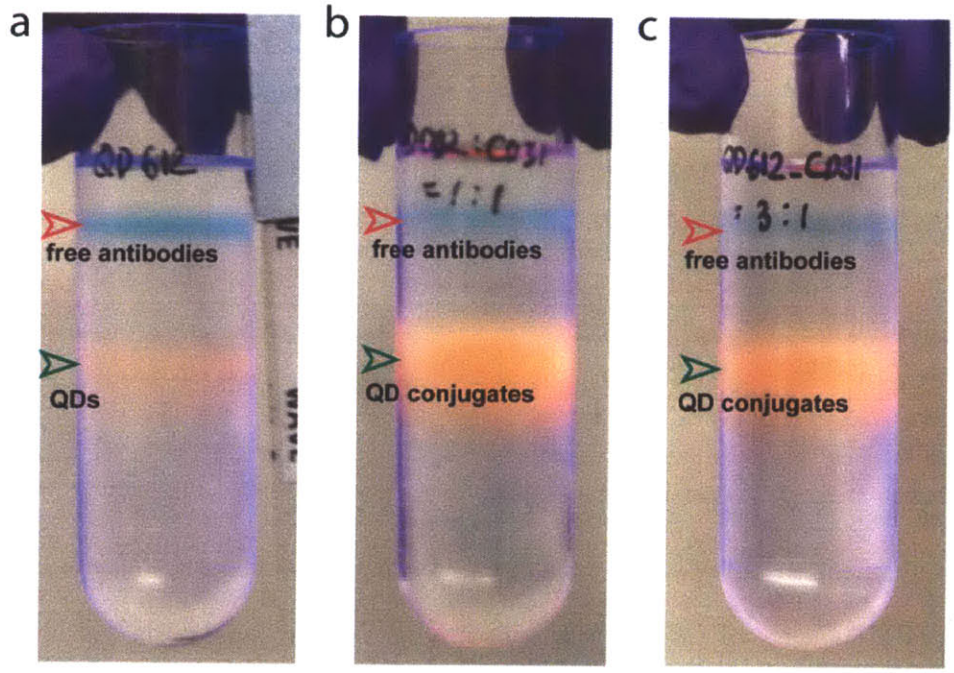

Figure 3-5 Gradient centrifugation to remove free antibodies from the QD_{612}-CD31 conjugates.

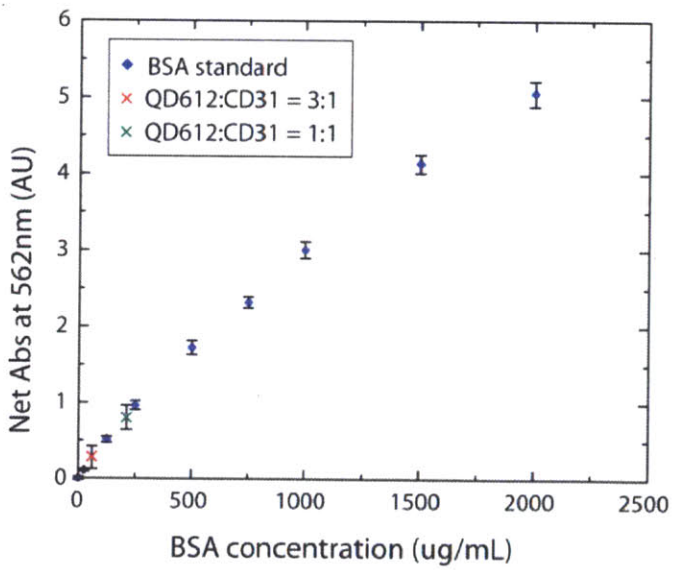

Figure 3-6 Calibration curve for protein concentration measurement using BSA standard solution.

Table 3-3 Calculation of the actual ratio between QDs and antibodies after purification.

	QD_{612}:CD31=3:1	QD_{612}:CD31=1:1
QD_{612} concentration	0.15 μM	0.21 μM
CD31 concentration in mass	63 μg/mL	204 μg/mL
MW of CD31	150 kDa	150 kDa
Molar concentration of CD31	4.2×10^{-7} M	1.6×10^{-6} M
Dilution factor for CD31	10	10
Ratio between QD_{612} and CD31	3.6 : 1	1.3 : 1

In addition, the gel filtration chromatograpy (GFC) traces and the transmission electron microscopy (TEM) images of the resulting QD_{612}-NB-CD31 conjugates showed no aggregate formation confirming the mono-dispersity of the samples (Figure 3-7 and 3-8).

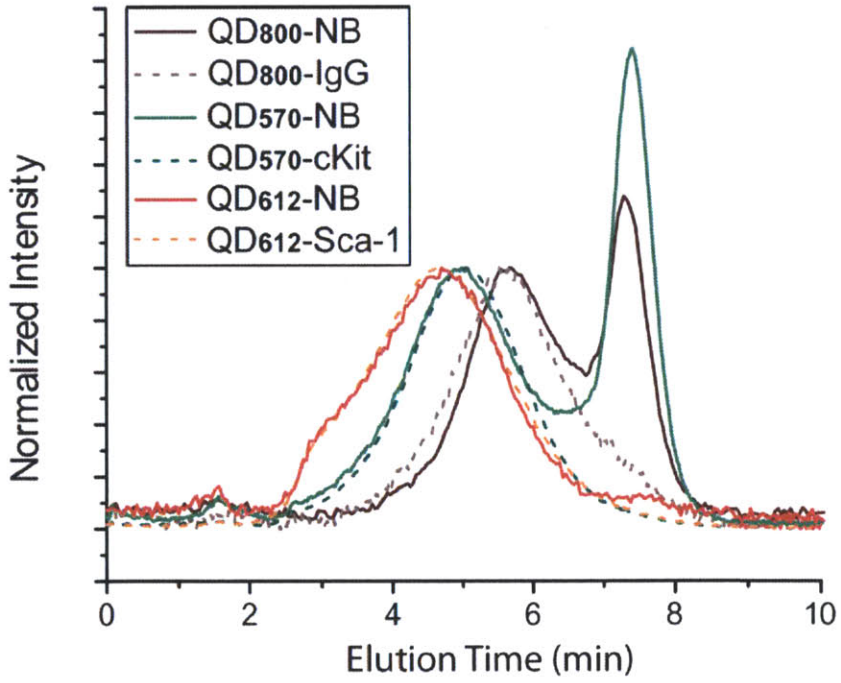

Figure 3-7 GFC traces of NB-PIL coated QD_{570} (solid green line), QD_{612} (solid red line), QD_{800} (solid brown line) and QD-Ab conjugates: QD_{800}-IgG (dashed brown line), QD_{612}-Sca-1 (dashed red line), QD_{570}-C-kit (dashed green line).

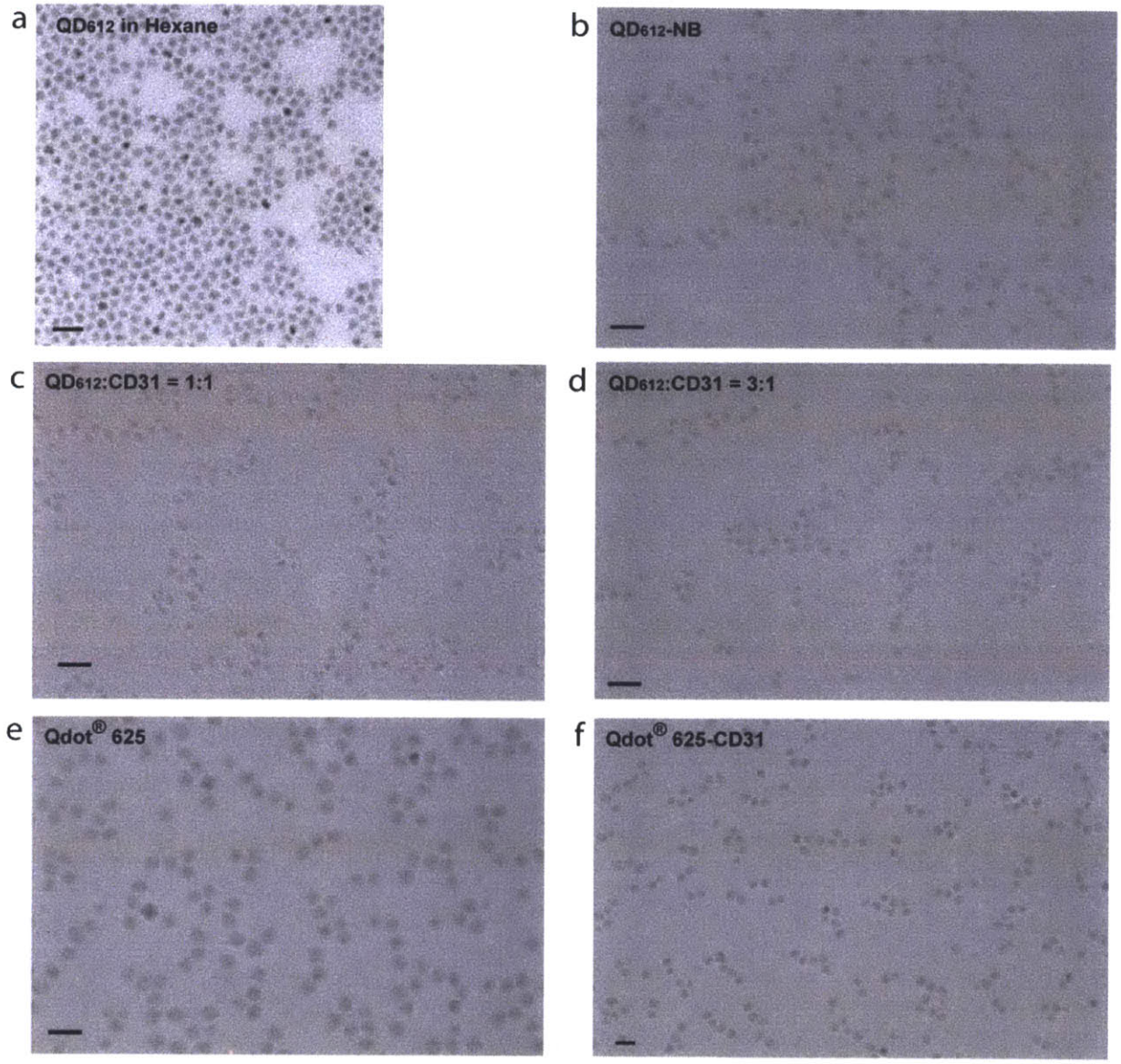

Figure 3-8 TEM images of NB-PIL coated QD_{612}, QD_{612}-CD31, Qdot® 625, and Qdot® 625-CD31 (a) QD_{612} in Hexane, (b) NB-PIL coated QD_{612}, (c) QD_{612}-CD31 conjugates (QD:CD31=1:1), (d) QD_{612}-CD31 conjugates (QD:CD31=1:1), (e) Qdot® 625, and (f) Qdot® 625-CD31 conjugates. Scale bar = 20nm.

3.5.2 Vessel Labeling

After the synthesis and the characterization, the QDs or QD conjugates were administered systemically via retroorbital injection to Tie2GFP/FVB mice and the vessels were imaged through a mammary fat pad window using a two photon intravital microscope. Endothelial cells of the Tie2GFP/FVB mice express green fluorescent proteins (GFP) to visualize vessels; therefore, the specificity of the QD_{612}-NB-CD31 to endothelial cells can be confirmed by co-localization of the QD signal to the GFP signal. Before the labeling, non-specific binding of the QDs and the QD-Ab conjugates was tested *in vivo* by injecting free QD_{612}-NB and QD_{612}-NB-IgG, and imaging the vessels over time. Both QD_{612}-NB and QD_{612}-NB-IgG completely cleared from the vessels within ~16 hours without leaving any evidence of non-specific accumulation (Figure 3-9(a-b) and Figure 3-10). In contrast, we observed non-specific accumulation of the commerical Qdot® 625 and Qdot® 625-IgG in random spots after the QDs were cleared from the vessels (Figure 3-9(c-d) and Figure 3-11).

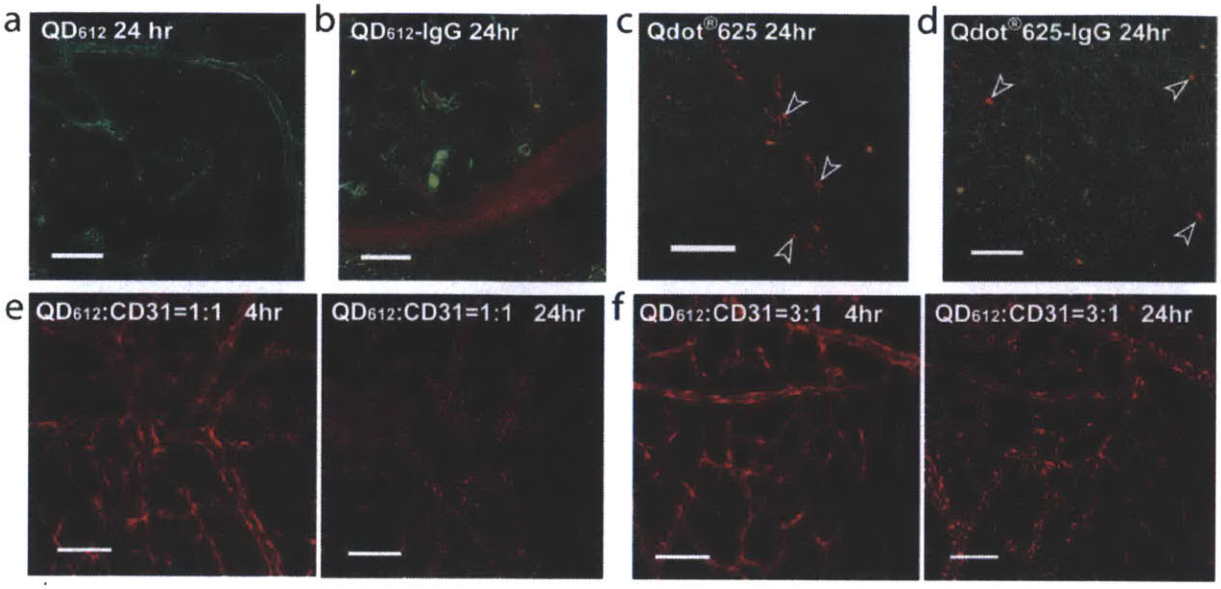

Figure 3-9 *In vivo* imaging (a-d) Non-specific binding studies for a) QD_{612}, b) QD_{612}-IgG, c) Qdot® 625 and d) Qdot® 625-IgG. (e-h) Labeling of endothelial cells using the QD_{612}-CD31 conjugates. e) 4 hours and 24 hours after the injection of QD_{612}-CD31 conjugates with the ratio of 1:1 for QDs and CD31, f) 4 hours and 24 hours after the injection of QD_{612}-CD31 conjugates with the ratio of 3:1 for QDs and CD31.

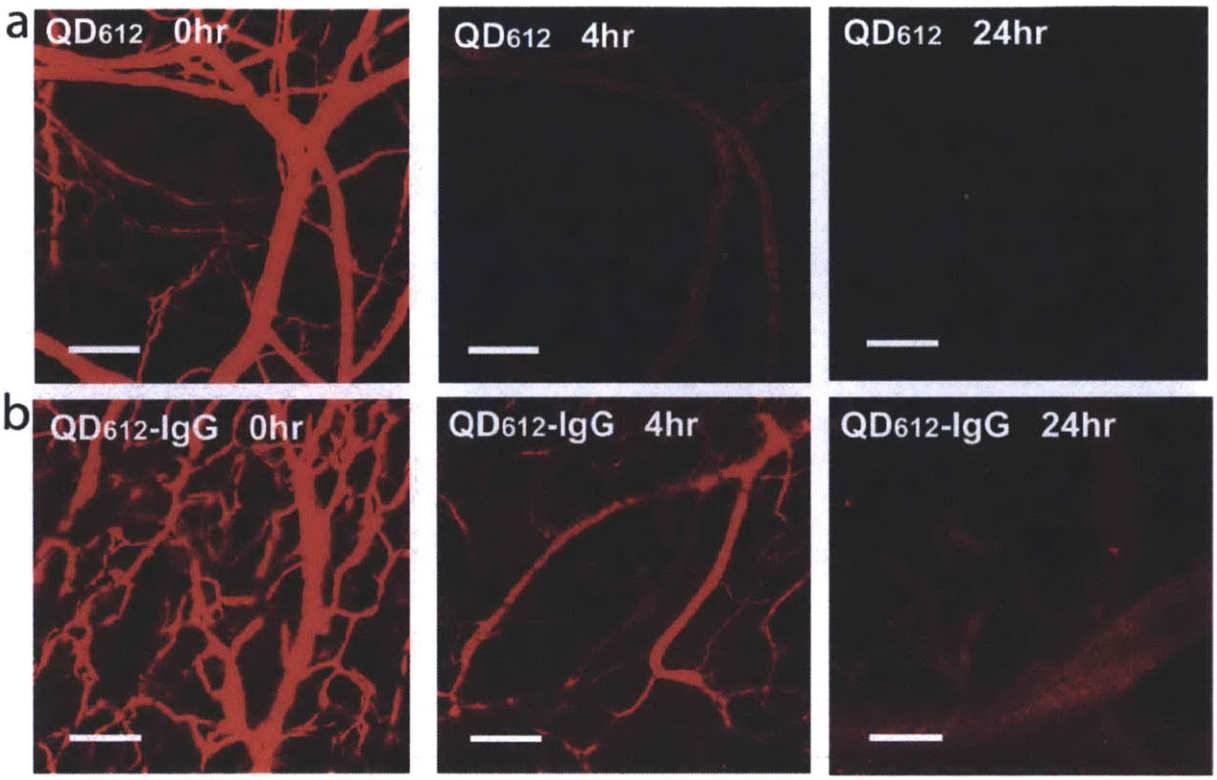

Figure 3-10 Time series *in vivo* imaging of (a) the QD_{612} and (b) the QD_{612}-Ab conjugates (QD_{612}-IgG conjugates and the QD_{612}-CD31 conjugates) at 0, 4 and 24 hours after the injection.

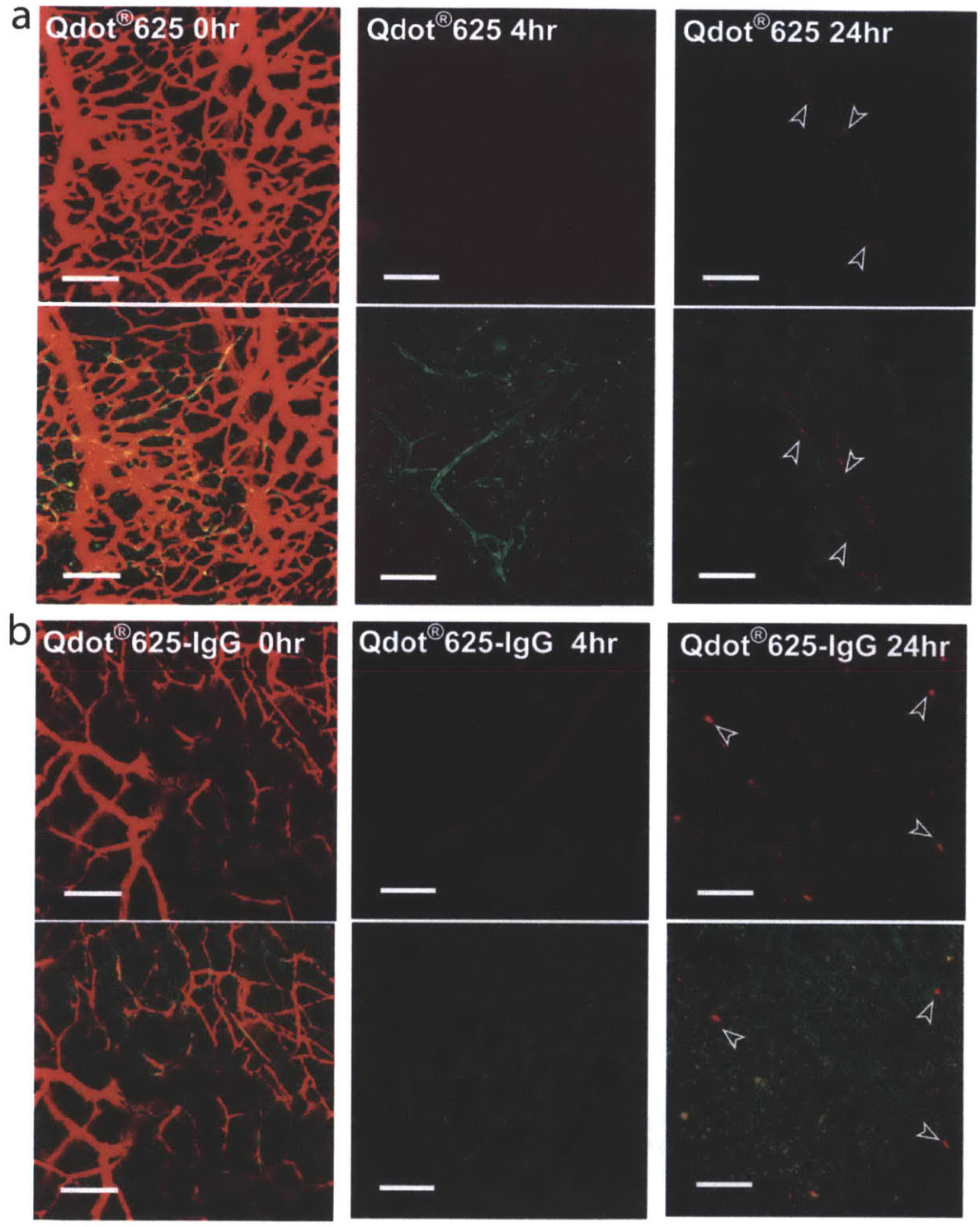

Figure 3-11 Time series imaging of vessels in live mice after injecting a) the Qdot® 625 and b) the Qdot® 625-IgG conjugates. Upper 3 panels are for the Qdot® 625 channel only and the lower 3 panels are for both Qdot® 625 and GFP channels.

Next, the QD_{612}-NB-CD31 conjugates were injected and their labeling of the vessels was monitored. As shown in Figure 3-9(e-h) and Figure 3-12, we observed the co-localization of the QD_{612}-NB-CD31 signal to the GFP signal of the vessels at 3~4 hours and later time points. After 24 hours the QD signal from the vessels was still visible, but the observed pattern was more punctate (Figure 3-9(f-h) and Figure 3-12). Punctate patterns indicate endocytosis of the QD_{612}-NB-CD31 into endothelial cells due to the relatively large size of the QDs (HD of ~13nm) attached to the antibodies (HD of ~12nm). In contrast, allophycocyanin (APC) labeled CD31 (CD31-APC) showed a more diffusive labeling pattern along the vessels up to 24 hours after the injection (Figure 3-13). Next, the level of labeling by the QD_{612}-NB-CD31 conjugates was evaluated at 4 hours and 24 hours after the injection. In both case, the labeling signal was the highest for the QD:Ab=3:1 sample, and the lowest for the QD:Ab=1:3 sample (Figure 3-9(e-h) and Figure 3-12).

Next, commercial Qdot® 625 was conjugated with CD31 antibodies using the commercial antibody conjugation kit (Invitrogen). As shown in Figure 3-14, the vessel walls were well labeled with the Qdot®-Ab conjugates at 4 hours after the injection but the staining pattern was more punctate than the pattern obtained with our conjugates. At 24 hours after the injection, only low intensity of the Qdot® signal was observed and the labeling pattern was much more random (Figure 3-14). Because of the high nonspecific binding nature of the Qdot® *in vivo*, we were not able to distinguish the signal of the Qdot® labeling the vessels from the signal of the Qdot® nonspecifically accumulated on random bio-compartments at the 24 hour time points.

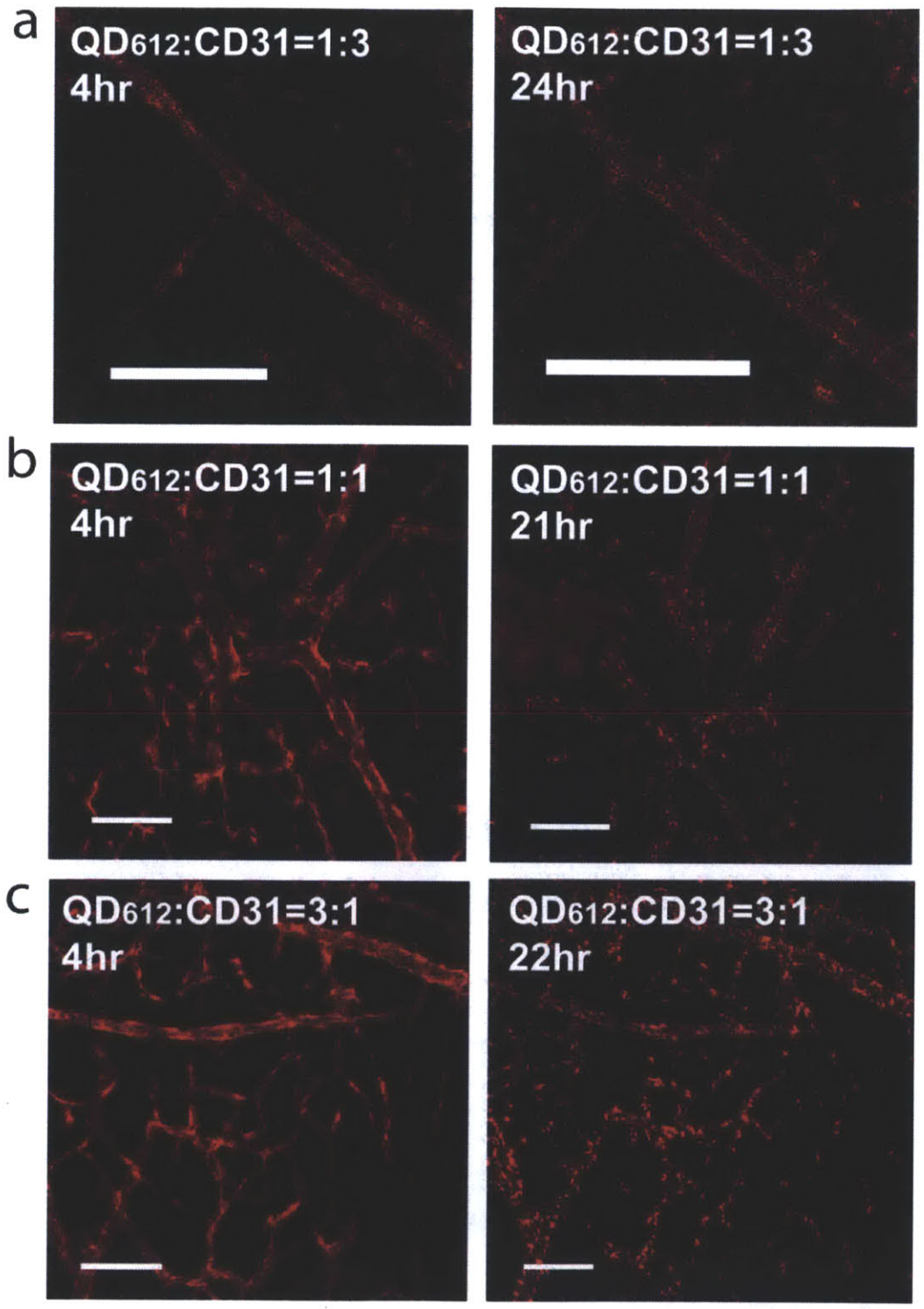

Figure 3-12 Time series *in vivo* imaging of the QD_{612}-Ab conjugates with different ratios of QD to Ab.

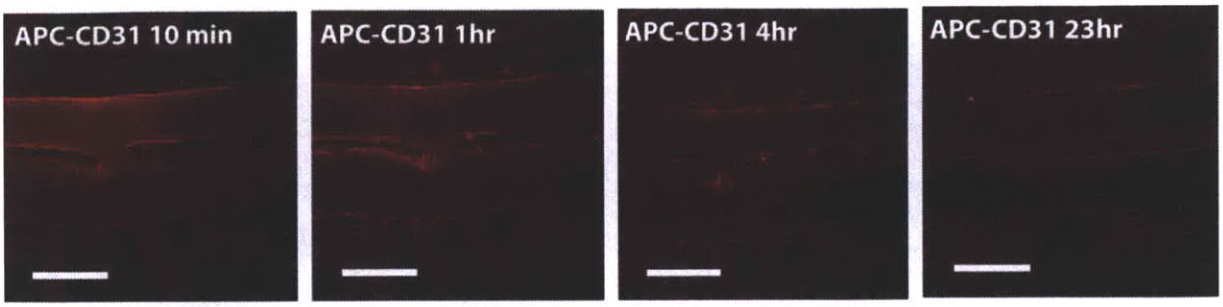

Figure 3-13 Time series imaging of vessels of live mice after injecting APC-CD31.

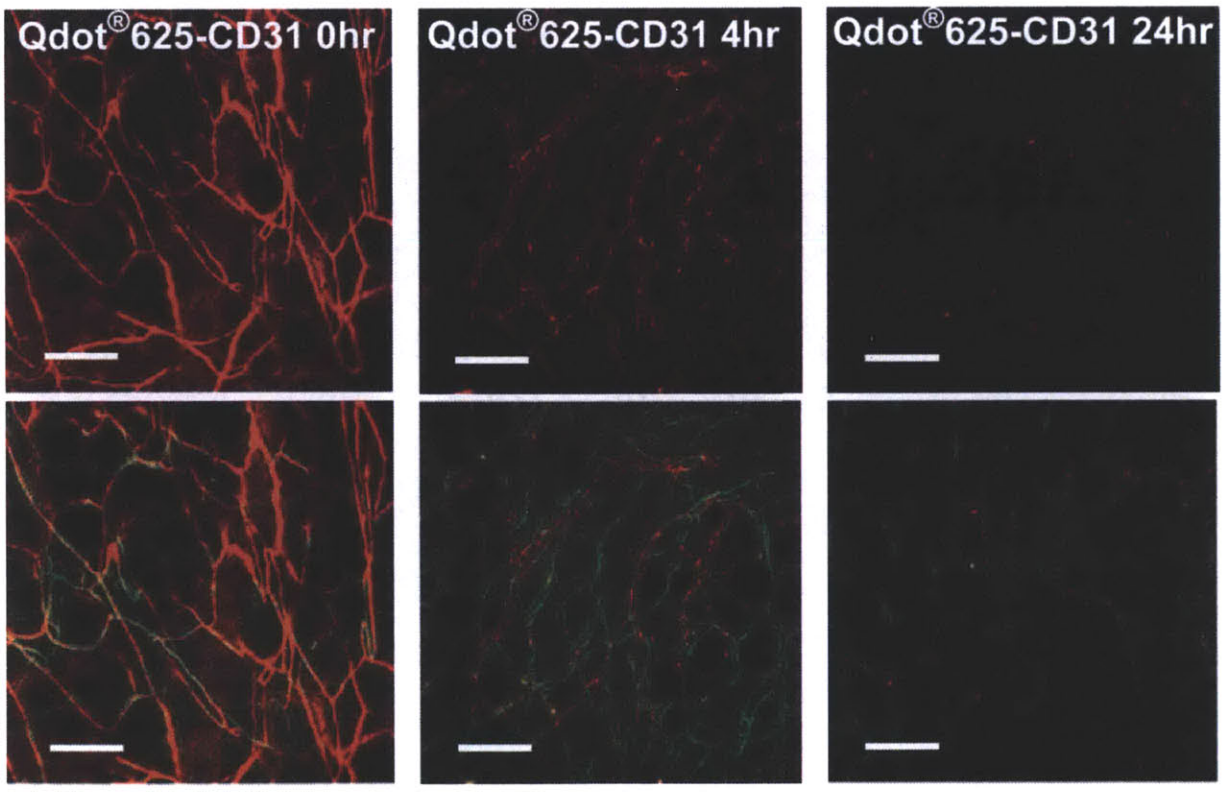

Figure 3-14 Time series imaging of vessels in live mice after injecting the Qdot® 625-CD31 conjugates. Upper panel at each time point is for Qdot® 625 channel only and lower panel at each time point is for both Qdot® 625 and GFP channels.

3.5.3 Single Hematopoietic Stem Cell Labeling

Finally, single endogenous hematopoietic stem cells (HSCs) were labeled with the QD-NB-Ab conjugates and Hoechst 33342, and imaged through a chronic bone marrow window. HSCs were identified by being QD_{570}-NB-cKit positive, QD_{612}-NB-Sca-1 positive, and Hoechst 33342 negative. QD_{800}-NB-IgG conjugates were also co-injected to check the non-specific binding of the QD-NB-Ab conjugates *in vivo*. Bones were imaged by second harmonic generation of collagen; imaging was performed 22-23 hours after the injection of QD-NB-Ab conjugates. By the time of imaging, unbound QD-NB-Ab conjugates were completely depleted from the vessels and the bone marrow, and cells in the bone marrow labeled with the QD-NB-Ab conjugates and Hoechst dyes were visualized (Figure 3-15). The movement of the HSCs and other cells in the bone marrow was also recorded over 3 hours. More detailed studies on endogenous HSCs and their microenvironment will be reported elsewhere. Lastly, in order to prove that the color or the composition of the QDs do not affect the quality of the imaging, we labeled HSCs using QD-NB-Ab conjugates with different combinations of QDs and antibodies; QD_{800}-NB-cKit, QD_{612}-NB-Sca-1 and Hoechst33342. In this case, the vessels were visualized with GFP. Figure 3-16 shows the successful labeling of HSCs which confirms that we can utilize the variety of QDs that emit in the visible to NIR to prepare the QD-NB-Ab conjugates for multiplexed imaging.

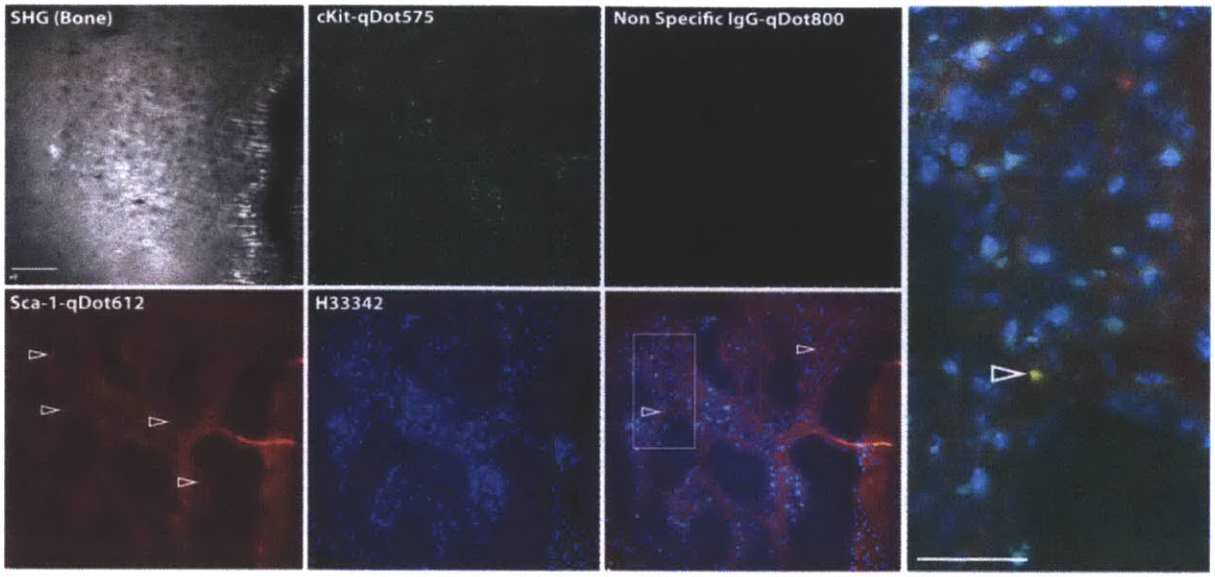

Figure 3-15 Hematopoietic stem cell labeling with QD_{612}-Sca-1, QD_{570}-cKit, QD_{800}-IgG, and Hoechst33342 in bone marrow.

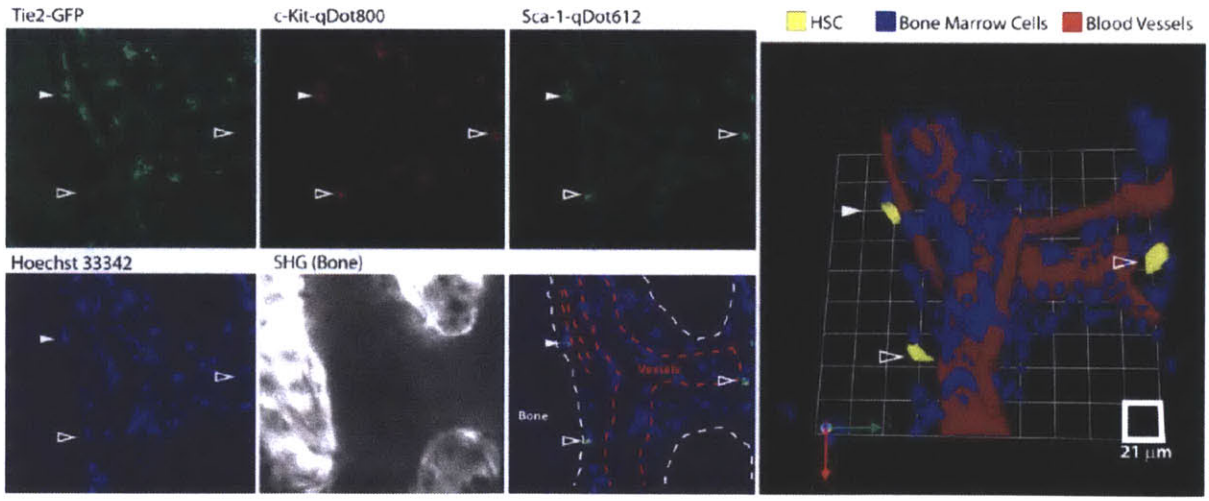

Figure 3-16 Hematopoietic stem cell (HSC) labeling using QD_{800}-c-Kit, QD_{612}-Sca-1, and Hoechst 33342 in Tie2GFP/FVB mice.

3.6 Conclusion

In summary, compact, bright and stable QD-NB-Ab constructs have been synthesized by taking advantage of recent advances in QD synthesis, ligand development, and conjugation chemistry on QDs. The high QY and narrow emission feature of the QDs enable simultaneous imaging of multiple biomarkers, the PIL ligands result in compact size, aqueous stability, and biocompatiblity, and norbornene-tetrazine click chemistry allow a facile and efficient coupling antibodies to QDs. Improved transport of the particles owing to the compact size of the QD-NB-Ab conjugates and extremely low non-specific binding compared to commercially available QD-Ab conjugates make the QD-NB-Ab a significant step forward for *in vivo* imaging. *In vitro* flow cytometry data indicate that the QD-NB-Ab conjugates specifically label cells in the same manner as the dye-labeled antibodies, demonstrating a high level of targeting specificity. *In vivo* imaging results prove that we can label both mesoscale objects (vessels) and single endogenous cells in live mice with QD-NB-Ab constructs both in the visible and in the NIR. Especially for the HSC imaging, five different color channels from the visible to NIR were utilized to label multiple bio-markers simultaneously. Multiplexing is especially beneficial for *in vivo* imaging where diverse cells are present in confined spaces. The technique described here can expand the scope of *in vivo* imaging by allowing single endogenous cell imaging in live animals using QDs of different wavelengths. Further experiments using various QD-NB-Ab conjugates are in progress to learn more about cellular interactions *in vivo* in a multiplexed regime. In the next chapter, we will describe additional HSC labeling experiments that led to new biological information about the micro-enviroments of the HSCs in live mice.

3.7 Experimental Section

3.7.1 Synthesis

Synthesis of QDs. QDs used in this study were synthesized with modifications of previously reported syntheses as described below.

Synthesis of CdSe(CdS) QDs-QD$_{570}$. CdSe cores with a first absorption peak at 480nm were synthesized using a previously reported method.[3] The cores were precipitated with acetone three times to remove excess ligands and salts, and left overnight at 4°C before overcoating. CdS shells were deposited on CdSe cores via modification of previously reported procedures. (ref) Before the shell deposition, the cores (274 nmol) were filtered with a 0.2 μM PTFE syringe filter and annealed at 220 °C in a solvent mixture of oleylamine (3 mL) and octadecene (6 mL) until no spectral shift was observed. Cd and S precursor solutions were then introduced simultaneously at 240°C over 2 hours. The Cd precursor consisted of 0.3 mmol Cd(oleate)$_2$ and 0.6 mmol oleylamine in a solvent mixture of octadecene (1.5 mL) and TOP (3 mL). The S precursor consisted of 0.3 mmol hexamethyldisilathiane [(TMS)$_2$S] in 6 mL TOP. Addition of a total of 5 monolayers of CdS yielded QDs with an emission at 570 nm and a quantum yield close to unity when diluted in octane.

Synthesis of CdSe(Cd$_{0.3}$Zn$_{0.7}$S)-QD$_{612}$. The synthesis follows previously reported procedures [28, 37]. The QY of the QD$_{612}$ was 50% in octane.

Synthesis of InAs/Cd$_{0.2}$Zn$_{0.8}$S-QD$_{800}$. Synthesized as previously reported [6]. The quantum yield of the QD$_{800}$ was 20% in octane

Synthesis of NB-PIL coated QDs (QD-NB). Norbornene modified PIL was synthesized with modifications of the previous work [30]. (1S,2S,4S)-bicyclo[2.2.1]hept-5-en-2-yl acetic acid (norbornene) was activated by *N,N'*-Diisopropylcarbodiimide and hydroxybenzotriazole in anhydrous tetrahydrofuran(THF) at room temperature. The activated norbornene was reacted with poly(amino-PEG_{11})$_{20\%}$-PIL in dry THF. After the reaction was completed, THF was pulled off and the reaction mixture was redissolved in water and filtered with a 0.2 μm Tuffryn syringe filter. The polymer solution was dialyzed 4 times through a 5kDa molecular weight cut off (MWCO) spin concentrator and redissolved in chloroform for further ligand exchange.

Synthesis of tetrazine modified antibodies (tet-Ab) and QD-Ab conjugates. Amine reactive tetrazine (5-((4-(1,2,4,5-tetrazin-3-yl)benzyl)amino)-5-oxopentanoic acid), which was synthesized following the previous literature [30, 38], was activated with hydroxybenzotriazole and *N,N'*-Diisopropylcarbodiimide in anhydrous N,N-dimethylformamide (DMF) and reacted with antibodies in pH 7.5 PBS solution overnight at room temperature. 5% DMF was added to the antibody solutions to solubilize the tetrazine. After the reaction is completed, the tetrazine modified antibodies (tet-Abs) were dialyzed 4 times using a 50kDa MWCO spin concentrator. Right after the synthesis of tet-Ab, tet-Ab was mixed with QD-NB for 20-24 hour at room temperature. After the conjugation, unreacted tetrazine on the antibodies was quenched using 5-norbornene-2,2-dimethanol. Before the biological experiments, the QD-Ab conjugates were dialyzed 3 times with a 50kDa MWCO spin concentrator to remove excess 5-norbornene-2,2-dimethanol.

3.7.2 Characterization

Fluorescence Correlation Spectroscopy (FCS). Size change of the QD612 and Qdot® 625 after the serum incubation was measured by FCS using a setup described previously [23]. 1μM of QD612 and Qdot® 625 were incubated with 90% Fetal Bovine Serum for 4-6 hr at 37°C and the samples were diluted in PBS right before the measurement. The excitation power was 8 μW in front of the objective and ten to eleven measurements with acquisition times of 30 s were performed for each sample. Correlation functions were fit in Matlab (The Mathworks) with the isotropic 2D translational diffusion model to extract the average particle diffusion times. These diffusion times were converted to sizes through the Stokes-Einstein equation using the hydrodynamic radii of the particles in PBS measured by dynamic light scattering as the standard.

Gradient centrifugation. Gradient centrifugation was used to purify free antibodies from the QD-Ab conjugates. A four layer sucrose gradient (10%+30%+50%+70%) was used for separation. 0.1mL of QD612-NB or QD612-NB-CD31 samples were added on top of the multilayer density gradient prior to ultracentrifugation. 0.1mL of DyLigh 649 labeled IgG (1mg/mL, Jackson Immunoresearch) was co-added with the QD samples to visualize the band for antibodies. The solution was centrifuged at 40krpm (SW32T Rotor, Beckman Coulter.) for 5 hours. After the centrifugation, distinctive bands for antibodies and the QD conjugates were observed (Supplementary Fig. S2). The QD conjugates were pipetted out and used for BCA assay measurements to measure the ratio between QDs and antibodies. (Supplementary methods)

Measurement of ratio of QD to Ab in the QD-Ab conjugates using BCA assay. After the purification of the QDs and QD-Ab conjugates using gradient centrifugation, the QD samples were dialyzed three times through a 50kDa molecular weight cut off spin concentrator and

concentrated down to 100μL. The concentration of the QD was then measured using the absorbance of the QD samples at 350nm and the extinction coefficient of the QD_{612}.

To measure the concentration of antibodies in QD_{612}-CD31 conjugates (QD:Ab=3:1 and 1:1), BCA reagents (Thermo Scientific, Pierce Protein Research Products) (200 μL) were combined with standard bovine serum albumin solutions (25-2000ug/mL) , QD_{612}-NB, and QD_{612}-NB-CD31 samples in triplicate. After reacting the solutions at 37°C for 30 minutes, absorbance at 562nm was measured. The net absorbance of QD_{612}-NB-CD31 was calculated by subtracting the absorbance value of QD_{612}-NB from that of QD_{612}-NB-CD31. Then, the concentration of CD31 in each QD_{612}-NB-CD31 samples was obtained by fitting the absorbance value into the standard concentration vs absorbance curve. The calculated ratio of QD to Ab for QD_{612}-NB-CD31 (3:1) and QD_{612}-NB-CD31 (1:1) was 3.6:1 and 1.3:1 respectively. (Supplementary Table S1)

3.7.3 Flow Cytometry Experiments

For peripheral blood mononuclear cell isolation, blood was harvested by heart punctuation and red blood cells were lysed by ACK lysing buffer. Cells were then washed twice and resuspended in 1% BSA in PBS. 1×10^6 lymphocytes were treated with the QDs or the QD-Ab conjugates at a concentration of 60nM in 1% BSA in PBS at room temperature for 30 minutes. The cells were washed twice with 1% BSA in PBS and analyzed for fluorescence by flow cytometry.

3.7.4 *In vivo* Imaging

Mice preparation. All animal procedures were performed following the guidelines of the Public Health Service Policy on Humane Care of Laboratory Animals and approved by the Institutional Animal Care and Use Committee of the Massachusetts General Hospital. Tie2GFP-FVB male or female mice of 6-8 weeks were obtained from MGH Cox animal facility. Either cranial or mammary fat pad window model was prepared and used right after wound healing for systemic injection of QD samples via retroorbital pathway. 50~100 μg of antibodies conjugated to relative amount of QDs were introduced per injection. For the vessel labeling, imaging was carried out at multiple time points after the QD-Ab injection and for the HSC labeling experiments, imaging was performed 20~24 hours after the QD-NB-Ab injection. Due to rapid clearance kinetics of small molecules, Hoechst 33342 was injected 15 minutes prior to the imaging.

Intravital multiphoton imaging. Two photon images were obtained with a custom-built multiphoton microscope by using a Ti:Sapphire laser (Mai-Tai Broadband; Spectra-Physics) at 840 or 900 nm, a 20× (0.5 N.A.; Olympus) water-immersion objective, and photon-counting photomultiplier tubes (H7421-40; Hamamatsu). The laser power was set to 400 mW. Three-dimensional image stacks were collected containing 21 images of 5 nm thickness and obtained at emission wavelengths appropriate for the injected particles. A maximum intensity z projection of each colored stack generated a 2D image. Images of consecutive adjacent regions in the x and y directions were combined into a montage.

3.8 Reference

1. Dabbousi BO, Rodriguez-Viejo J, Mikulec FV, Heine JR, Mattoussi H, Ober R, Jensen KF, Bawendi MG: **(CdSe)ZnS Core-Shell Quantum Dots: Synthesis and Characterization of a Size Series of Highly Luminescent Nanocrystallites**. *J Phys Chem B* 1997, **101**(46):9463-9475.

2. Bruchez M, Moronne M, Gin P, Weiss S, Alivisatos AP: **Semiconductor nanocrystals as fluorescent biological labels**. *Science* 1998, **281**:2013-2016.

3. Peng ZA, Peng X: **Formation of high-quality CdTe, CdSe, and CdS nanocrystals using CdO as precursor**. *J Am Chem Soc* 2001, **123**:183-184.

4. Zimmer JP, Kim S-W, Ohnishi S, Tanaka E, Frangioni JV, Bawendi MG: **Size Series of Small Indium Arsenide-Zinc Selenide Core-Shell Nanocrystals and Their Application to In Vivo Imaging**. *J Am Chem Soc* 2006, **128**(8):2526-2527.

5. Smith AM, Mancini MC, Nie S: **Bioimaging: Second window for in vivo imaging**. *Nat Nano* 2009, **4**(11):710-711.

6. Allen PM, Liu W, Chauhan VP, Lee J, Ting AY, Fukumura D, Jain RK, Bawendi MG: **InAs(ZnCdS) Quantum Dots Optimized for Biological Imaging in the Near-Infrared**. *J Am Chem Soc* 2009, **132**(2):470-471.

7. Resch-Genger U, Grabolle M, Cavaliere-Jaricot S, Nitschke R, Nann T: **Quantum dots versus organic dyes as fluorescent labels**. *Nature Methods* 2008, **5**(9):764-775.

8. Soper SA, Mattingly QL: **Steady-State and Picosecond Laser Fluorescence Studies of Nonradiative Pathways in Tricarbocyanine Dyes: Implications to the Design of Near-IR Fluorochromes with High Fluorescence Efficiencies**. *Journal of the American Chemical Society* 1994, **116**(9):3744-3752.

9. Panchuk-Voloshina N, Haugland RP, Bishop-Stewart J, Bhalgat MK, Millard PJ, Mao F, Leung W-Y, Haugland RP: **Alexa Dyes, a Series of New Fluorescent Dyes that Yield Exceptionally Bright, Photostable Conjugates**. *Journal of Histochemistry & Cytochemistry* 1999, **47**(9):1179-1188.

10. Berlier JE, Rothe A, Buller G, Bradford J, Gray DR, Filanoski BJ, Telford WG, Yue S, Liu J, Cheung C-Y *et al*: **Quantitative Comparison of Long-wavelength Alexa Fluor Dyes to Cy Dyes: Fluorescence of the Dyes and Their Bioconjugates**. *Journal of Histochemistry & Cytochemistry* 2003, **51**(12):1699-1712.

11. Eggeling C, Volkmer A, Seidel CAM: **Molecular Photobleaching Kinetics of Rhodamine 6G by One- and Two-Photon Induced Confocal Fluorescence Microscopy**. *ChemPhysChem* 2005, **6**(5):791-804.

12. Goldman ER, Clapp AR, Anderson GP, Uyeda HT, Mauro JM, Medintz IL, Mattoussi H: **Multiplexed Toxin Analysis Using Four Colors of Quantum Dot Fluororeagents**. *Analytical Chemistry* 2003, **76**(3):684-688.

13. Jaiswal JK, Mattoussi H, Mauro JM, Simon SM: **Long-term multiple color imaging of live cells using quantum dot bioconjugates**. *Nat Biotech* 2003, **21**(1):47-51.

14. Han M, Gao X, Su JZ, Nie S: **Quantum-dot-tagged microbeads for multiplexed optical coding of biomolecules**. *Nat Biotech* 2001, **19**(7):631-635.

15. Xu C, Zipfel W, Shear JB, Williams RM, Webb WW: **Multiphoton fluorescence excitation: new spectral windows for biological nonlinear microscopy**. *Proceedings of the National Academy of Sciences* 1996, **93**(20):10763-10768.

16. Larson DR, Zipfel WR, Williams RM, Clark SW, Bruchez MP, Wise FW, Webb WW: **Water-Soluble Quantum Dots for Multiphoton Fluorescence Imaging in Vivo**. *Science* 2003, **300**(5624):1434-1436.

17. He GS, Yong K-T, Zheng QS, Yudhisthira , Baev A, Ryasnyanskiy AI, Prasad PN: **Multi-photon excitation properties of CdSe quantum dots solutions and optical limiting behavior in infrared range**. *Opctical Express* 2007, **13**:6460-6467.

18. Xing Y, Chaudry Q, Shen C, Kong KY, Zhau HE, Chung LW, Petros JA, O'Regan RM, Yezhelyev MV, Simons JW *et al*: **Bioconjugated quantum dots for multiplexed and quantitative immunohistochemistry**. *Nat Protocols* 2007, **2**(5):1152-1165.

19. Wu X, Liu H, Liu J, Haley KN, Treadway JA, Larson JP, Ge N, Peale F, Bruchez MP: **Immunofluorescent labeling of cancer marker Her2 and other cellular targets with semiconductor quantum dots**. *Nat Biotechnol* 2003, **21**(1):41-46.

20. Ghazani AA, Lee JA, Klostranec J, Xiang Q, Dacosta RS, Wilson BC, Tsao MS, Chan WCW: **High Throughput Quantification of Protein Expression of Cancer Antigens in Tissue Microarray Using Quantum Dot Nanocrystals**. *Nano Letters* 2006, **6**(12):2881-2886.

21. Gao X, Cui Y, Levenson RM, Chung LWK, Nie S: **In vivo cancer targeting and imaging with semiconductor quantum dots**. *Nat Biotechnol* 2004, **22**(8):969-976.

22. Popović Z, Liu W, Chauhan VP, Lee J, Wong C, Greytak AB, Insin N, Nocera DG, Fukumura D, Jain RK *et al*: **A Nanoparticle Size Series for In Vivo Fluorescence Imaging**. *Angewandte Chemie International Edition* 2010, **49**(46):8649-8652.

23. Wong C, Stylianopoulos T, Cui J, Martin J, Chauhan VP, Jiang W, Popovic Z, Jain RK, Bawendi MG, Fukumura D: **Multistage nanoparticle delivery system for deep penetration into tumor tissue**. *Proceedings of the National Academy of Sciences* 2011, **108**(6):2426-2431.

24. So M-K, Xu C, Loening AM, Gambhir SS, Rao J: **Self-illuminating quantum dot conjugates for in vivo imaging**. *Nat Biotechnol* 2006, **24**(3):339-343.

25. Tada H, Higuchi H, Wanatabe TM, Ohuchi N: **In vivo Real-time Tracking of Single Quantum Dots Conjugated with Monoclonal Anti-HER2 Antibody in Tumors of Mice**. *Cancer Research* 2007, **67**(3):1138-1144.

26. Gonda K, Watanabe TM, Ohuchi N, Higuchi H: **In Vivo Nano-imaging of Membrane Dynamics in Metastatic Tumor Cells Using Quantum Dots**. *Journal of Biological Chemistry* 2010, **285**(4):2750-2757.

27. Liu W, Greytak AB, Lee J, Wong CR, Park J, Marshall LF, Jiang W, Curtin PN, Ting AY, Nocera DG *et al*: **Compact Biocompatible Quantum Dots via RAFT-Mediated Synthesis of Imidazole-Based Random Copolymer Ligand**. *J Am Chem Soc* 2010, **132**(2):472-483.

28. Liu W, Howarth M, Greytak AB, Zheng Y, Nocera DG, Ting AY, Bawendi MG: **Compact Biocompatible Quantum Dots Functionalized for Cellular Imaging**. *J Am Chem Soc* 2008, **130**(4):1274-1284.

29. unpublished work

30. Han H-S, Devaraj NK, Lee J, Hilderbrand SA, Weissleder R, Bawendi MG: **Development of a Bioorthogonal and Highly Efficient Conjugation Method for Quantum Dots Using Tetrazine–Norbornene Cycloaddition**. *Journal of the American Chemical Society* 2010, **132**(23):7838-7839.

31. Devaraj NK, Weissleder R, Hilderbrand SA: **Tetrazine-Based Cycloadditions: Application to Pretargeted Live Cell Imaging**. *Bioconjug Chem* 2008, **19**(12):2297-2299.

32. Kalyuzhny G, Murray RW: **Ligand Effects on Optical Properties of CdSe Nanocrystals**. *The Journal of Physical Chemistry B* 2005, **109**(15):7012-7021.

33. Morris-Cohen AJ, Donakowski MD, Knowles KE, Weiss EA: **The Effect of a Common Purification Procedure on the Chemical Composition of the Surfaces of CdSe Quantum Dots Synthesized with Trioctylphosphine Oxide**. *The Journal of Physical Chemistry C* 2009, **114**(2):897-906.

34. Bryant GW, Jaskolski W: **Surface Effects on Capped and Uncapped Nanocrystals**. *The Journal of Physical Chemistry B* 2005, **109**(42):19650-19656.

35. Choi HS, Liu W, Misra P, Tanaka E, Zimmer JP, Kandapallil B, Bawendi MG, Frangioni JV: **Renal Clearance of Nanoparticles**. *Nat Biotech* 2007, **25**:1165-1170.

36. Xiao K, Lia Y, Luoa J, Leea JS, Xiaoa W, Gonikb AM, Agarwalb RG, Lam KS: **The effect of surface charge on in vivo biodistribution of PEG-oligocholic acid based micellar nanoparticles**. *Biomaterials* 2011, **32**(13):3435-3446.

37. Snee PT, Chan Y, Nocera DG, Bawendi MG: **Whispering-Gallery-Mode Lasing from a Semiconductor Nanocrystal/Microsphere Resonator Composite**. *Advanced Materials* 2005, **17**(9):1131-1136.

38. Haun JB, Devaraj NK, Hilderbrand SA, Lee H, Weissleder R: **Bioorthogonal chemistry amplifies nanoparticle binding and enhances the sensitivity of cell detection**. *Nat Nano* 2010, **5**(9):660-665.

Chapter 4. Multiplexed Cytometric Immuno Imaging Reveals Normoxia in Hematopoietic Stem Cell Niche[1]

4.1 Background and Motivation

As described in the earlier chapters, QDs have numerous advantages over organic dyes as imaging fluorophores. In this chapter, we demonstrate the applications of QD antibody conjugates (QD-Ab) in single endogenous cell hematopoietic stem cell (HSC) labeling in the bone marrow of live mice. Immunomicroscopy imaging in the bone marrow has been previously performed using antibodies conjugated with organic fluorophores against chemokines and adhesion molecules [1]. However, the wide emission spectra of fluorophores limit their multiplexing *in vivo*. Additionally, the rapid photobleaching of most fluorophores can be problematic in time lapse imaging. Using QDs overcomes these limitations and allows multiplexing several specific and non-specific markers, which is critical for cell labeling *in vivo* where a variety of cells is present in confined spaces (Figure 4-1). By using QD-Ab, we were able to label endogenous hematopoietic stem cells and study their microenvironment in live mice, and that was not possible previously using the dye antibody conjugates.

[1] This work was done in collaboration with Steele laboratory at Massachusetts General Hospital.

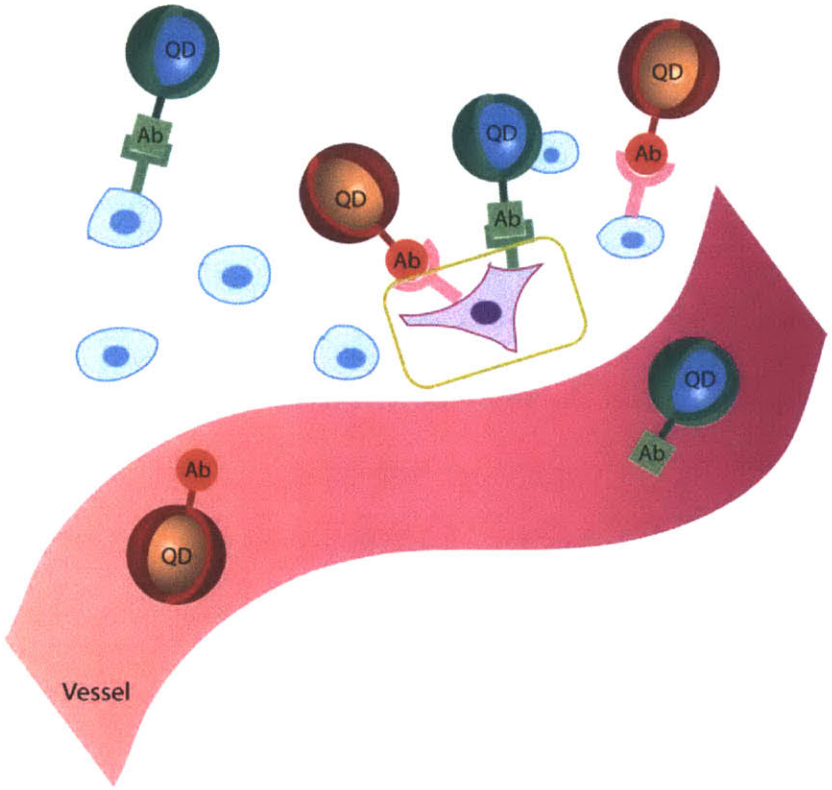

Figure 4-1 Schematic of *in vivo* labeling using the multiple QD-Ab conjugates. The purple cell is labeled with two types of QD-Ab.

The stem cell niche is a highly specialized microenvironment that provides signals for regulating the asymmetric division of stem cells. These local cues control differentiation into cell progenies while maintaining a constant source of stem cells. In the bone marrow, all blood cells are generated by HSCs throughout the lifetime of the organism. While the function of HSC has been well characterized, the cellular composition and location of the niche in which they reside have remained elusive due to lack of appropriate methodologies. Previous studies have shown that HSCs may localize both in endosteal and peri-vascular regions of the bone marrow [2-5]. However, histological techniques commonly used to identify the endogenous HSCs lack the ability to measure the dynamics or physiology of the niche [2, 4, 5]. On the other hand, available

intravital microscopy systems can follow cell dynamics, but have not yet succeeded in tracking endogenous HSCs in the intact marrow. Previous studies have focused on tracking infused HSCs in pre-irradiated or genetically modified bone marrow [1, 3, 6]. Because of that, the functional differences and potential cross-talk between the HSCs and the bone marrow microenvironment in which they reside remain unresolved (reviewed in [7]). For example, the presence of a low oxygen (hypoxic) environment in the "niche" has been proposed for decades as a key physiological signal controlling HSC quiescence. Moreover, oxygen gradients are thought to regulate the direction of HSC differentiation within the niche (reviewed in [8]). However, these hypotheses have not been directly confirmed due to the lack of ability to directly measure oxygen gradients in HSC "niches."

In this chapter, we combine newly developed quantum dot (QD) antibody conjugates (QD-Ab) with a novel chronic bone marrow window preparation to image endogenous HSCs. This new approach allows us to localize the HSCs and measure the oxygenation in the niche.

4.2 Transvasular Transport within the Bone Marrow

Prior to using the QD immunocontructs for *in vivo* cytometry, we characterized the transvascular transport of macromolecules of comparable sizes within the bone marrow using previously developed techniques [9]. Analysis of the structure of the bone marrow vasculature showed the presence of a characteristic sinusoidal capillary network [10]. Direct quantification of the extravasation rate of macromolecules in these vessels revealed a significant extravasation of macromolecules as high as MW 500 kDa. To quantify the rate of extravasation of macromolecules, we performed multiphoton intravital microscopy of the bone marrow before and at several time points after injection of TAMRA-BSA. We quantified vascular permeability

at multiple positions along the vessel wall surface using a method previously developed by our collaborators [9]. BSA extravasated within few minutes and accumulated in the bone marrow (Figure 4-2). Median permeability was 7.6 [25 percentile = 4.6, 75 percentile = 13.1] × 10^{-7} cm/s. These high values are comparable to the permeabilities that were previously measured in tumor vessels, and are significantly higher than the vascular permeability measured in normal skin or brain [11-13]. Therefore, we conclude that the bone marrow vessels were highly permeable to macromolecules (Figure 4-2).

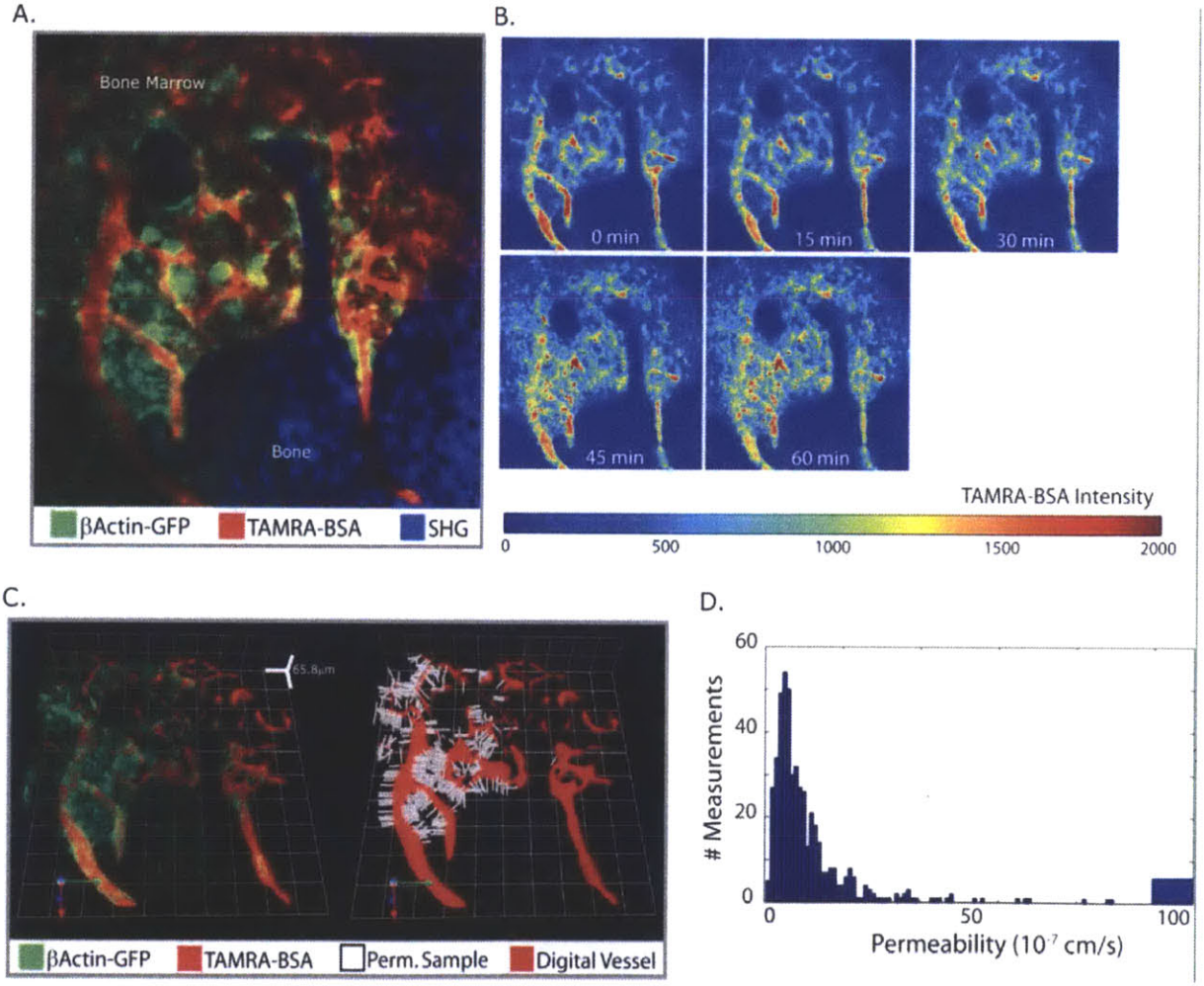

Figure 4-2 Bone marrow vessels are hyperpermeable to albumin. (A) Representative image of the bone marrow after injection of rhodamine albumin (TAMRA-BSA - red) in a Actb-GFP mouse (bone marrow cells are shown in green, and the bone in blue – by SHG) using

multiphoton intravital microscopy. (B) TAMRA-BSA intensity heat map showing extravasation of albumin over time which is detectable within 15 and 30 minutes after i.v. injection. (C) Analysis of vessel permeability. Vessels are segmented and rods are randomly selected in 3D. BSA accumulation is quantified in each rod. (D) Histogram of permeability quantified along spots along the vessel wall surface.

4.3 Kinetics of Hoechst33342 Cell Labeling in the Intact Bone Marrow

HSCs express multidrug resistance 1 (MDR1) that inhibits the transport of Hoechst33342 (H33342) dye. Based on this finding, *in vitro* HSCs-identification assays have been developed to use H33342 exclusion as a specific stem cell marker [14, 15]. In this study, we used H33342 for *in vivo* labeled of HSCs. The *in vivo* H33342 staining is not only dependent on MDR1 expression but also on H33342 delivery to the bone marrow cells. A recent study used H33342 to assess the distance to the closest vessel of cells based on H33342 delivery 10 minutes after injection [16]. In order to reliably use H33342 as a specific negative marker for HSCs *in vivo*, we characterized the kinetics of H33342 cell labeling *in vivo* by imaging cells before and at multiple time-points after H33342 ranging from 5 to 82 minutes (Figure 4-3). HSCs were identified using two specific positive markers (c-Kit and Sca-1). Nuclear staining by H33342 was detectable as soon as 5 minutes after i.v. injection and reached its maximum level within 10-15 minutes in most cells. This rapid and homogeneous uptake of H33342 indicated that 30 minutes after H33342 injection, H33342 intensity is not related to its delivery but to its transport in and out of cells. In most c-Kit$^+$ Sca-1$^+$ cells (>90%), the nuclear staining by H33342 was significantly dimmer or completely absent when compared to c-Kit$^-$ Sca1$^-$ cells. At the time-points imaged, the kinetics of uptake of H33342 by HSCs did not show any increase. This suggests that H33342 rate of influx to the cell is slower than that of its rate of efflux. The presence of H33342 dim cells and negative cells may be related to higher and lower activity of MDR1 in a subset of HSCs.

This result demonstrated the applicability of H33342 as a specific negative marker for HSCs. Given the fast uptake of H33342 by bone marrow cells, we imaged analyzed HSCs and bone marrow cells one hour after H33342 injection.

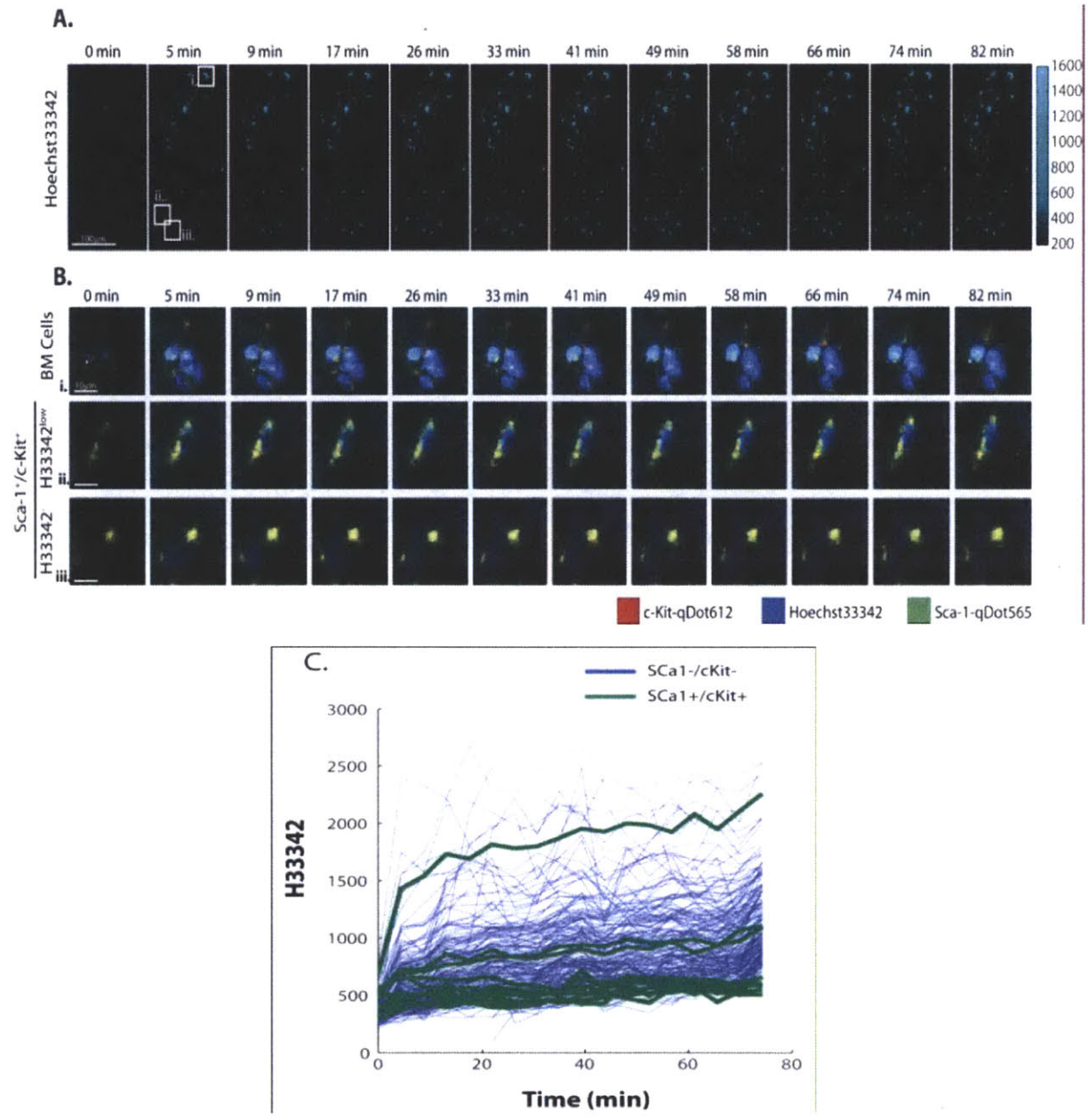

Figure 4-3 Kinetics of Hoechst333342 uptake by bone marrow cells. (A) Representative images of time-lapse multiphoton intravital micrscoscopic imaging of the bone marrow before and after i.v. injection of Hoechst33342 (H33342). Cell nuclei appear positively stained as soon as 5

minutes after H33342 injection and reach maximum intensity after 10 minutes. Bone marrow (BM) cells nuclei uptake H33342 independently of their location relative to bone. (B) Identification of c-Kit$^-$Sca-1$^-$H33342$^+$ cells (i), c-Kit$^+$ Sca-1$^+$ H33342^{low} cells (ii), and c-Kit$^+$ Sca-1$^+$ H33342$^-$ cells (iii) in the bone marrow. (C) Plot of H33342 intensity over time of single cells collected in two time lapses. H33342 increases within few minutes reaching maximum intensity in less than 20 minutes. Most c-Kit$^+$ Sca-1$^+$ cells are H33342$^{-\text{ or low}}$.

4.4 Identification of Hematopoietic Stem Cells *In vivo*

The endogenous HSCs were identified as cells that expressed Sca-1 and c-Kit and excluded the nuclear dye Hoechst33342. Time-lapse imaging showed rapid uptake of the nuclear dye Hoechst33342 in bone marrow cells but not in c-Kit$^+$ Sca-1$^+$ cells, confirming its HSC specificity (Figure 4-3). Finally, the bone marrow vasculature was detected using contrast angiography (circulating QD-immunoconstructs) or transgenic mice selectively expressing GFP in endothelial cells (Tie2-GFP mice), and the bone was imaged using second harmonic generation microscopy [3] (Figure 4-4, 4-5, and 4-6).

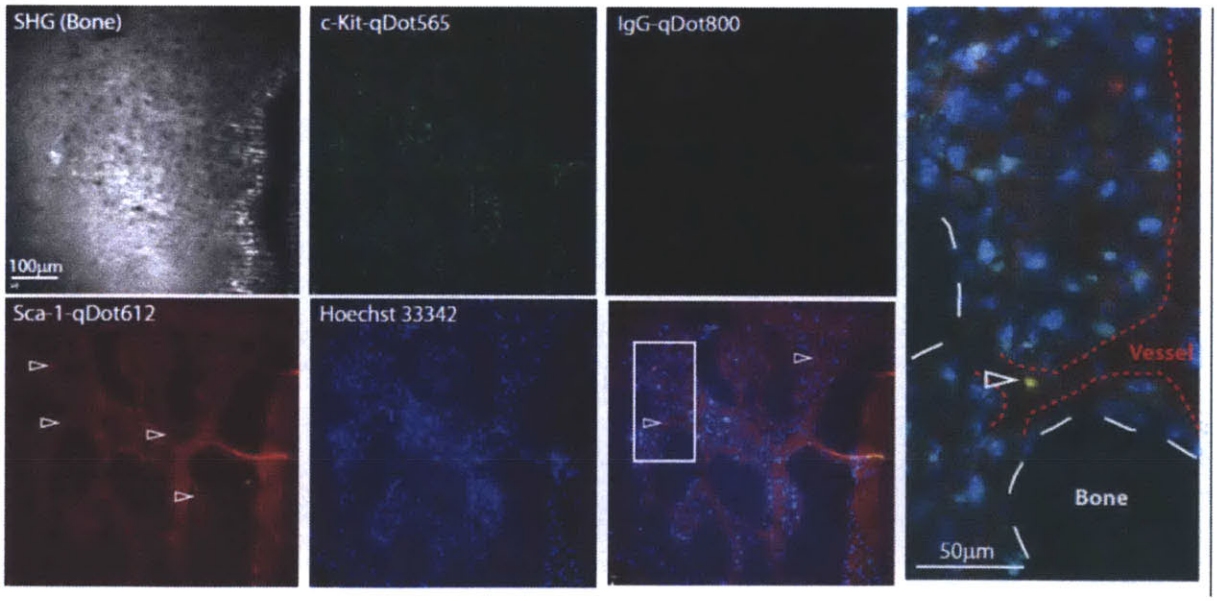

Figure 4-4 Representative multiphoton microscopy images of a bone marrow cavity with cells stained using the nuclear dye Hoechst33342 (blue), rat c-Kit-qDot565 (green), rat Sca-1-

qDot612 (red), and rat IgG-qDot800 (gray) antibodies. Bone is imaged using second harmonic generation (SHG – in gray). HSCs are identified as c-Kit^{+} Sca-1^{+} Hoechst33342$^{low/-}$ (arrowhead).

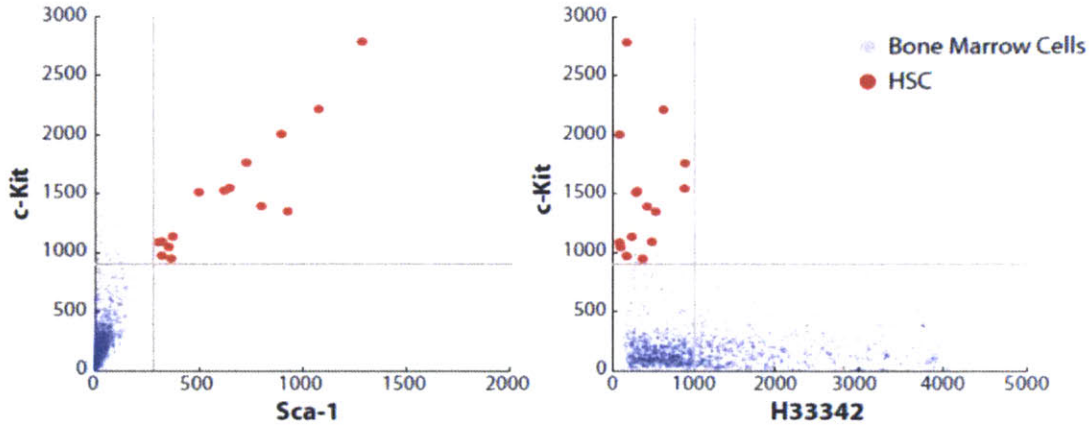

Figure 4-5 Representative intravital cytometric analysis from a multiphoton intravital volume. Scatter plots of c-Kit vs. Sca-1 and c-Kit vs. Hoechst33342 staining of bone marrow cells illustrating the thresholds used to define HSCs.

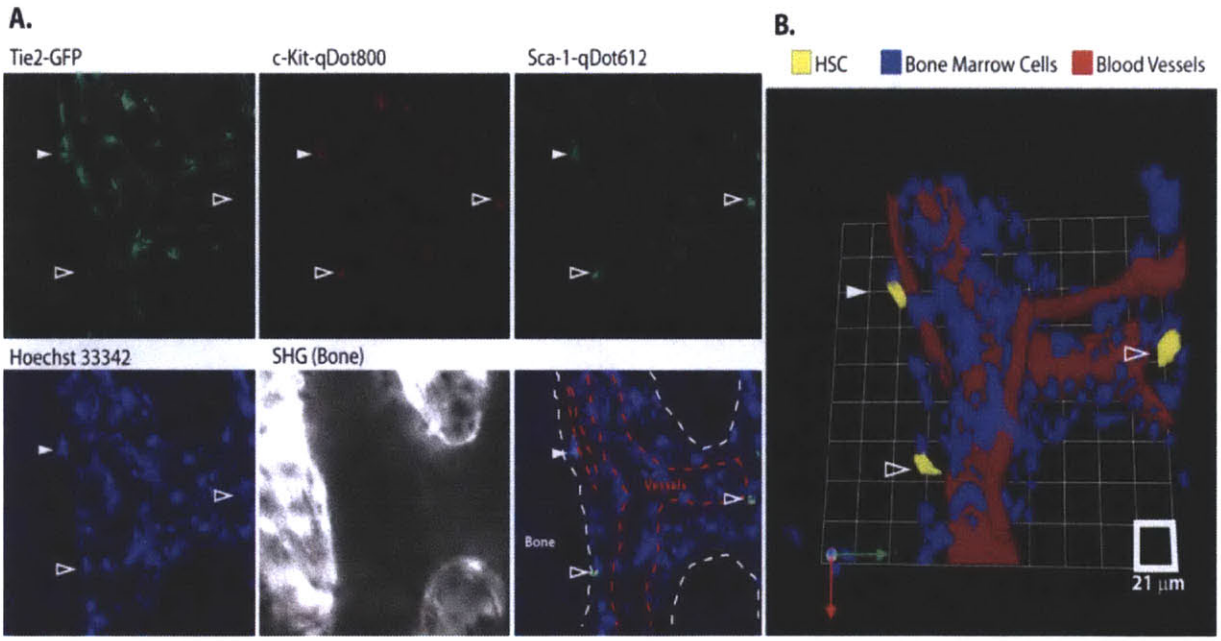

Figure 4-6 Imaging HSCs in Tie2-GFP mice. Multiphoton intravital images of bone marrow cavities in a Tie2-GFP mouse. (A) Single color images of Tie2, c-Kit, Sca-1, Hoechst 33342, and bone. (B) Three-dimensional reconstruction of the bone marrow cavity showing cells (blue), HSCs (yellow) and blood vessels (red). HSCs were defined as c- Kit^{+} Sca1^{+} Hoechst33342$^{low/-}$

cells (unfilled arrowhead). We noticed c-Kit^{+} Sca1^{+} Hoechst33342^{low} cells that are in some cases Tie2+ (filled arrowhead).

4.5 Where Do the HSCs Reside?

4.5.1 Single Vessel Cavities (SVCs) vs Multiple Vessels Cavities (MVCs)

By analyzing the bone marrow vasculature structure, we found that cavities of the calvarial bone marrow can be classified physiologically into single vessel cavities (SVCs) and multiple vessels cavities (MVCs). SVCs are characterized by a tube-like structure with one central vessel surrounded by up to 3 cell layers. MVCs are defined by larger cavities with a more complex vessel network (see Figure 4-7). The analysis show thatHSCs reside predominantly in SVCs (12.5 per 1000 cells in SVCs compared to 3.8 per 1000 cells in MVCs; $p < 0.05$). The architecture of SVCs is anatomically optimal for HSCs to be in close proximity to vessels and bone.

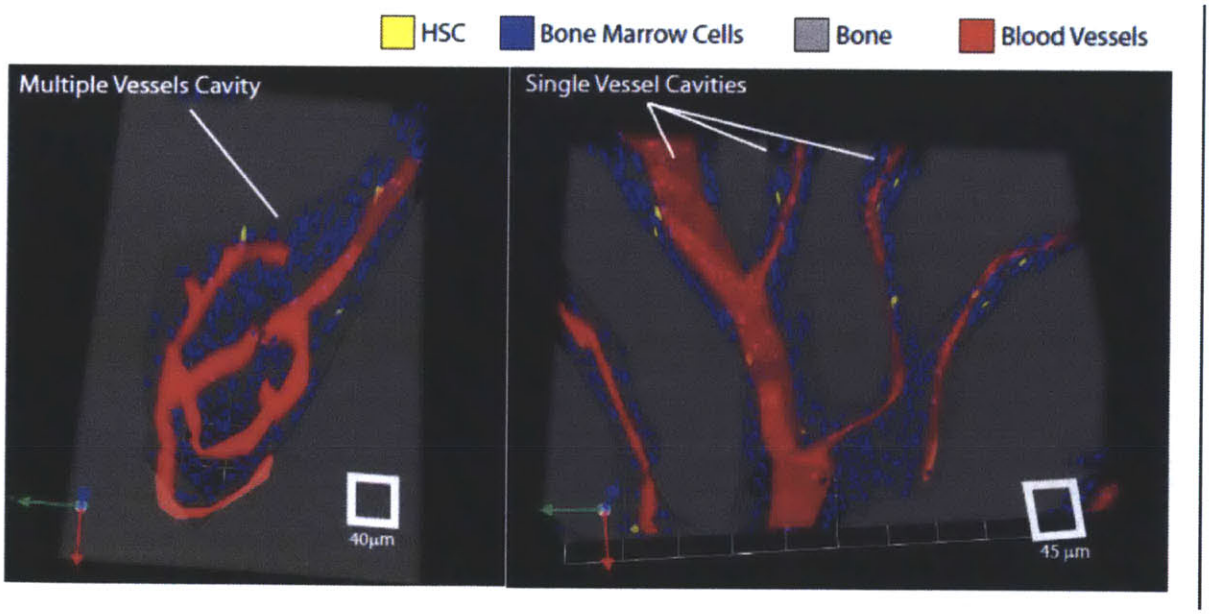

Figure 4-7 Three-dimensional reconstruction of the bone marrow cavity showing bone (gray), cells (blue), HSCs (yellow) and blood vessels (red). Representative images of single vessel

cavities (SVCs) and multiple vessels cavities (MVCs) illustrate the density and preferential localization of HSCs.

4.5.2 Distance from Vessels and Bones

Three-dimensional analysis showed that endogenous HSCs are in close proximity (< 25 μm) to both blood vessels and bone independently of the type of cavity in which they reside (Figure 4-8). These results suggest that HSCs can interact with vascular and perivascular cells as well as endosteal cells following the model discussed in review [7] and are consistent with studies that imaged transplanted HSCs in pre-irradiated animals [3].

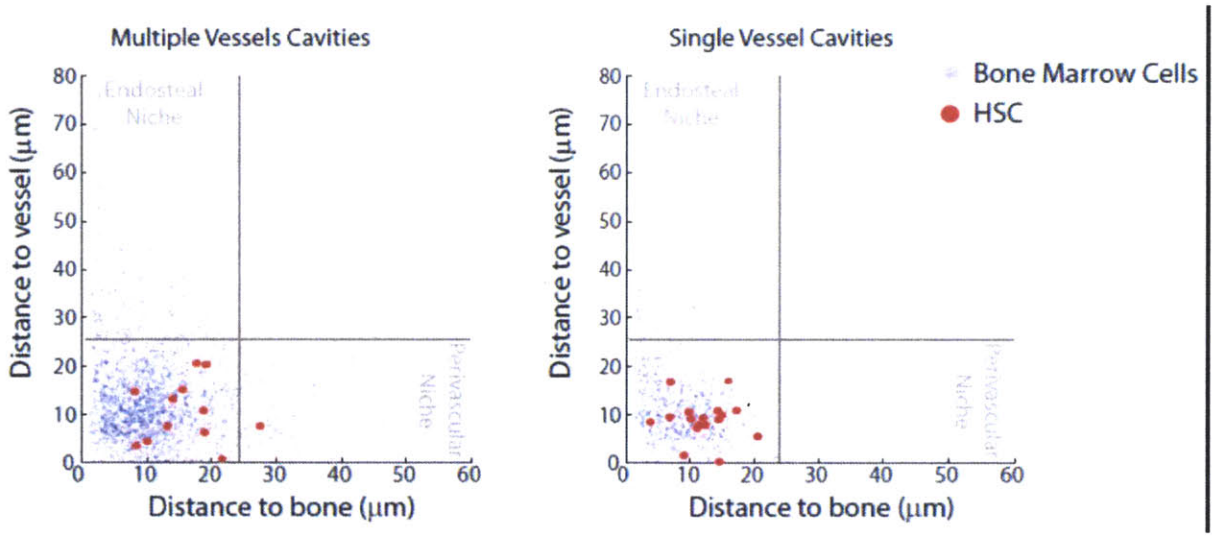

Figure 4-8 Scatter plot of bone marrow cells and HSCs showing their spatial distribution relative to bone (distance to the closest bone trabeculae) and vessel (distance to the closest vessel).

4.6 Oxygen Level of the HSC "niche"

To assess HSC "niche" oxygenation, we used two-photon phosphorescence lifetime quenching microscopy [17]. Analysis of bone marrow oxygenation (>9700 measurements, using 4 mice) showed pO_2 measurements that ranged between 20-100 mmHg, and no areas of hypoxia

(<10 mmHg) (see Figure 4-9 and 4-10). Areas of low oxygen (15<pO_2<20 mmHg) encompass less than 1% of the total measured area. Endosteal pO_2 was variable depending on the position of the nearest vessel, but was always over 10 mmHg. Specific measurement of pO_2 within the HSC niche (bone marrow cavities in which HSCs reside) showed that endogenous HSCs reside in normoxic areas – in contrast to the widely held view that these niches are hypoxic (Figures 4-10 and 4-11). The niches localized in SVCs were characterized by slightly lower and more homogenous pO_2 levels as compared to niches in MVCs (Figure 4-11D). Mapping pO_2 within SVCs, which are rich in HSCs, showed a characteristic steep gradient decreasing from the central vessel to the endosteal area. This well-defined gradient seen in SVCs is very different from the more complex oxygenation distribution in MVCs (Figure 4-10 & 4-11A-C). To further characterize the HSC microenvironment, we measured pO_2 in the close proximity of HSCs (< 3μm distance). We found that the pO_2 in the vicinity of HSCs was not significantly lower than the average oxygenation of the cavity in which the HSCs resided (Figure 4-11E). This shows that HSCs do not preferentially localize in areas with low oxygenation.

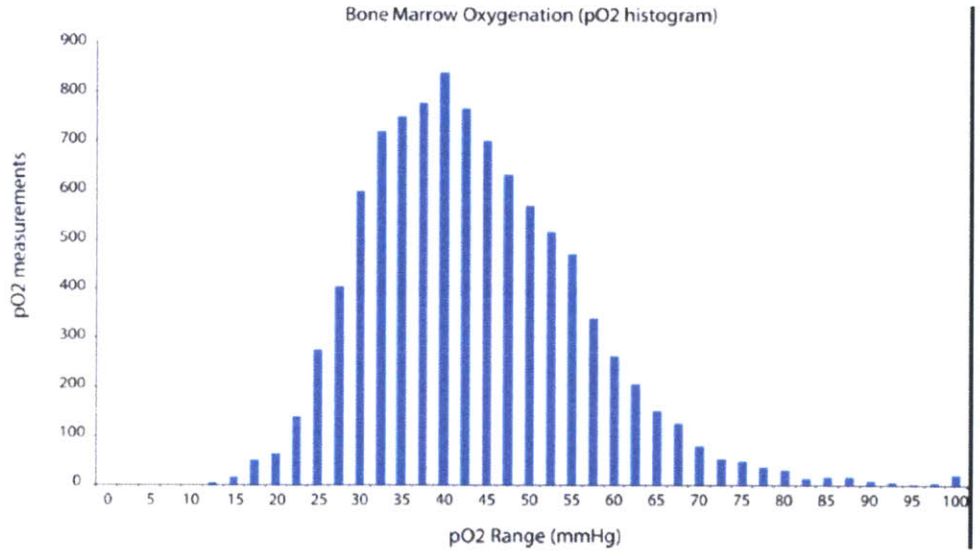

Figure 4-9 Histogram of pO_2 measurements in the bone marrow collected in 1-2 cavities in 4 mice.

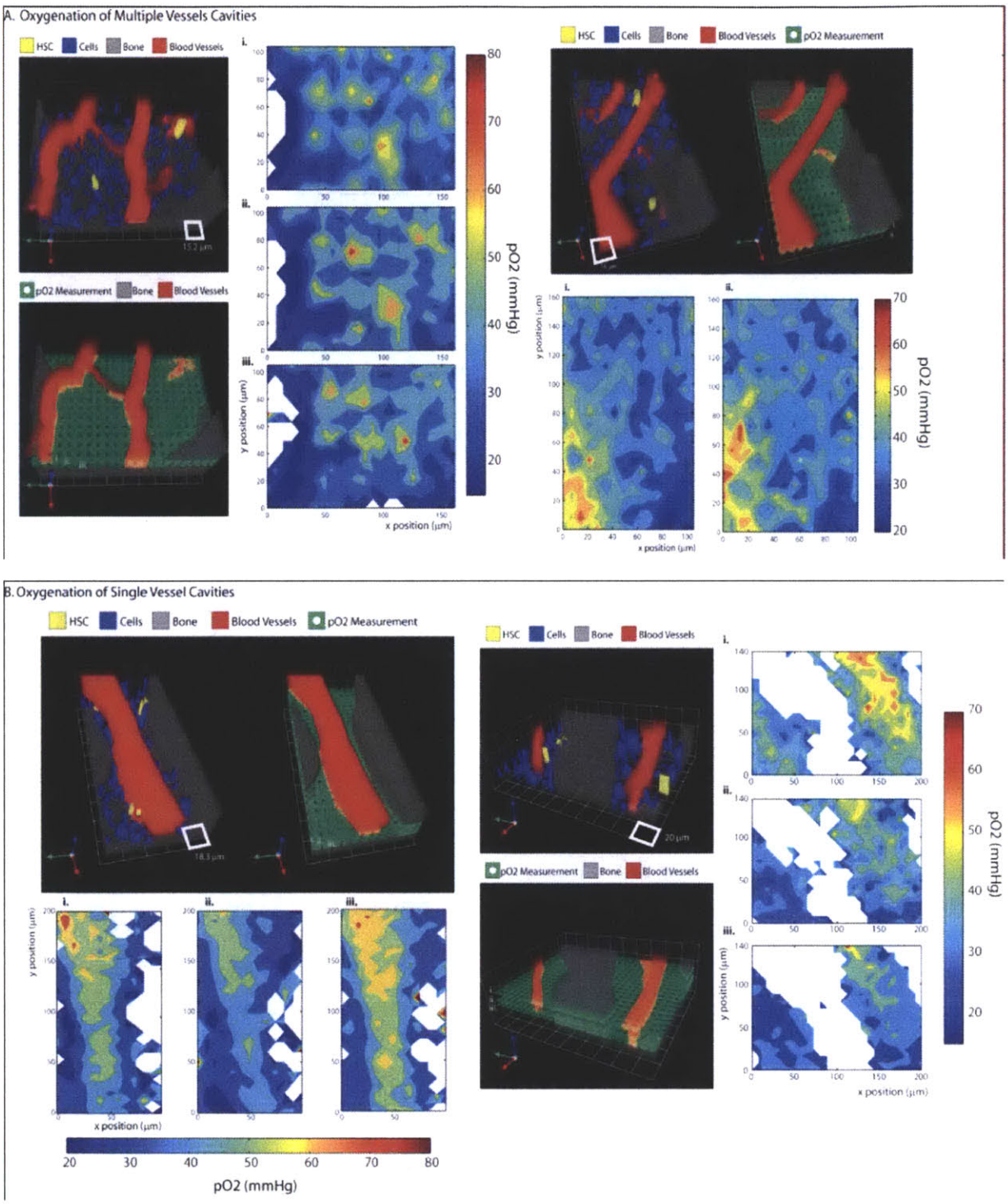

Figure 4-10 pO_2 within HSC niches. Representative images and pO_2 maps of bone marrow cavities in which HSCs are identified. Three-dimensional reconstruction of the bone marrow cavity showing bone (gray), cells (blue), HSCs (yellow) and blood vessels (red). The green plane shows the depth at the specific locations where pO_2 measurements were performed. Surface plots

of pO_2 extracted from pO_2 measurements using PQM. (A) Representative multiple vessels cavities showing heterogeneous oxygen distribution mapping the complexity of the vessel network. (B) Representative single vessel cavities showing an O_2 gradient within the niche going from the central vessel to the endosteal area.

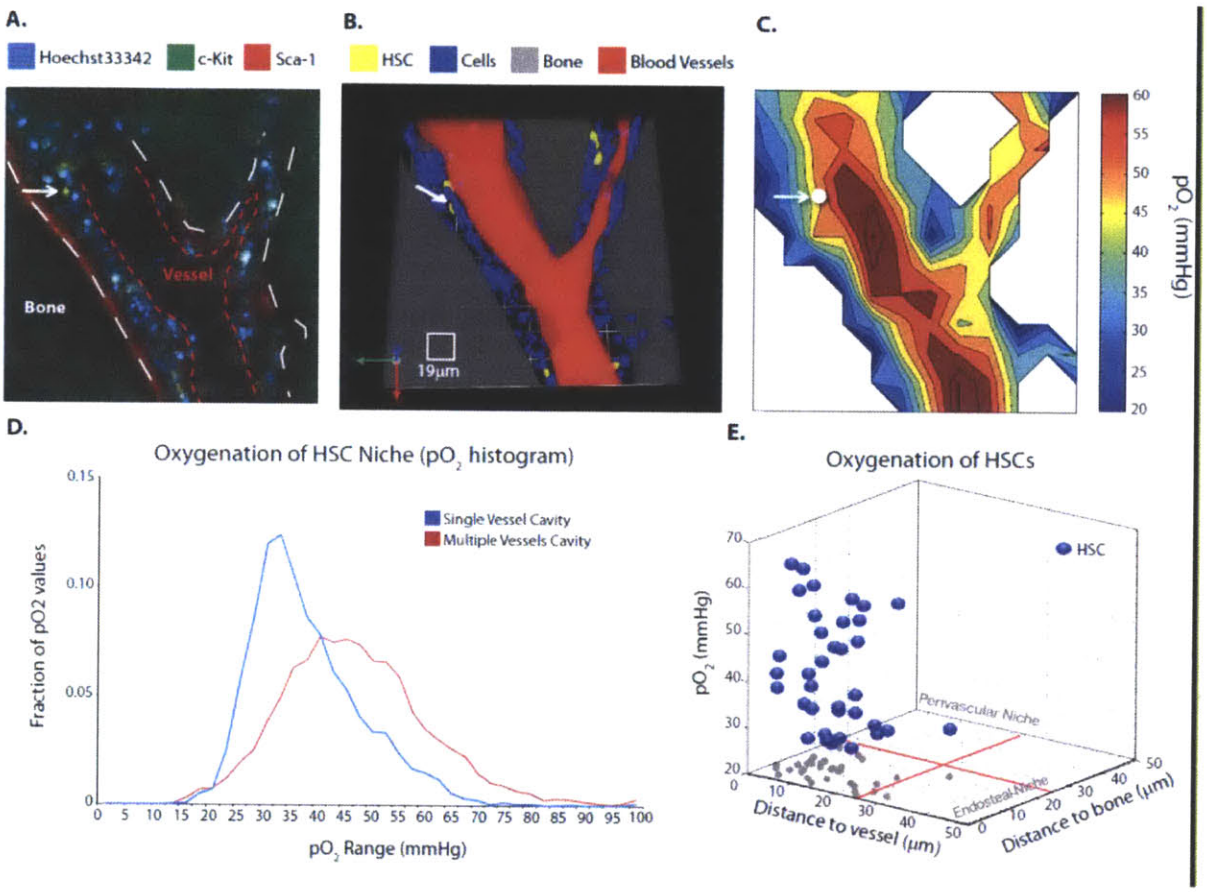

Figure 4-11 (A) Representative multiphoton microscopy image of a bone marrow cavity with cells stained with the nuclear dye Hoechst33342 (blue) and HSCs identified by antibodies against c-Kit (linked with qDot612 in red) and ScA-1 (linked with qDot575 in green) and Hoechst33342 exclusion. HSCs appear yellow with no nuclear staining (white arrow). (B) Three dimensional reconstruction of the bone marrow cavity showing bone (gray), cells (blue), HSCs (yellow – white arrow) and blood vessels (red). (C) A surface plot of pO_2 extracted from pO_2 measurements using phosphorescence quenching microscopy. pO_2 map shows the O_2 gradient within the niche from the central vessel to the endosteal area. (D) Histogram of pO_2 measurements performed in HSC niches (bone marrow cavities in which HSCs reside) comparing single vessel cavities (1784 pO_2 measurements performed in 5 cavities) and multiple vessels cavities (7575 pO_2 measurements performed in 7 cavities) (n=5 mice). (E) Scatter plot of HSCs' spatial distribution relative to bone (distance to the closest bone trabeculae) and vessel (distance to the closest vessel).

4.7 Imaging of HSCs in the Intact Bone Marrow in Tie2-GFP Transgenic Mice

In order to image endothelial cells within the bone marrow, we performed bone marrow intravital microscopy in Tie2-GFP/FVB (Tie2-GFP) mice. Although Tie2 is known to be specifically expressed by endothelial in most tissues, Tie2 expression was described by several bone marrow derived cells including Tie2 expressing monocytes [18] and a subset of HSCs [4]. We were able to identify endothelial cells based on Tie2 expression and endothelial cell morphology. Three-dimensional analysis showed that endogenous HSCs were found in close proximity to the bone and vessel (Figure 4-6, arrows). As in previous studies, we found that Tie2 expression was not limited to endothelial cells but also included in unidentified bone marrow cells and a subset of HSCs.

4.8 Conclusion

In summary, we utilized newly developed QD-Ab conjugates and chronic bone marrow windows to directly image endogenous HSCs *in vivo* in intact bone marrow niche and probe the HSC microenvironment. By labeling the endogenous HSCs using the QD-Ab conjugates, we showed that HSCs localize in close proximity to both blood vessels and bone trabeculae, and HSCs reside in a normoxic microenvironment characterized by an oxygen gradient between the endosteal surface and blood vessels. This would not be possible with the traditional methods using dye conjugated antibodies due to their broad emission profiles and the low two photon cross sections. It remains to be established whether niches in other tissues, in which the cells remain local to maintain or reconstitute the anatomy, are also normoxic.

4.9 Experimental Section

4.9.1 Chronic Bone Marrow Window Preparation

We developed a chronic window model for calvarial bone marrow imaging that allows imaging the bone marrow over several days. The model is based on the acute preparation model originally developed by Mazo et al. [19]. In summary, the anesthetized mouse (ketamine 90 mg/kg and xylazine 9 mg/kg) is laid on a rigid plate equipped with a heating pad and its head shaved. A longitudinal skin incision is made on the skull and the skin is removed. Connective tissue and periosteum is removed using fine forceps. A coverslip is placed on top of the calvarial bone and fixed to the bone using glue and plastic powder.

We performed single photon imaging of the bone marrow of Actb-GFP/C57BL/6 (Actb-GFP) mice and found that bone marrow can be imaged from day 0 and until day 8 without any inflammation or hemorrhage (Figure 4-12). We performed multiphoton intravital imaging and found that the bone marrow can be imaged at high resolution and with a penetration depth of 150-200 μm. This penetration depth is sufficient to image bone marrow cavities which are at around 50 μm depth.

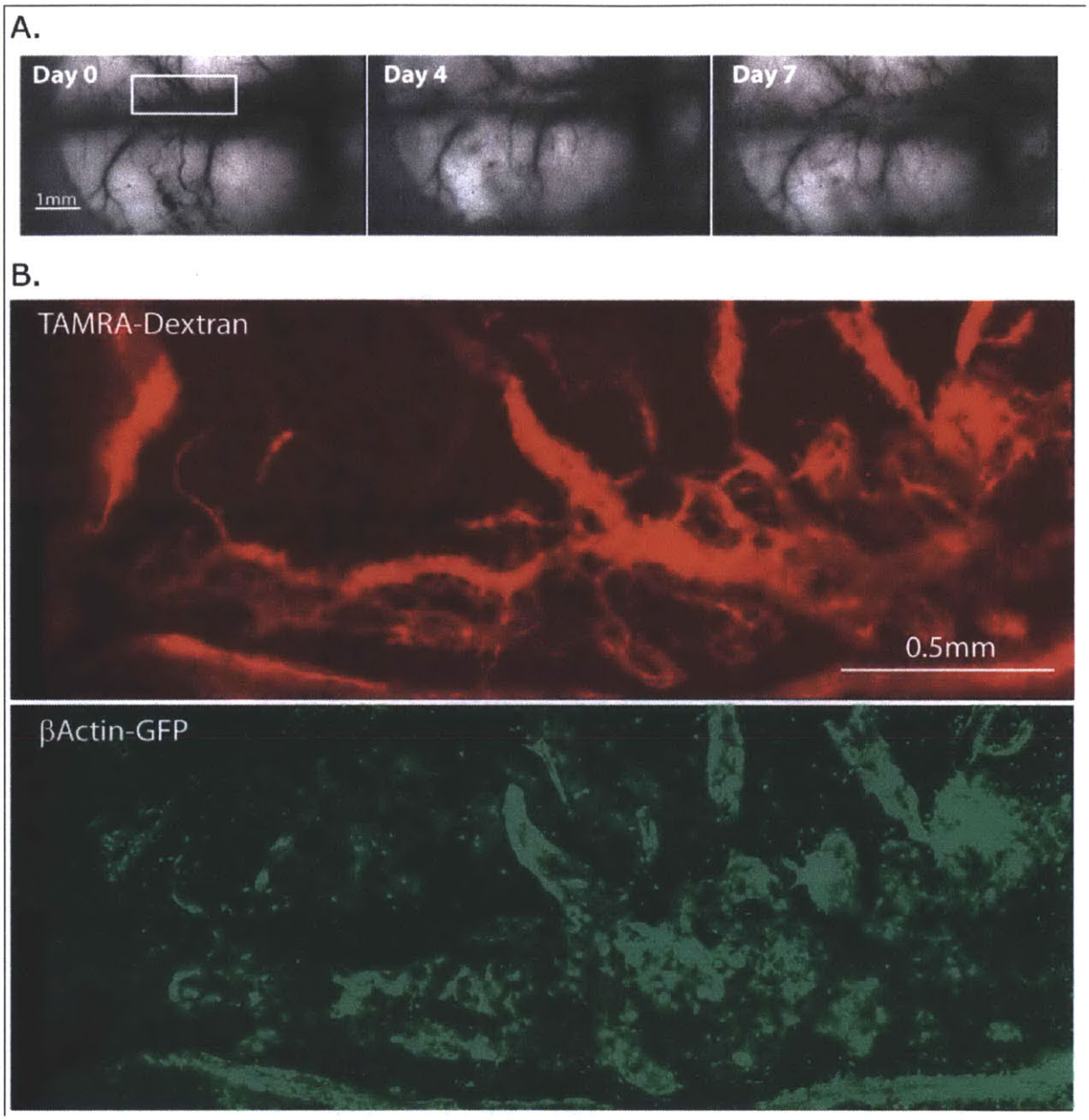

Figure 4-12 Bone marrow intravital microscopy through the chronic bone marrow window. (A) Representative single photon image of the bone marrow of a Actb-GFP mouse monitored over a period of 7 days. The overall vascular network (dark structures) around the central sinus was readily identifiable and could be imaged over several days with no apparent signs of inflammation or hemorrhage. (B) Composite image of several fields in the bone marrow using multiphoton intravital microscopy. Vessels were imaged after injection of angiographic contrast (TAMRA-Dextran MW 500 kDa injected i.v.). Bone marrow cells were imaged based on the endogenous expression of GFP under the ubiquitous promoter for cytoskeleton protein β-actin.

4.9.2 Multiphoton Intravital Imaging Setup and Image Analysis

In vivo multiphoton laser scanning microscopy was performed as previously described [9] on a custom-built multiphoton laser-scanning microscope using confocal laser-scanning microscope body (Olympus 300; Optical Analysis Corp.) and a broadband femtosecond laser source (High Performance MaiTai, Spectra-Physics).

Antibodies. We used c-Kit antibody (CD117/c-kit/2B8, BD Bioscience), Sca-1 antibody (Ly-6A/E/Sca-1/Purified/E13161.7, BD Bioscience) and non-specific rat IgG. For all antibodies we injected the 50 μg of antibodies (50 μg based on non-conjugated antibodies) into the animal retro-orbitally and have imaged 24 hours and 48 hours after injection.

Imaging parameters. In order to multiplex several colors, we used optimal band-pass filters and different excitation wavelengths. Specifically, qdot565 was imaged using excitation at 840nm and a 535-100 nm band pass filter; qdot600 was imaged using excitation at 840nm and a 605-50 nm band pass filter; qdot612 was imaged using excitation at 840nm and a 610-50 nm band pass filter; qdot800 was imaged using excitation at 840nm and a 750-100 nm band pass filter; Hoechst33342 was imaged using excitation at 820-840nm and a 450-50 nm band pass filter; second harmonic generation (bone) was imaged using excitation at 900nm and a 450-50 nm band pass filter; Tie2-GFP was imaged using excitation at 900nm and a 535-50 nm band pass filter.

Image analysis. All the image analysis was performed using algorithms developed in-house implemented on Matlab (Mathworks). Bone was imaged based on second harmonic generation (SHG) and was digitized using threshold and manual drawing. Vessels were identified by *in vivo* staining by antibody infusion or by endogenous GFP expression under the endothelial promoter Tie2 (in Tie2-GFP mice). The vessels were digitized using thresholding and an active contour

model as described [20]. Nuclei were imaged using Hoechst33342 dye and segmented using a recursive threshold method combined with post-processing manual corrections. Distance to bone and distance to vessel was generated using Matlab distance map function and each cell distance was measured as the average distance of all its pixels. All 3-*D* reconstructions were rendered using Volocity (Improvision Ltd.).

Phosphorescence quenching multiphoton microscopy. We measured pO2 in the bone marrow using phosphorescence quenching multiphoton microscopy(PQM). PQM has been previously used to measure both vascular and interstitial pO2 *in vivo* [21, 22]. Recently, PQM was adapted to multiphoton microscopy (MP-PQM), which allows quantification of pO2 at high resolution (~1μm) and at high depths [17]. In summary, MP-PQM was performed using single photon counting triggered by the selection of pulses of the excitation source. This technique allows signal integration (integration time at 6.5s), improves signal to noise ratio, and the result can be analyzed through fitting a two components lifetime decay model. The MP-PQM system incorporates a KD*P Pockels cell (Model: 350-50; Conoptics, Inc., Danbury, CT) electro-optic modulator, an amplifier driver as the temporal gate for pulse selection, and an oscilloscope to monitor the optical response. The excitation pulses ranged from 1.28 to 15.36 μs in duration indicating that sample excitation was performed by a train of femtosecond Ti:Saphire laser pulses ranging in number from 100 to 1230 nm. The laser excitation wavelength used was 1020nm. Photon counting was performed using a multichannel scaler (SR340, SRS, Sunnyvale, CA) to histogram the counts to 1024 bins. Phosphorescence emission (~690nm) of oxyphorR2 (Oxygen Enterprises, Ltd., Philadelphia PA) was detected using a GaAs photomultiplier tube (PMT; H7421-50, Hamamatsu, Inc., Bridgewater, NJ). Given the short spectral separation between the emission wavelength and the excitation wavelength we used a short-pass (<750nm)

AR-coated filter. We have also used a 690/90 nm band pass filter to limit noise. Lifetime measurements were performed by a stationary beam and not in scanning mode.

Physiological monitoring of mice during intravital microscopy. During intravital microscopy mice were anesthetized using isofluorane (1%-2% in 100% Air) that is known to have minimal effects on animal baseline physiology [23]. The animal systemic physiology was monitored during multiphoton intravital imaging by measuring oxygen saturation, heart rate and breathing rate using a mouse Oxymeter (STARR Life Sciences Corp). Isoflurane levels were adjusted depending on heart rate and oxygen saturation. When oxygen saturation was lower than 97% for more than 5 minutes despite adjusting anesthesia, imaging was stopped and the data were excluded from analysis.

Measurements of oxygenation in the intact bone marrow. We characterized bone marrow oxygenation by quantifying pO_2 along a grid with a 10μm resolution covering 200x200μm at three different depths. We have quantified oxygenation in two to three cavities in 5 animals and have combined all the measurements (9716 measurements) in a pO_2 histogram (Figure 4-8). We detected no areas of hypoxia, and pO_2 ranged between 20-100 mmHg. Endosteal pO_2 varied depending on the position of the nearest vessel, but was always over 10 mmHg.

pO_2 maps in bone marrow cavities. We measured pO_2 using phosphorescence quenching in bone marrow cavities where HSCs were identified. Measurements were made in single vessel cavities and multiple vessels cavities along a grid with 7-15 μm resolution at one to three depths (Figure 4-9). pO_2 distribution in multiple vessel cavities is heterogeneous and correlates with the complexity of the vessel network. Single vessel cavities have a well-defined O_2 gradient going from the central vessel to the endosteal area.

4.10 References

1. Sipkins DA, Wei X, Wu JW, Runnels JM, Cote D, Means TK, Luster AD, Scadden DT, Lin CP: **In vivo imaging of specialized bone marrow endothelial microdomains for tumour engraftment**. *Nature* 2005, **435**(7044):969-973.

2. Kiel MJ, Yilmaz ÖH, Iwashita T, Yilmaz OH, Terhorst C, Morrison SJ: **SLAM Family Receptors Distinguish Hematopoietic Stem and Progenitor Cells and Reveal Endothelial Niches for Stem Cells**. *Cell* 2005, **121**(7):1109-1121.

3. Lo Celso C, Fleming HE, Wu JW, Zhao CX, Miake-Lye S, Fujisaki J, Cote D, Rowe DW, Lin CP, Scadden DT: **Live-animal tracking of individual haematopoietic stem/progenitor cells in their niche**. *Nature* 2009, **457**(7225):92-96.

4. Arai F, Hirao A, Ohmura M, Sato H, Matsuoka S, Takubo K, Ito K, Koh GY, Suda T: **Tie2/Angiopoietin-1 Signaling Regulates Hematopoietic Stem Cell Quiescence in the Bone Marrow Niche**. *Cell* 2004, **118**(2):149-161.

5. Nilsson SK, Johnston HM, Coverdale JA: **Spatial localization of transplanted hemopoietic stem cells: inferences for the localization of stem cell niches**. *Blood* 2001, **97**(8):2293-2299.

6. Xie Y, Yin T, Wiegraebe W, He XC, Miller D, Stark D, Perko K, Alexander R, Schwartz J, Grindley JC *et al*: **Detection of functional haematopoietic stem cell niche using real-time imaging**. *Nature* 2009, **457**(7225):97-101.

7. Kiel MJ, Morrison SJ: **Uncertainty in the niches that maintain haematopoietic stem cells**. *Nat Rev Immunol* 2008, **8**(4):290-301.

8. Eliasson P, Jönsson J-I: **The hematopoietic stem cell niche: Low in oxygen but a nice place to be**. *Journal of Cellular Physiology* 2010, **222**(1):17-22.

9. Brown EB, Campbell RB, Tsuzuki Y, Xu L, Carmeliet P, Fukumura D, Jain RK: **In vivo measurement of gene expression, angiogenesis and physiological function in tumors using multiphoton laser scanning microscopy**. *Nature Medicine* 2001, **7**(7):864-868.

10. Becker RP, De Bruyn PPH: **The transmural passage of blood cells into myeloid sinusoids and the entry of platelets into the sinusoidal circulation; a scanning electron microscopic investigation**. *American Journal of Anatomy* 1976, **145**(2):183-205.

11. Kamoun WS, Ley CD, Farrar CT, Duyverman AM, Lahdenranta J, Lacorre DA, Batchelor TT, di Tomaso E, Duda DG, Munn LL *et al*: **Edema Control by Cediranib, a**

Vascular Endothelial Growth Factor Receptor–Targeted Kinase Inhibitor, Prolongs Survival Despite Persistent Brain Tumor Growth in Mice. *Journal of Clinical Oncology* 2009, **27**(15):2542-2552.

12. Yuan F, Dellian M, Fukumura D, Leunig M, Berk DA, Torchilin VP, Jain RK: **Vascular Permeability in a Human Tumor Xenograft: Molecular Size Dependence and Cutoff Size**. *Cancer Research* 1995, **55**(17):3752-3756.

13. Jain RK, di Tomaso E, Duda DG, Loeffler JS, Sorensen AG, Batchelor TT: **Angiogenesis in brain tumours**. *Nat Rev Neurosci* 2007, **8**(8):610-622.

14. Pallavicini MG, Summers LJ, Dean PN, Gray JW: **Enrichment of murine hemopoietic clonogenic cells by multivariate analyses and sorting**. *Exp Hematol* 1985, **13**:1173-1181.

15. Goodell MA, Brose K, Paradis G, Conner AS, Mulligan RC: **Isolation and functional properties of murine hematopoietic stem cells that are replicating in vivo**. *The Journal of Experimental Medicine* 1996, **183**(4):1797-1806.

16. Parmar K, Mauch P, Vergilio J-A, Sackstein R, Down JD: **Distribution of hematopoietic stem cells in the bone marrow according to regional hypoxia**. *Proceedings of the National Academy of Sciences* 2007, **104**(13):5431-5436.

17. Sakadzic S, Roussakis E, Yaseen MA, Mandeville ET, Srinivasan VJ, Arai K, Ruvinskaya S, Devor A, Lo EH, Vinogradov SA *et al*: **Two-photon high-resolution measurement of partial pressure of oxygen in cerebral vasculature and tissue**. *Nat Meth* 2010, **7**(9):755-759.

18. De Palma M, Mazzieri R, Politi LS, Pucci F, Zonari E, Sitia G, Mazzoleni S, Moi D, Venneri MA, Indraccolo S *et al*: **Tumor-Targeted Interferon-α Delivery by Tie2-Expressing Monocytes Inhibits Tumor Growth and Metastasis**. *Cancer Cell* 2008, **14**(4):299-311.

19. Mazo IB, Gutierrez-Ramos J-C, Frenette PS, Hynes RO, Wagner DD, von Andrian UH: **Hematopoietic Progenitor Cell Rolling in Bone Marrow Microvessels: Parallel Contributions by Endothelial Selectins and Vascular Cell Adhesion Molecule 1**. *The Journal of Experimental Medicine* 1998, **188**(3):465-474.

20. Tyrrell JA, di Tomaso E, Fuja D, Ricky T, Kozak K, Jain RK, Roysam B: **Robust 3-D Modeling of Vasculature Imagery Using Superellipsoids**. *Medical Imaging, IEEE Transactions on* 2007, **26**(2):223-237.

21. Wilson DF, Vanderkooi JM, Green TJ, Maniara G, DeFeo SP, D.C. B: **A versatile and sensitive method for measuring oxygen**. *Adv Exptl Med Biol* 1987, **215**(71-77).

22. Vanderkooi JM, Wilson DF: **A new method for measuring oxygen concentration in biological systems**. *Adv Exptl Med Biol* 1986, **200**:189-193.

23. Janssen BJA, De Celle T, Debets JJM, Brouns AE, Callahan MF, Smith TL: **Effects of anesthetics on systemic hemodynamics in mice**. *American Journal of Physiology - Heart and Circulatory Physiology* 2004, **287**(4):H1618-H1624.

Chapter 5. Synthesis of Compact and Biocompatible Quantum Dots with a Zwitterionic Polymer Coating

5.1 Background and Motivation

In this chapter, we present development of a new class of the QD ligands that incorporates betaine moieties to synthesize extremely compact and biocompatible QDs. Poly(ethylene glycol) (PEG) has been one of the most popular surface coatings for nanoparticles to make them water soluble and non-interactive with biomolecules or cells [1-5]. However, PEG coatings significantly increase the particles' hydrodynamic size because more than 8 units of ethylene glycol are required to enable water solubility of the particles. For instance, PEG coatings produce a hydrodynamic size of > 10nm for an inorganic core/shell of < 5 nm [3, 4]. The small hydrodynamic size of particles is crucial for their access to crowded cellular regions for biological studies [6, 7], efficient Förster Resonance Energy Transfer (FRET) [8], and renal clearance of the particles [9]. Therefore, the search for more compact ligands has been an issue in the field.

Recently, zwitterionic self-assembled monolayers (SAMs) have brought attention as a biocompatible surface. Due to the strong hydration capacity via electrostatic interactions, zwitterionic SAMs show very low nonspecific protein adsorption [10-12]. Small molecules containing zwitterionic moieties such as cysteine [13], D-penicillamine [14], mercaptoalkane-phosphorylcholine [15], or dihydrolipoic sulfobetaine ligands [16] have been used to prepare water soluble QDs or gold nanoparticles. However, those coatings suffer from weak binding of

monothiols to the nanoparticles and poor stability of the ligands in ambient conditions owing to the oxidation of thiols [4].

In this chapter, we demonstrate the development of betaine polyimidazole ligands (betaine PILs) incorporating pendant imidazole moieties for QD binding and sulfate betaine (SBPIL) or carboxybetaine (CBPIL) moieties for water-solubilization. Multi-dentate imidazole moieties provide strong binding of the ligand to the QD surface and prevent aggregation of QDs [4]. As a result, betaine PIL coated QDs were stable in buffer up to a month as opposed to several hours or a day for cyesteine. Also, permanent charges on sulfonate and quaternary amines of SBPIL allow us to synthesize QDs that are zwitterionic at all times as opposed to zwitterionic molecules containing carboxylic acids and amines whose surface charge depends on the pH of environments.

Synthesis of betaine PILs was developed by modifying the synthesis of recently developed PEG containing poly imidazole ligands (PEG PILs) [4], and the betaine PIL coated QDs (betaine PIL QDs) were prepared by exchanging the native ligand of QDs with betaine PILs. The resulting QDs were used for *in vitro* nonspecific cell binding studies, *in vivo* clearance studies, trans vascular flux measurements and biodistribution analysis to examine the behaviors of the betaine QDs in biological environments. In addition, QD-dye conjugates were built by incorporating derivatizable moieties in SBPILs. With extremely compact size of the betaine PIL QDs, efficient energy transfer was observed between QDs. In addition, characteristic behaviors of the betaine PIL QDs were compared with that of the PEG PIL QDs *in vitro* and *in vivo* to learn the influence of zwitterionic ligands on QD behaviors in bio-environments.

5.2 Synthesis and Characterization of Betaine PIL QDs

By incorporating multidentate imidazole moieties in the QD ligands, we were able to synthesize exceptionally stable zwitterionic QDs with shelf life of up to a month. As expected, the hydrodynamic diameter of the betaine PIL QDs was significantly smaller than that of the PEGPIL QDs.

5.2.1 Monomer Synthesis and Polymerization

The synthesis of betaine PILs is composed of three steps (Scheme **1**): (1) RAFT mediated polymerization of backbone (Polymer **3**), (2) betainization of the polymers (Polymer **4**, **6**) and (3) cleavage of BOC protecting groups (Polymer **5**, **7**). RAFT mediated polymerization allows us tight control over the mean and standard deviation of the resulting polymer weights, as shown in the previous literature (Figure 5-1A) [4]. Post-modification of a polymerized backbone to yield the betaine PILs was chosen as the pre-modified zwitterionic monomer exhibited very limited solubility in organic solvents.

To prepare the monomer, N-hydroxysuccinimide activated acrylic acid or acryloyl chloride was coupled to primary amine containing moieties (histamine and N,N-dimethyl diethane 1,2 diamine) and purified using silica column. The purified monomers were polymerized via RAFT mediated polymerization using dibenzyl carbonotrithioate as a RAFT reagent and Azobisisobutyronitrile (AIBN) as an initiator in dry DMF (Scheme 5-1). The resulting polymer (polymer **3**) was used for betainization without further purification. Before the betainization, the molecular weight and the polydispersity of the polymer samples were measured by gel permeation chromatography (GPC). As expected, narrow polydispersity and good control of molecular weight of the polymer 5 was confirmed (Figure 5-1A).

Scheme 5-1

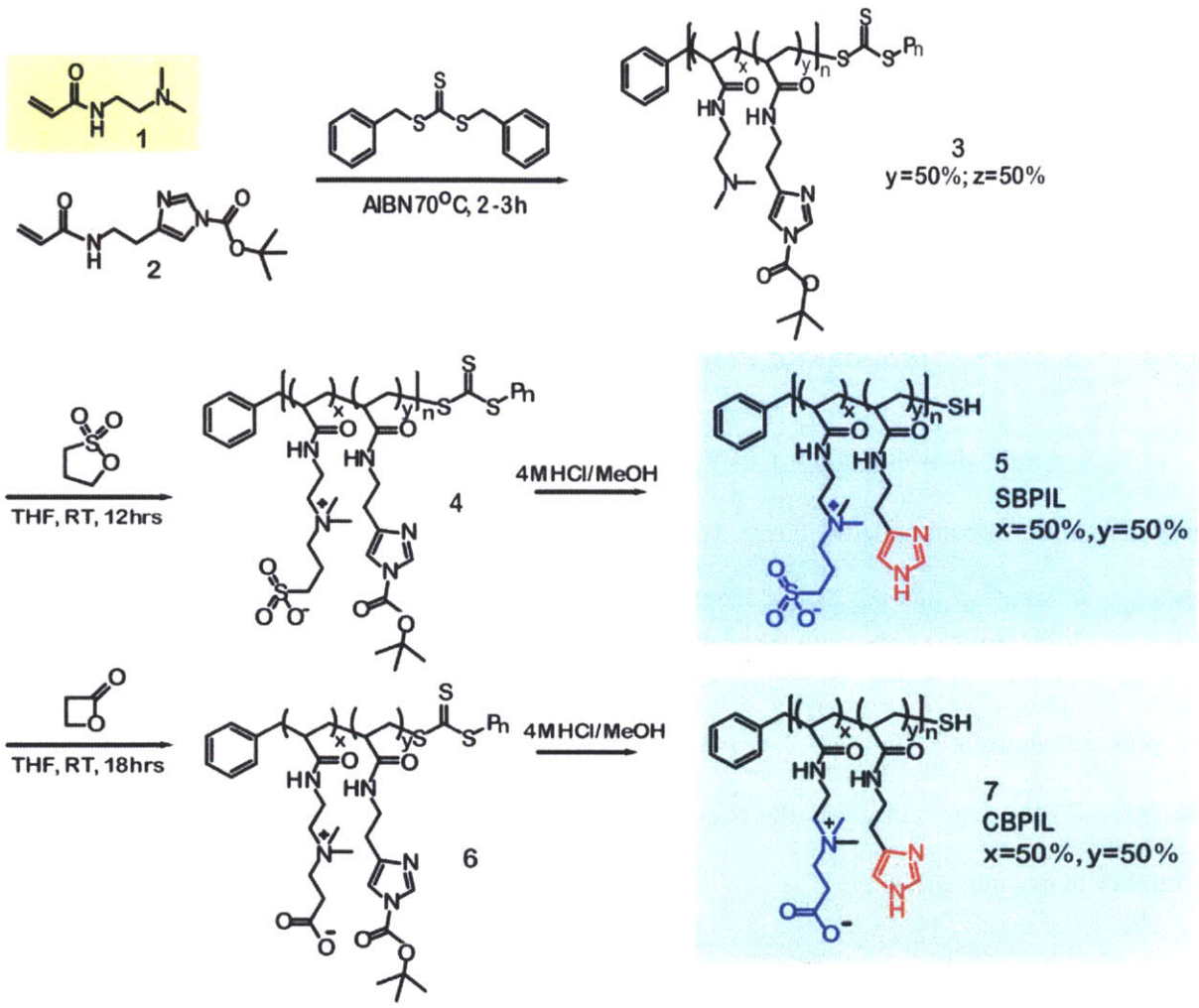

Scheme 5-2

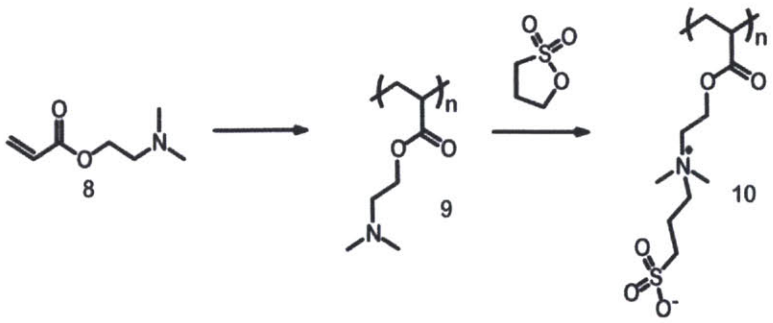

Scheme 5-3

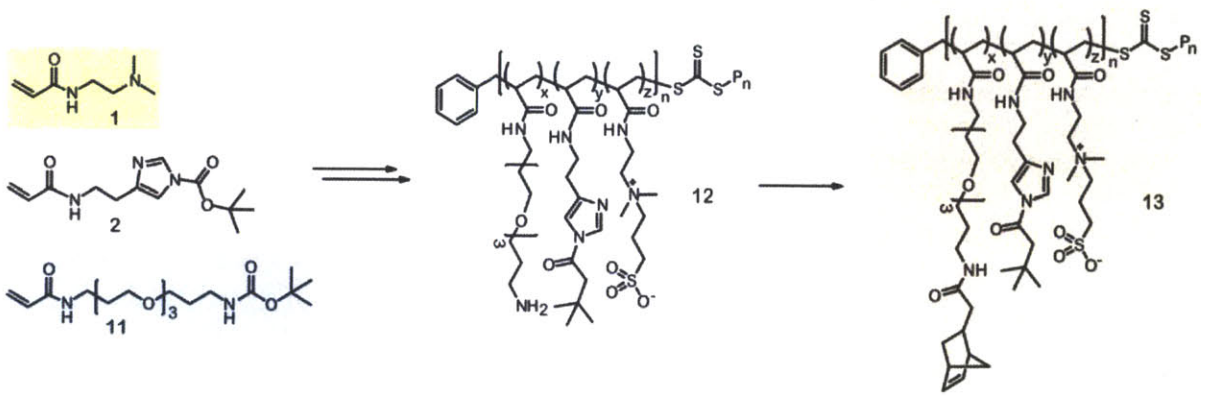

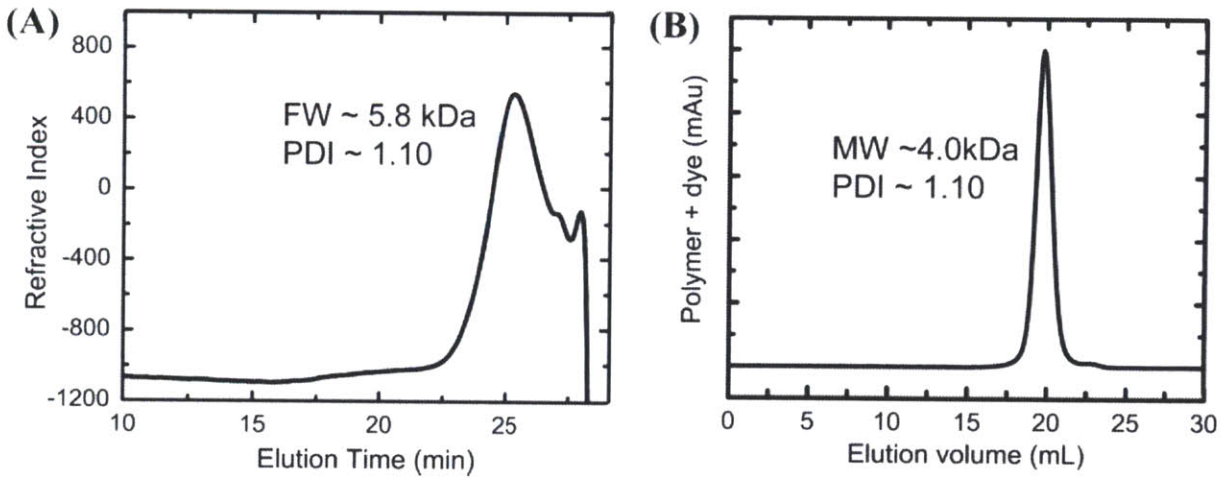

Figure 5-1. Characterization of (A) polymer 4 by gel permeation chromatography and (B) polymer 5 by gel filtration chromatography.

For betainization, highly strained 1,3-sultone and β-propiolactone were used. Release of ring strain allows one-step conversion of tertiary amine to quatanary amine and either sulfonate (sulfobetaine PIL (SBPIL), Polymer **5**) or carboxylate group (carboxybetaine PIL (CBPIL),

Polymer **7**). Before the betainization, compatibility of 1,3-sultone with BOC protected amines was verified by mixing 1,3-sultone with monomer 2 and monomer 8 and monitoring the NMR spectra since 1,3-sultone is known to form highly acidic solutions in the presence of water which in turn deprotect the BOC groups. The NMR spectra confirmed that the BOC groups on monomer 2 and 8 are intact after incubation with 1,3-sultone (Figure 5-2). For the betainization, 2-(dimethylamino)ethyl acrylate homopolymer (Scheme 5-2, polymer 9) was used as a model polymer to optimize the chemistry to achieve the conversion yield of close to unity. The conversion efficiency was measured by elemental analysis of the resulting betaine polymer (polymer **10** in Scheme 5-2, refer to Table 1 for the elemental analysis data done by Atlantic Micro Lab Inc.). The extent of the betainization measured by H NMR was not accurate since peak broadening of the polymers hinders accurate integration of each peak (Figure 5-3). Before the betainization, polymer 3 was soluble in a wide range of organic solvents such as chloroform, methanol, and dimethylformaide. However, after the betainization, the polymers were only soluble in aqueous solution or highly fluorinated organic solvents such as 2,2,2-trifluoroethanol and 1,1,1,3,3,3-hexafluoropropan-2ol. The size of the final polymers was measured using gel filtration chromatography (GFC) against protein standards (BioRad) (Figure 5-1B). The narrow molecular mass distribution of polymer **3** was preserved after the betainization, which indicates high conversion efficiencies of the tertiary amine moieties to betaines. The lower molecular weight of the final polymer (polymer **5**, **7**), which is calculated from the hydrodynamic size, compared to the polymer before betainization (polymer **3**) might be due to differences between the hydrodynamic volume of betaine PILs and the standard proteins (Vitamin B12, Myoglobin, Ovalbumin, and Gamma Globulin).

(A)

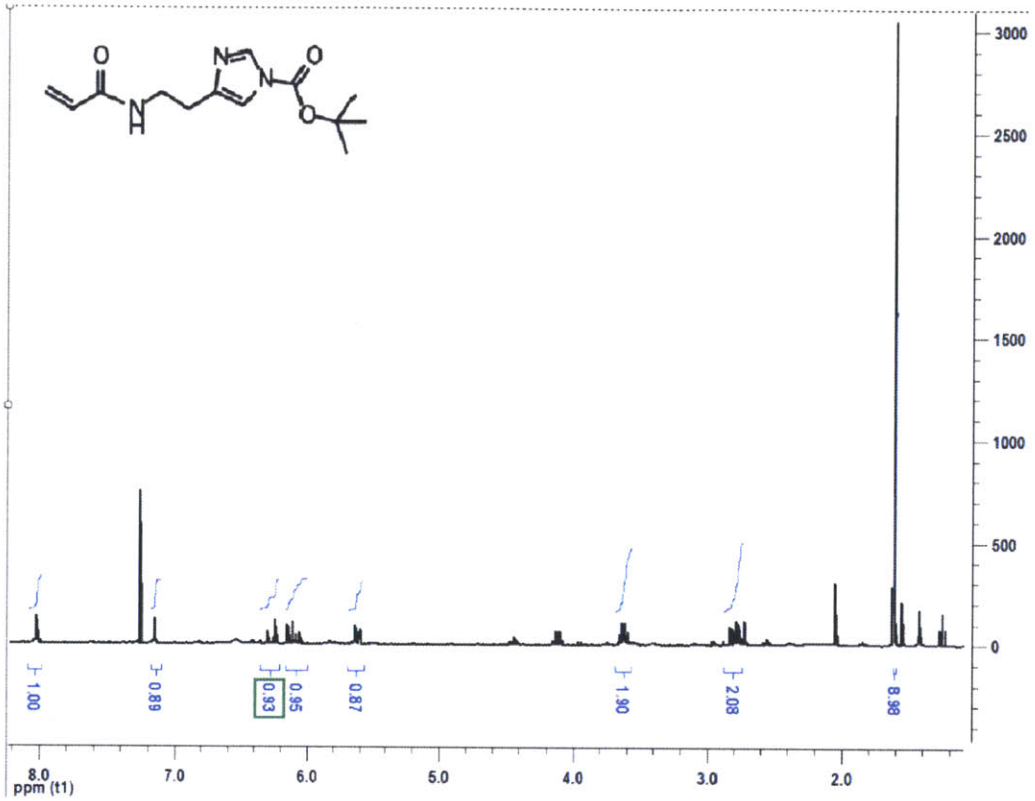
3000
2500
2000
1500
1000
500
0
1.00
0.89
0.93
0.95
0.87
1.90
2.08
8.99
8.0
ppm (t1)
7.0
6.0
5.0
4.0
3.0
2.0

(B)

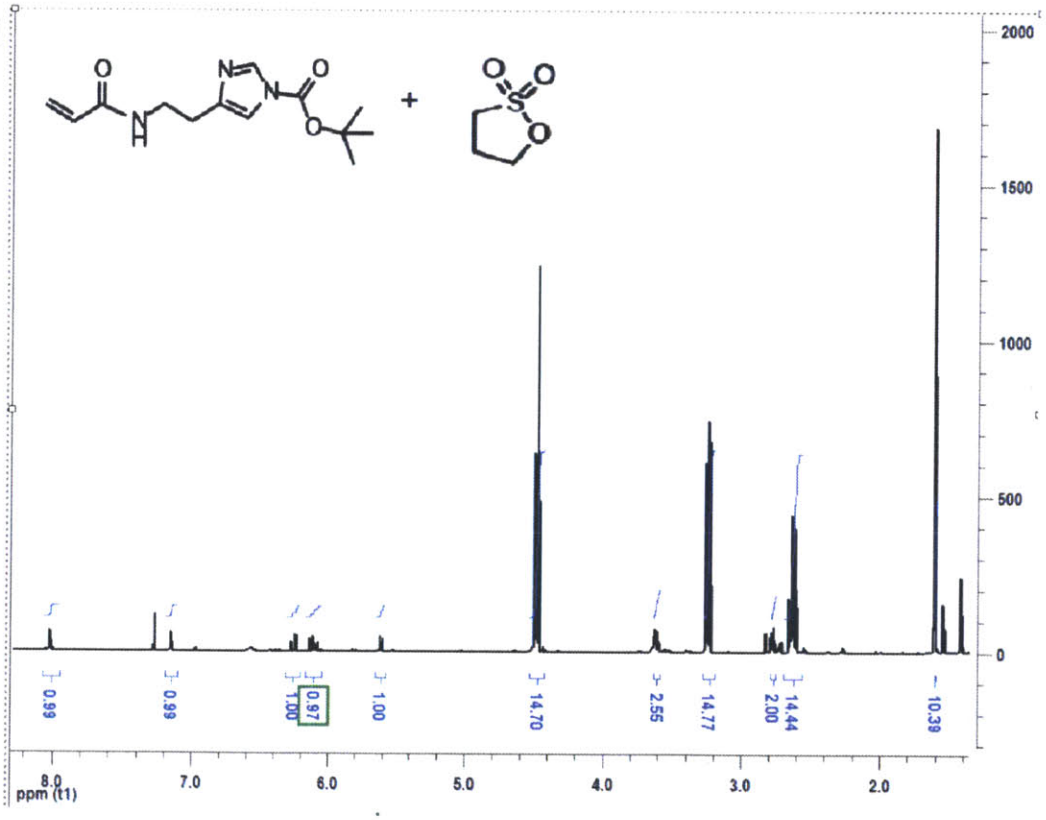
2000
1500
1000
500
0
0.99
0.99
1.00
0.97
1.00
14.70
2.55
14.77
2.00
14.44
10.39
8.0
ppm (t1)
7.0
6.0
5.0
4.0
3.0
2.0

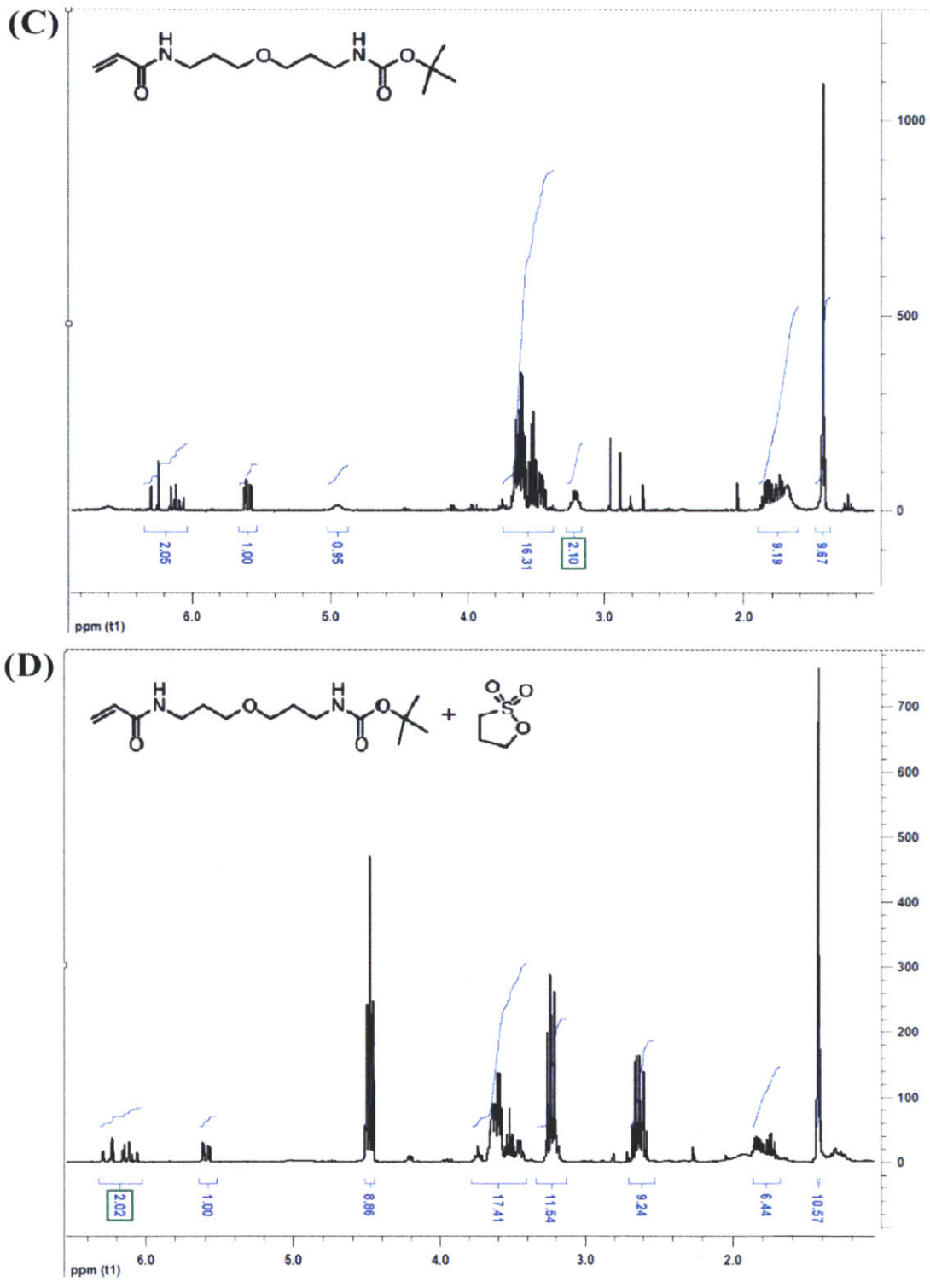

Figure 5-2 Compatibility of 1,3-sultone with BOC protected amine containing monomers. NMR spectra of (A) monomer 2, (B) monomer 2 mixed with 5 times excess of 1,3-sultone, (C) monomer 8, and (D) monomer 8 mixed with 5 times excess of 1,3-sultone.

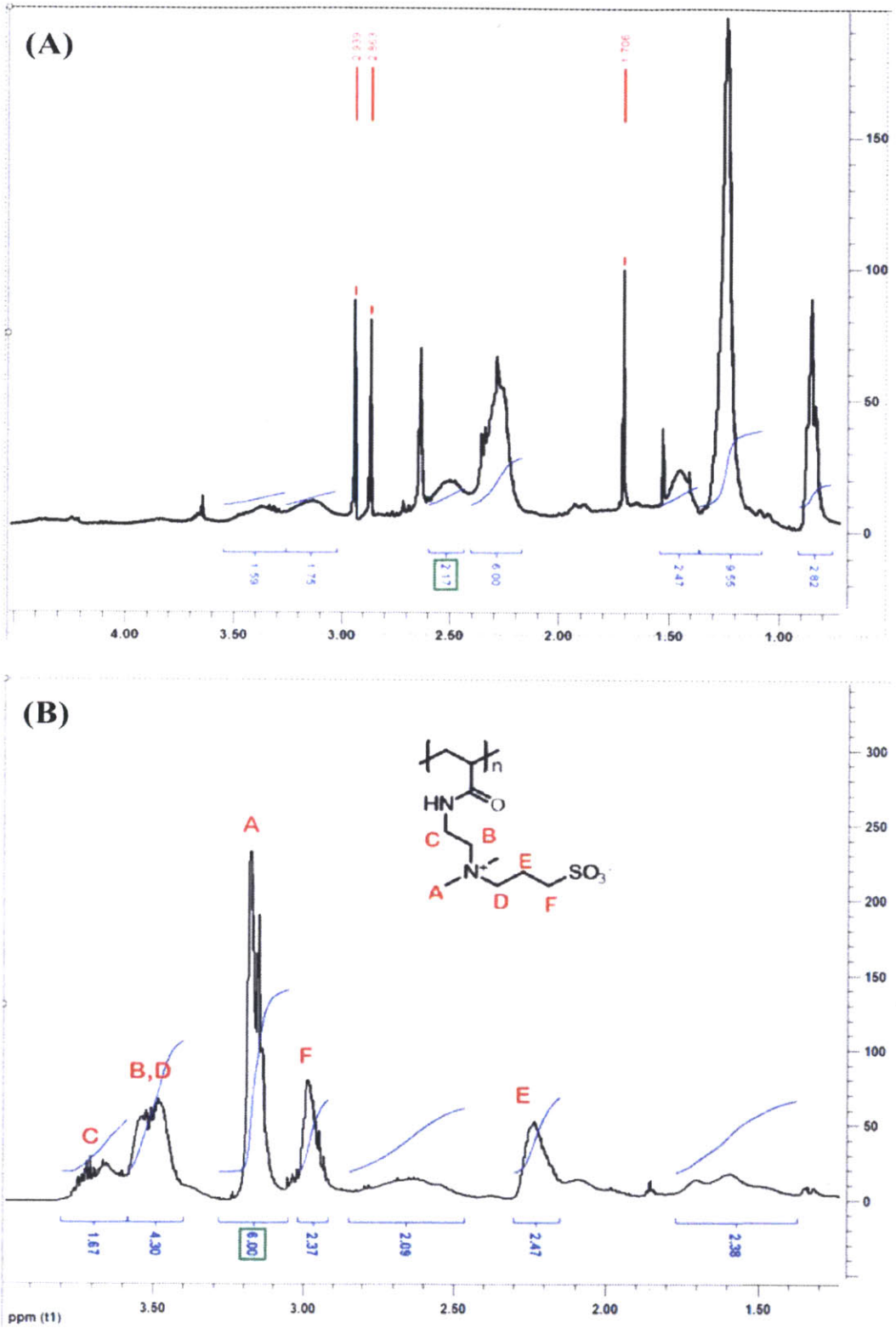

Figure 5-3 NMR spectra of (A) the tertiary amine homopolymer, polymer 9 in scheme 2 and (B) the betaine homopolymer, polymer 10 in scheme 2.

5.2.2 Preparation of Betaine PIL QDs

Water soluble QDs coated with the betaine PIL were prepared by ligand exchange of the native hydrophobic ligand capped QDs with the betaine polymers. InAs($Cd_xZn_{1-x}S$) emitting at 800 nm, CdSe(CdS) emitting at 570 nm and CdSe(CdZnS) emitting at 605 nm were successfully brought into water by exchanging their native ligands with SBPILs and CBPILs. This experiment confirms that the betaine polymers can be used for water solubilization of various type of QDs ranging from visible to near infrared. The ligand exchange was achieved using a modified biphasic exchange method. In a typical biphasic exchange, QDs are dissolved in a hydrophobic solvent such as chloroform and stirred with the water layer containing water-soluble ligands [13]. However, this method requires a concentrated solution of ligands and does not work for polymeric ligands with multidentate binding units; This is because simultaneous coordination of binding units is difficult to achieve at the interface of hydrophobic and hydrophilic solvents. Therefore, we first performed partial ligand exchange by adding the betaine polymer solution dissolved in 2,2,2-trifluoroethanol, and then performed biphasic ligand exchange. While adding the polymer solution, the QD solution becomes turbid due to low solubility of the QDs in 2,2,2-trifluoroethanol. The resulting QD solution was not soluble either in chloroform or in water, which indicates partial exchange of the native ligands. After that, chloroform and water were added to the QD solution and the whole solution was stirred vigorously. Within 1 minute, QDs were transferred to the water phase leaving the chloroform phase transparent (Figure 5-4). This result can be explained by the increased solubility of QDs in aqueous solution after the partial ligand exchange, which in turn promotes the complete exchange of the native ligands with the betaine PILs via biphasic ligand exchange.

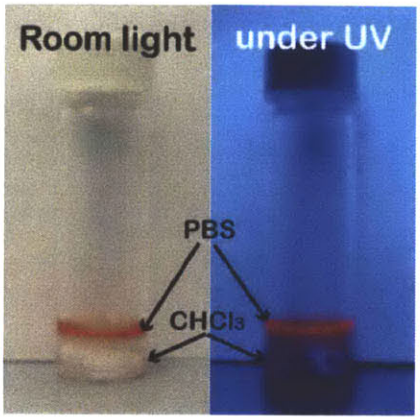

Figure 5-4 Modified biphasic ligand exchange. After the exchange, the SBPIL QDs were well dispersed in aqueous solutions. Left panel shows the picture taken under the room light and right panel shows the picture take under UV illumination.

5.2.3 Characterization of the Betaine PIL QDs

After the ligand exchange, both SBPIL QDs and CBPIL QDs were well dispersed in aqueous buffers with pH ranging from 5 to 12. Transmission electron microscopy (TEM) images confirmed that both CBPIL and SBPIL QDs are monodisperse without forming aggregates (Figure 5-5). Both QD solutions were stable in buffers for over a month under ambient conditions, which is a great enhancement from the zwitterionic ligand coated QDs presented in previous literature that have shelf lives of several hours to a day at the most (data not shown).

After ligand exchange, a slight red shift of the emission peak (2-3 nm) of the betaine PIL QDs was observed but the full width half max of the emission features remained fairly constant. Absorbance and emission spectra of CdSe(CdS) before and after the ligand exchange with the SBPILs are shown in Figure 5-6A. The quantum yield (QY) of CdSe/CdS coated with the betaine PIL was ~65%, a modest drop from a QY of >90% in n-octane with native ligands. The PEG PIL QDs showed slightly higher QY (~80 %) than betaine PIL QDs (~65%). This may be

due to better passivation of the QD surface with the PEG PILs than betaine PILs owing to the long repeating units of ethylene glycol. In addition, photo-brightening of the betaine PIL QDs after UV treatment was observed as reported previously for the PEG PIL QDs [4].

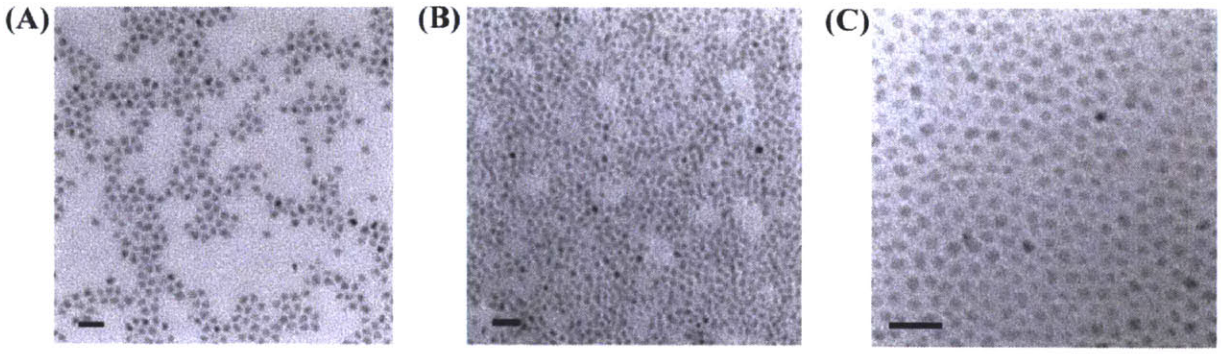

Figure 5-5 TEM images of (A) QD_{612} in hexane, (B) CBPIL QD_{612}, and (C) SBPIL QD_{612}.

The hydrodynamic size of the SBPIL QDs, which was measured with both GFC and dynamic light scattering (DLS), was significantly smaller (~7nm) than that of the PEG PIL QDs (~ 11nm) (Figure 5-6B). GFC traces were taken only for the SBPIL QDs as the CBPIL QDs showed strong interaction with the GFC media which prevented the elution of the particles. However, DLS data showed the hydrodynamic size of the CBPIL QDs is very similar to that of the SBPIL QDs (Figure 5-6B). The small size of the QD constructs is beneficial for sensing applications based on energy transfer and for the access of the QD constructs to biologically crowded regions such as neuronal synapses or solid tumors. In addition, *in vivo* studies have shown that the small size promotes rapid clearance of QDs via urinary excretion as intact nanoparticles, and minimizes the toxicity of QDs in live animals [9].

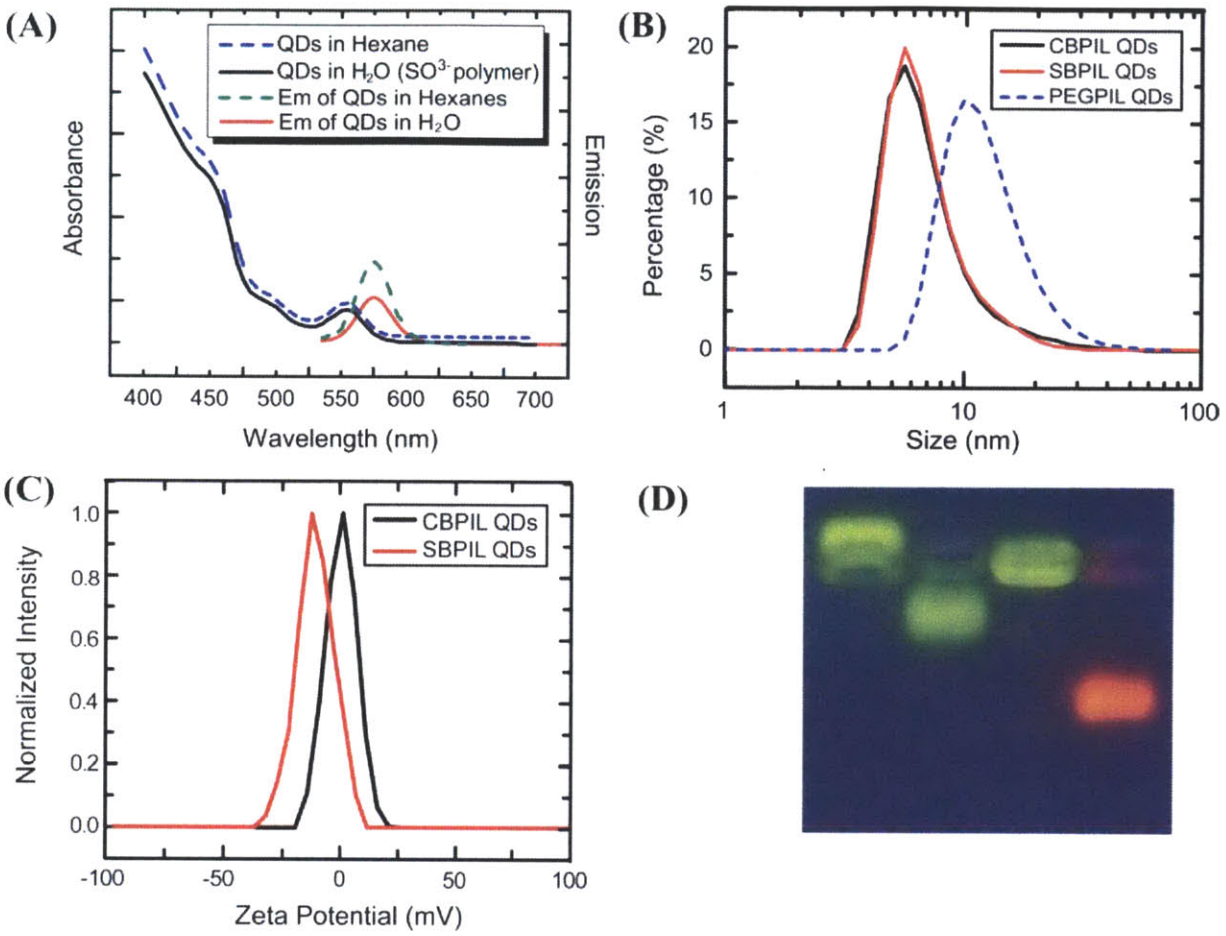

Figure 5-6 Characterization of the betaine PILs QDs (A) Absorption (sold black and dashed blue) and Emission (solid red and dashed green) spectra of QDs before (dashed) and after (solid) ligand exchange with SBPILs. (B) Dynamic scattering data of SBPIL QDs, CBPIL QDs and PEGPIL QDs. (C) Zeta potential measurements for the SBPIL and CBPIL QDs (D) Gel electrophoresis of the PEGPIL QDs (first lane), SBPIL QDs (second lane), CBPIL QDs (third lane) and DHLA QDs (fourth lane).

The surface charges of SBPIL coated QDs and CBPILs coated QDs were characterized by measuring the zeta potential and performing gel electrophoresis. The zeta potential of the CBPIL QDs was ~ 0.3mV (close to neutral) and that of the SBPIL QDs was ~ -13.1mV (mildly negatively charged) (Figure 5-6C). This data is consistent with gel electrophoresis results where CBPIL QDs did not move when applying the voltage, while SBPIL QDs moved slightly towards

the positive electrode (Figure 5-6D). The PEG PIL QDs, which are almost neutral, and dihydrolipoic acid (DHLA) coated QDs, which are highly negatively charged, were run with the betaine PIL QDs as a reference. The negative surface charge of the SBPIL QDs despite the zwitteronic nature of the SBPILs can be explained by the association of negative ions present in buffers with the quaternary amines in the SBPILs. The quaternary amines and the carboxylate groups of the SBPILs are separated by three carbons, which provide an enough space for a negative ion to be associated with the amine. In contrast, the quaternary amines and the carboxylate groups of the CBPILs are separated by only two carbons. Due to the proximity of the negative and the positive groups, hydration shells around two groups generate more spatially uniform and stronger hydration layer, which result in the neutral surface charge of the CBPIL QDs [12].

5.2.4 Non-biocompatible Behaviors of the CBPIL QDs

Even though both CBPILs and SBPILs were successful at solubilizing QDs in aqueous buffers, CBPIL QDs exhibited strong interaction with sugar-based polymeric beads such as sephadex, superdex, and superose, and also showed high nonspecific binding towards cells. This observation contradicts what has been reported previously. Several papers reported that self-assemble monolayers displaying carboxybetaine moieties exhibit extremely low nonspecific binding properties [12, 17-20]. This discrepancy can be explained by the usage of different substrates. Most of the previous experiments were executed on gold surfaces with carboxybetaine ligands possessing thiols as a coordinating group. In this case, the binding constant between thiol and gold is far greater than the binding constant between carboxylate and gold[21-23], and all carboxylate groups are exposed to the environment rather than binding to

the gold surface. But in case of the CBPIL QDs, the binding energy of carboxylic acids with the QD surface is similar to that of amines [24]. Therefore, in case of the CBPIL QDs, we expect both carboxylic acids and imidazole moieties to bind to the QD surface. Attraction of carboxylate groups towards the QD surface has been confirmed by low conjugation efficiencies of the carboxylic groups on the QDs [4, 25]. For the CBPIL QDs, binding of carboxylic acid to the QD surface will result in the exposure of positively charged quaternary amines to the outermost layer of the QDs. The exposed quaternary amine groups of the CBPILs can trigger nonspecific interaction of the CBPIL QDs with cells and the polymer beads. In contrast, the sulfonate groups of the SBPILs do not interact with the QD surface and allow the entire sulfobetaine moieties of the SBPIL QDs to face outward. With the limited biocompatibility of the CBPIL QDs, we used only SBPIL QDs for *in vitro* and *in vivo* studies.

5.3 Functionalization of SBPIL QDs and Conjugation of Bio-Molecules

5.3.1 Conjugation to an Organic Dye for Förster Resonance Energy Transfer

To provide the derivatizability to the SBPIL ligands, we incorporated 10% of amino-PEG_3 acrylamide to the SBPILs (polymer **12**) and modified the primary amine groups with norbornene to yield norbornene containing SBPILs ($NB_{10\%}$-SBPILs, polymer **13**, Scheme 5-3). Amine groups were converted to norbornene groups since the positive charge of amine groups in the PIL ligands increases the nonspecific binding of the PIL QDs to cells and proteins [3, 4]. After the ligand preparations, NB-SBPIL QDs were prepared by the ligands exchange process as described earlier. To conjugate organic dyes to $NB_{10\%}$-SBPIL QDs, norbornene modified QDs were mixed with tetrazine modified Alexa594. Sixteen hours after the incubation of $NB_{10\%}$-

SBPIL QDs with tetrazine modified Alexa594, unreacted dyes and byproducts were purified with GFC and spin concentrator with molecular weight cut off (MWCO) of 50 kDa. Refer to the method section for more detailed synthesis.

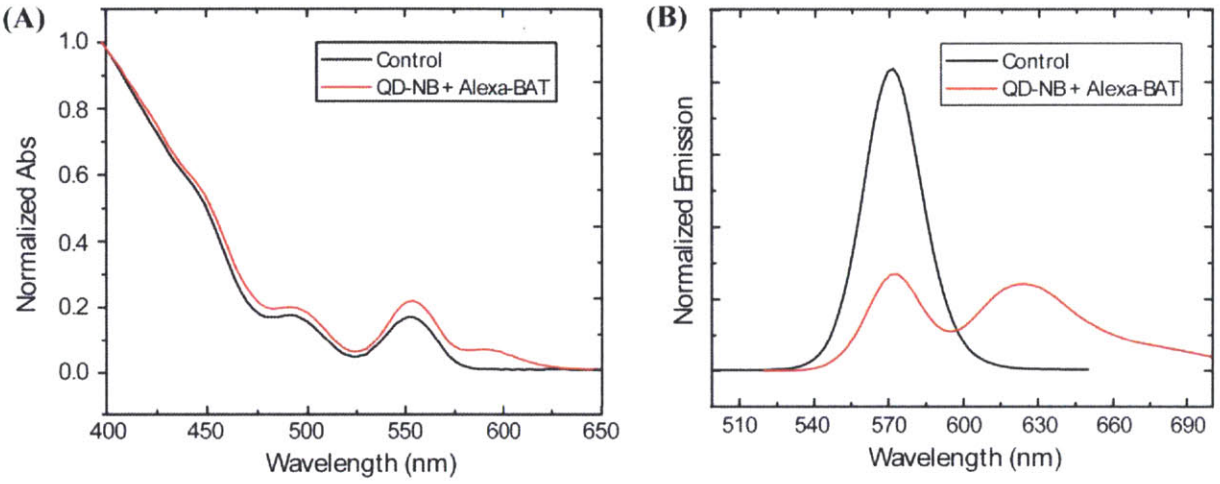

Figure 5-7 (A) Absorbance and (B) emission spectra of the QD-Alexa594. The conjugation was achieved by mixing tetrazine modified Alexa594 (Alexa-BAT) with norbornene modified SBPIL QDs and purified unreacted Alexa594 using GFC and spin concentrators.

Absorbance spectra of the QD samples after the conjugation exhibit both features from the dye and the QDs which confirms successful coupling of the dyes to QDs (Figure 5-7). Figure 4B shows the emission spectrum of the conjugates under 400nm excitation where the dye has minimal absorbance. Under this circumstance, only QDs are excited by the direct excitations and the dyes can be excited through Förster Resonance Energy Transfer (FRET) from the QDs. As expected, the QD emission was significantly quenched compared to the control QDs processed similarly but without the dyes, while the dye emission was enhanced more than 70 times compared to the free dyes of the same concentration which were excited at 400nm. The emission spectra show that we were able to achieve efficient FRET from QD to the dye even with the

small number of dyes conjugated per QD (~1.4 dye/QD) owing to exceptionally small hydrodynamic diameter of the SBPIL QDs.

5.4 *In vitro* Experiments Using SBPIL QDs

5.4.1 Nonspecific Binding to HeLa Cells

To evaluate the suitability of SBPIL QDs as bio-imaging probes, nonspecific adsorption of the SBPIL QDs to cells was investigated by incubating the SBPIL QDs with HeLa cells and subsequently washing the cells four times with phosphate buffered saline (PBS). The cell experiments showed dramatic difference in nonspecific cell binding depending on the betainization efficiencies of the SBPILs (Table 5-1).

Table 5-1 SBPIL samples that were synthesized with different ratios of the tertiary amines to 1,3-sultone for betainization and the properties of the QDs coated with each SBPIL sample.

	SBPIL sample 1 3^{o} amine : sultone = 1 : 1.2	**SBPIL sample 2** 3^{o} amine : Sulton = 1 : 3	**SBPIL sample 3** 3^{o}amine : Sulton = 1 : 5
Elemental analysis (S to N Ratio)	2.424 (82.5% conversion)	----	1.919 (104.2% conversion)
Nonspecific binding to cells	Significant binding	Less binding than sample 1	No binding
Zeta Potential	-0.4mV	-10.3mV	-13.1 mV

As shown in Figure 5-8, Cells incubated with QDs coated with SBPIL sample 1, the polymer with 80% conversion of tertiary amines to sulfobetaines, exhibited significant increase of fluorescence signal indicating nonspecific binding of the QDs to cells. On the other hands, the cells incubated with QDs coated with SBPIL sample 3, the polymer with 100% conversion of the tertiary amines to sulfobetaines, showed minimal increase of fluorescence signal. This result

confirms that even a small number of positively charged amines induces high nonspecific interaction of the particles with cells. After we confirmed that 100% conversion of the tertiary amines to sulfobetaines is crucial to prepare SBPIL QDs with minimal nonspecific adsorption to cells, we compared nonspecific binding of the SBPIL QDs with that of the PEGPIL QDs to understand the influence of the betaine moieties to the biocompatibility of the particles *in vitro*. At the concentrations of 50nM or lower, both the SBPIL QDs and the PEGPIL QDs showed nearly no binding (Figure 5-9). However, when the cells were incubated with the SBPIL QDs at the concentrations above 100nM, the SBPIL QDs exhibited slightly higher nonspecific adsorption to the cells than the PEGPIL QDs of the same concentration. This result is likely due to better passivation of the QD surface with PEG that has long repeating units of ethylene glycol ($n > 11$). We expect that long and flexible PEG chains physically protect the QD surface, and prevent proteins or bio-compartments from being adsorbed.

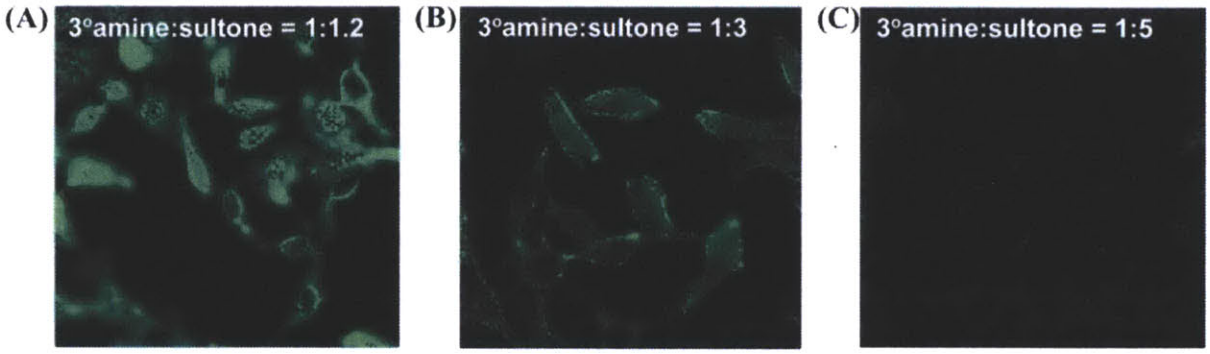

Figure 5-8 Nonspecific binding of the SBPIL QDs on HeLa cells with incubation at 100 nM QD concentration for 5 minutes at 4 °C, followed by 4 times wash with PBS buffer before imaging. (A) QDs coated with SBPIL sample 1, (B) QDs coated with SBPIL sample 2, and (C) QDs coated with SBPIL sample3. Significant decrease of the nonspecific binding was observed as the betainization efficiencies increases from 80% to 100%.

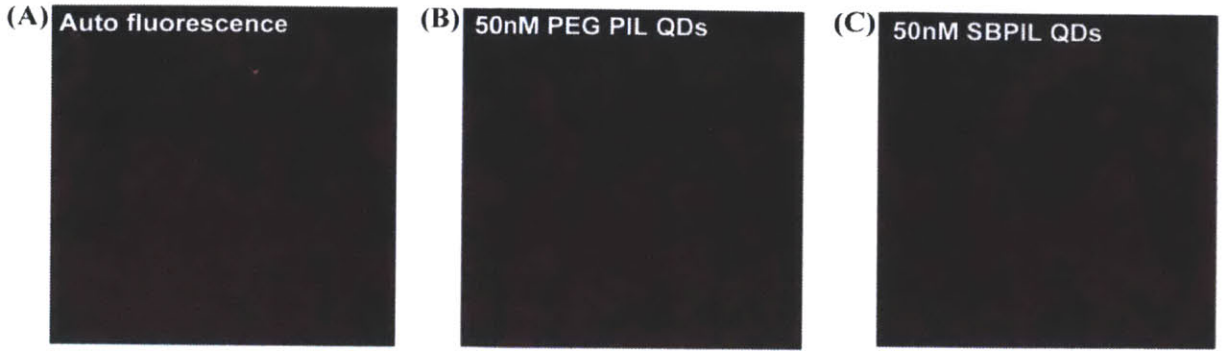

Figure 5-9 Nonspecific cell binding test with (B) 50nM of the PEGPIL QDs and (C) the SBPIL QDs. Both (B) and (C) showed the similar fluorescence level as the auto fluorescence of the cells (A).

5.5 *In vivo* Experiments Using SBPIL QDs

5.5.1 Nonspecific Binding to Serum Proteins for *In vivo* Applications

Since betaine SAMs, betaine polymer coated silica particles and gold nanoparticles have shown very low nonspecific adsorption of proteins in the previous studies [10-12, 18], we expect betaine PIL QDs to display very low bio-fouling properties. To illustrate the stability of the QDs for *in vivo* experiments, we incubated the SBPIL QDs with different concentrations of fetal bovine serum (FBS) (0.2×, 0.5× and 0.95× FBS) for 4 hours at 37°C, and verified the size change of the QDs before and after the incubation using size exclusion chromatography with fluorescence detection. The QDs incubated with PBS were used as the control. GFC traces show that the peak position of the SBPIL QDs did not change after serum incubation which indicates negligible nonspecific protein adsorption (Figure 5-10). However, we observed the growth of a small peak on the left shoulder of the elution spectra as we increased the concentration of FBS. This suggests that nonspecific binding does scale with protein concentration. Notwithstanding, the SBPIL QDs are still promising probes for *in vivo* imaging since they have extremely low protein adsorption properties when incubated with 50% FBS. Considering that blood is

composed of 50% serum and 50% blood cells, we expect the SBPIL QDs to be biocompatible *in vivo*.

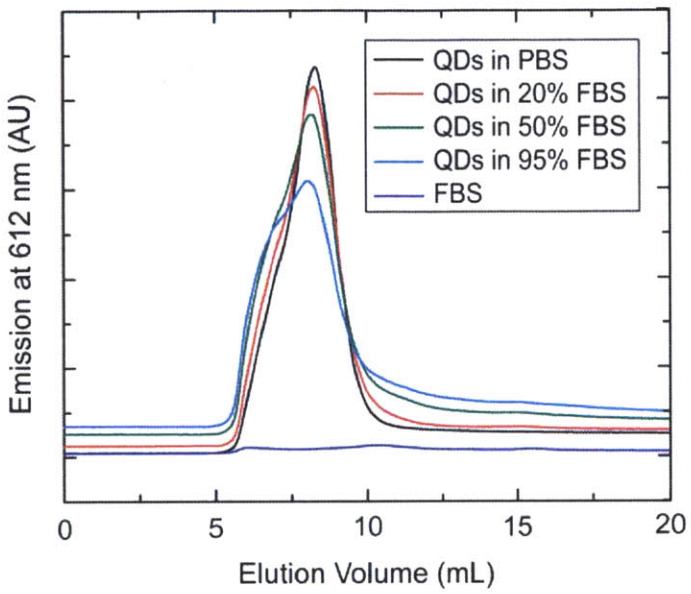

Figure 5-10 Nonspecific binding of QDs with serum proteins after incubation 20% (red), 50% (green), and 95% (blue) fetal bovine serum for 4 hours at 37 °C. QDs in PBS (black) and 100% FBS were run as a control.

5.5.2 *In vivo* Behaviors of SBPIL QDs

With low nonspecific serum binding, greatly enhanced stability and exceptionally compact size, the SBPIL QDs are expected to be excellent probes for *in vivo* imaging. To study the behaviors of the SBPIL QDs *in vivo*, we have carried out clearance studies, transvascular flux measurements and biodistribution studies. First, we examined clearance behavior of the SBPIL QDs *in vivo* by injecting 1nmol of SBPIL QDs (100uL of 10nM QD solution) via retro-orbital route in live mice and imaged vessels over time. As seen in Figure 5-11, we observed that the SBPIL QDs cleared from the vessels without leaving any evidence of nonspecific accumulation

of the QDs. This result was consistent among different core/shell QDs ranging from visible to near infrared (CdSe/ZnS, CdSe/CdZnS, CdSe/CdS, and InAs/CdZnS) (data not shown).

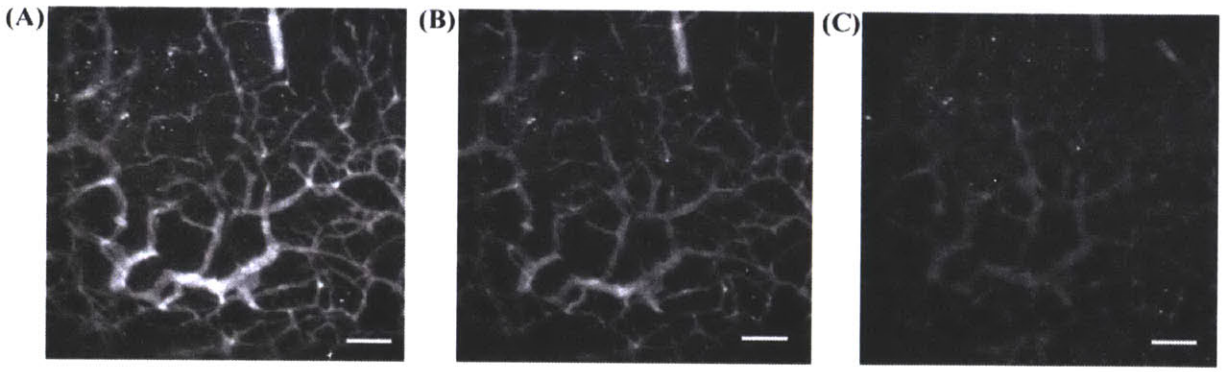

Figure 5-11 Clearance of the SBPIL QD_{612} from the vessels. The vessels were imaged through a mammary fat pad window at (A) 15 minutes, (B) 60 minutes, and (C) 4 hours after the injection. Note that SBPIL QD_{612} clears from the vessels without leaving any evidence of nonspecific accumulation. Scale bar = 100 μm.

After confirming that the SBPIL QDs showed virtually no nonspecific binding *in vivo*, clearance kinetics of SBPIL QDs versus PEGPIL QDs were compared to verify the effect of the betaine moieties on *in vivo* behavior of the QDs. For comparison, PEGPIL QD_{570} and SBPIL QD_{612} were coinjected into live mice and their clearance from vessels was imaged at multiple time points. PEGPIL QD_{570} and SBPIL QD_{612} have similar hydrodynamic sizes (~10nm, Figure 5-12), therefore, we were able to eliminate the effect of the size difference on their characteristic *in vivo* behaviors. Even though they have similar hydrodynamic diameters and similar zeta potentials (-7.7 mV for PEGPIL QD_{570}, -13.1mV for SBPIL QD_{612}), they showed very different clearance behaviors. Surprisingly, the SBPIL QD_{612} cleared much more quickly than the PEGPIL QD_{570} as shown in Figure 8 and Figure 5-13A. We confirmed that this result is solely due to the difference in the coatings and not due to the variability of the core QDs by comparing the clearance behavior of SBPIL QDs versus PEGPIL QDs that were prepared with the same core;

QD_{750} (InAs/CdZnS, Figure 5-13B). Higher level of nonspecific serum binding of the SBPIL QDs compared to the PEGPIL QDs might cause much more rapid clearance of the SBPIL QDs.

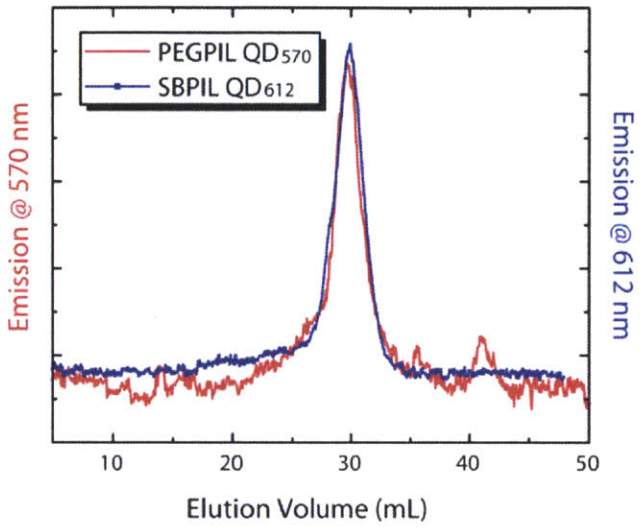

Figure 5-12 GFC traces of PEGPIL QD_{570} and SBPIL QD_{612}.

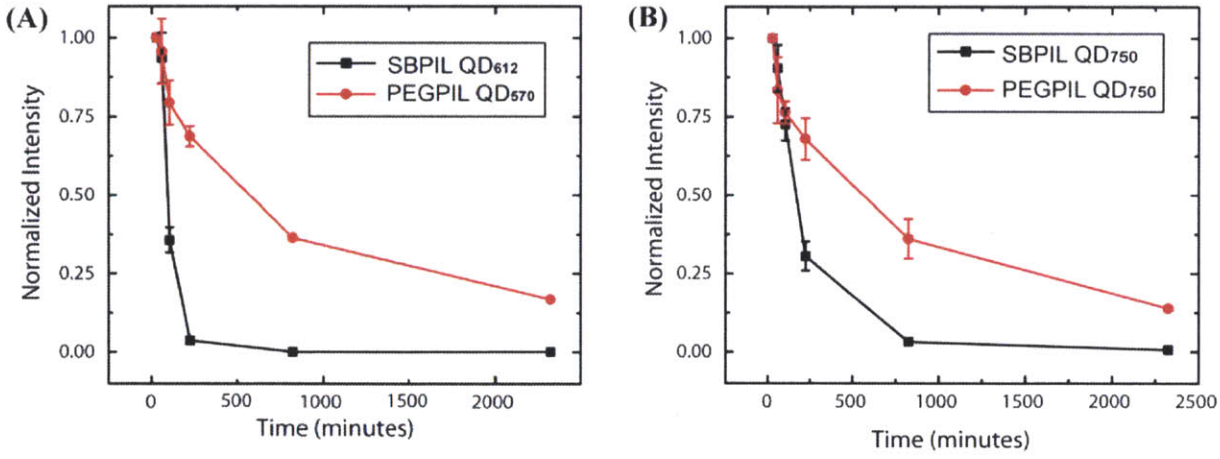

Figure 5-13 Comparison of clearance kinetic of SBPIL QDs versus PEGPIL QDs. (A) Clearance kinetic of SBPIL QD_{612} and PEGPIL QD_{570}, which have very similar hydrodynamic diameters. (B) Clearance kinetic of SBPIL QD_{750} and PEGPIL QD_{750} that were synthesized with the same QD cores.

After the clearance study, we measured the transvascular flux of the SBPIL QDs, a measure of how fast QDs extravasate from vessels. Transvascular flux of the QDs was measured in two different types of breast tumor which have different pore sizes; E0771 and MCaIV. MCaIV has exceptionally larger pores than other tumors (pore cutoff size of 1.2 to 2 μm while most tumors show pore cutoff size of 380 to 780 nm) [26, 27]. For this study, we injected SBPIL QD_{612} into mice bearing the tumors and measured the level of QD signal outside the vessels over time.

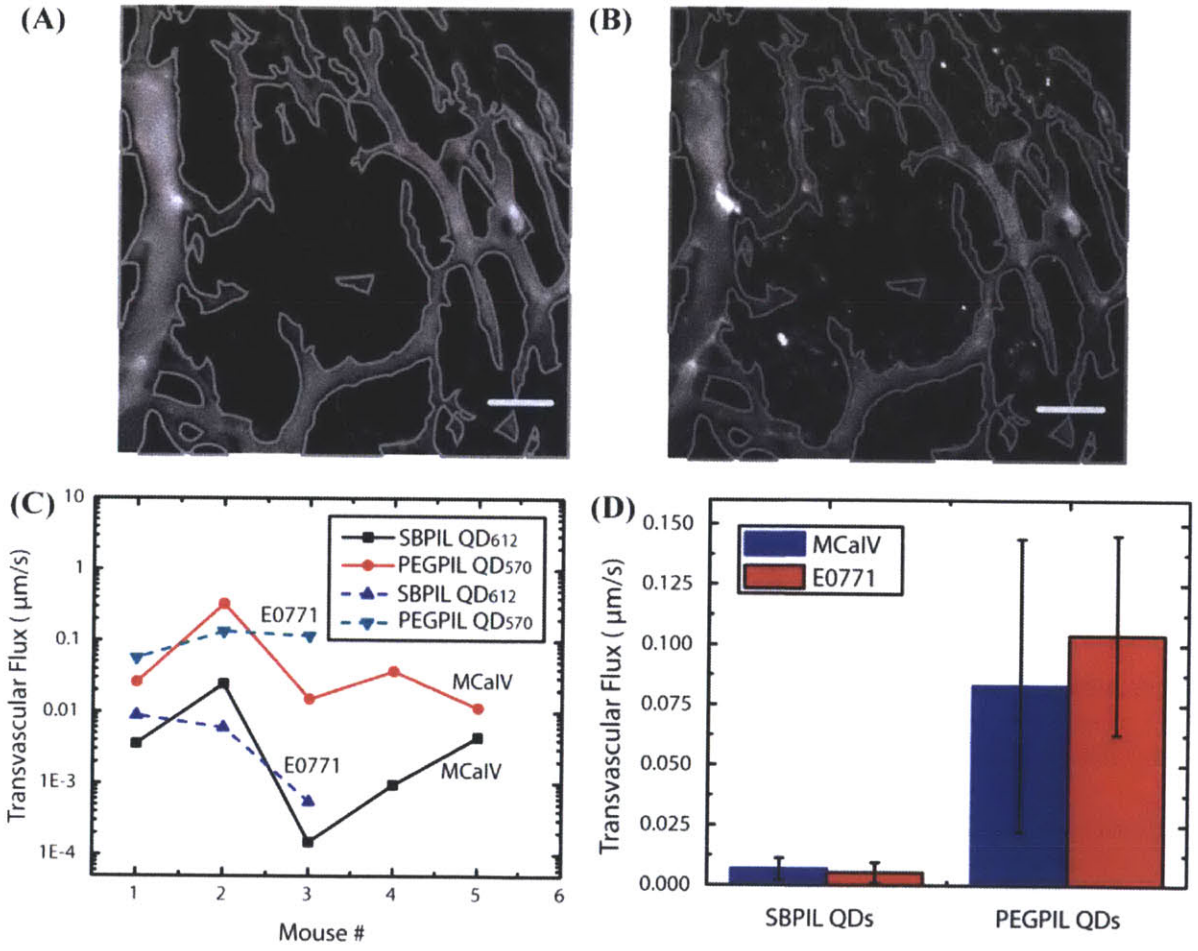

Figure 5-14 (A-B) Real-time intravital microscopy of ligand-dependent nanoparticle distribution in a murine breast tumor. Intravenous injection into a SCID mouse bearing an E0771 murine mammary adenocarcinoma in a mammary fat pad chamber of a mixture of (A) SBPIL QD_{612} and

(B)PEGPIL QD_{570}. Angiographic images demonstrate distribution of the nanoparticles one hour after injection. The initial fluorescence was recorded shortly after injection, and is depicted as the gray line. Images are mean intensity projections of 3D volumes. Scale bar is 100 μm. (C-D) Transvascular flux of SBPIL QD_{570} and PEGPIL QD_{612} in mice bearing an E0771 murine mammary adenocarcinoma and a MCaIV breast mammary cancer. (C) illustrates transvascular flux measured in individual mice. Solid lines are the values obtained from the mice bearing MCaIV tumor and dashed lines are the values obtained from the mice bearing E0771 tumor. (D) illustrates the average transvascular flux and the standard deviation.

Transvascular flux was calculated using the equation presented in the previous paper [28]. In both tumor models, the SBPIL QD_{612} showed 1 order of magnitude less transvascular flux than that of the PEGPIL QD_{570} (Figure 5-14). The difference of the transvascular flux between the SBPIL QDs and the PEGPIL QDs was less significant for the MCaIV tumor model which has larger pores. The significantly low transvascular flux of the SBPIL QDs can be explained by the reduced circulation half-life and weak negative charge of the SBPIL QDs. As shown in Figure 5-13A, only 35% of SBPIL QDs were present in the vessels 105 minutes after the injection while 76% of PEGPIL QDs remained in the vessels at the same time point. Due the reduction of the circulation time, the SBPIL QDs are thought not to have enough time to leave the vessels and enter the vicinity tissues. Also, the negative charge of the SBPIL QDs can cause repelling of the QDs from endothelial cells, which are known to display negative charges on the surface, which in turn hinder extravasation of the QDs [29, 30]. With low transvascular flux, SBPIL QDs will be useful for tracing vasculature more effectively than PEG displaying QDs because they do not leave the vasculature or raise the background signal.

Lastly, we performed *in vivo* biodistribution studies to unravel the cause of the fast clearance of SBPIL QDs. To investigate the biodistribution and tumor accumulation of the SBPIL QDs, the amount of cadmium delivered to various organs was measured using inductively

coupled plasma mass spectroscopy (ICP-MS) 24 hours after the SBPIL QD_{612} injection. To prepare the organ samples for the measurements, organs were collected from mice, physically homogenized using a homogenizer and boiled in concentrated nitric acid at 120°C for three days. After 3 days, all the organs were completely dissolved and the solutions became transparent. Then, the concentrated nitric acid was evaporated and 2% nitric acid with 1ppb In was added to produce the final organ samples for the measurements. To calculate the amount of cadmium delivered to each organ, we first generated the calibration curve using a series of cadmium solutions of known concentrations. After that, net increase of the cadmium level was obtained by subtracting the cadmium level, which is reported as counts, of the control mice from that of the QD injected mice. The net counts were then converted into cadmium concentrations by fitting them on the calibration curve. As seen in Figure 5-15, ~70% of SBPIL QDs were cleared through liver and spleen which implies RES clearance of the particles.

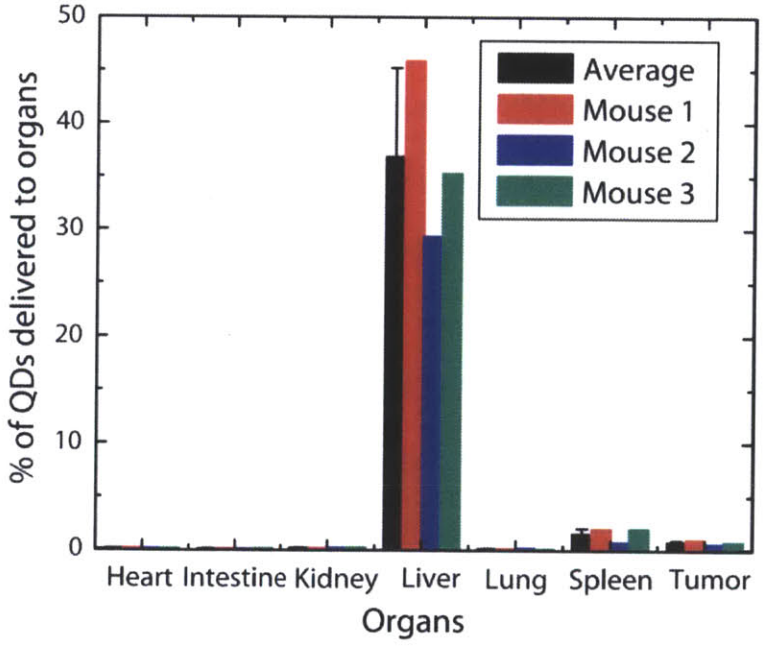

Figure 5-15 Bio distribution study of the SBPIL QDs 24 hours after the QD injection.

5.6 Conclusion

We developed a new class of polyimidazole ligands incorporating imidazole moieties for QD binding, and sulfobetaine or carboxybetaine moieties to provide water solubility and biocompatibility. Compared to traditionally used PEG composed of long repeating units of ethylene glycol, the betaine moieties of the SBPILs produce extremely compact size QDs while maintaining biocompatible behaviors. When the same size inorganic core/shell QDs were used, the betaine PIL QDs were 3.5 nm smaller in hydrodynamic diameter than the PEG PIL QDs. In addition to the small size, the strong hydration capacity of the betaine polymers via electrostatic interaction yields extremely low interaction of the SBPIL QDs with bio-environments. Nonspecific cell binding studies and nonspecific serum binding studies show that the SBPIL QDs exhibit extremely low nonspecific interaction with cells and the serum proteins. Next, biological behaviors of the SBPIL QDs were compared with that of the PEGPIL QDs to demonstrate the influence of the sulfobetaine moieties to the QD performance *in vivo* and *in vitro*. Both *in vitro* and *in vivo* studies confirm that PEG moieties are better at passivating the QD surface and repel proteins or cells from being adsorbed nonspecifically. This property of the PEG likely comes from the long and flexible nature of the PEG. We expect PEG groups on QDs exist as partially folded forms and wrap around the QD surface to physically protect the QDs. Even though PEGPIL QDs showed more stealthy nature, the SBPIL QDs also exhibited extremely low nonspecific interaction with biomolecules under optimized conditions and allowed us to perform *in vitro* targeting and *in vivo* vessel imaging studies with minimal background. Combining extraordinarily compact and biocompatible properties of the SBPIL QDs with other general properties of PIL QDs such as high QY, enhanced stability due to multidentate binding of poly

imidazole motif to QD surface and facile derivatizability, the SBPIL QDs can be widely used in biological studies well beyond the examples provided in the text.

5.7 Experimental Section

5.7.1 Materials and Instrumentation

All chemicals were purchased from Sigma Aldrich unless noted and were used as received. Alexa Fluor® 594 carboxylic acid, succinimidyl ester was purchased from Invitrogen. (1S,2S,4S)-bicyclo[2.2.1]hept-5-en-2-yl acetic acid was purchased from ChemBridge. All solvents were of reagent grade or higher and were used without further purification. All air sensitive materials were handled in an Omni-Lab VAC glove box under dry nitrogen atmosphere with oxygen levels < 0.2 ppm. All solvents were spectrophotometric grade and purchased from EMD Biosciences. All UV/vis spectra were recorded on an Agilent 8453 diode array UV/vis spectrophotometer. Photoluminescence and absorbance spectra were recorded with a BioTek Synergy 4 Microplate Reader. Flash column chromatography was performed on a Teledyne Isco CombiFlash Companion. Polymer molecular weights were determined in DMF solutions on an Agilent 1100 series HPLC/GPC system with three PLgel columns (103, 104, 105 Å) in series against narrow polystyrene standards. Molecular weights of polymers after betainization were determined in DMF solutions on an ÄKTAprime Plus chromatography system from Amersham Biosciences equipped with a self-packed Superose 12 10/300 column against BioRad Gel filtration standards. Dynamic light scattering analysis and zetapotential measurements were performed on a Malvern Instruments ZetaSizer ZS90 in a 45 μL plastic cuvette. 1H NMR spectra were recorded on a Varian Inova 500 NMR Spectrometer.

5.7.2 Synthesis

Synthesis of Monomers. ***Compound 1.*** N,N-dimethyl ethylene diamine (3.17g, 36 mmol) was added to an anhydrous THF (60mL) at 4°C. To this solution, acryloyl chloride (2.70g, 30 mmol) was injected slowly which is followed by addition of triehylamine (3.64g, 36 mmol). The solution was warmed to room temperature and stirred for 2 h. Precipitates were removed by filtration, and the solvent was evaporated in vacuo. Ethylacetate (50 mL) was added to facilitate further precipitation of reaction byproducts, and the solution was filtered once more. The crude product was purified by silica column (ethyl acetate/hexanes gradient 50:50 to 100:0, v/v) to give the pure product as a clear oil (2.59 g, 72% yield). 1H NMR (400 MHz, CDCl3): δ (ppm) 6.19 (dd, J1) 1.8 Hz, J2 = 17.0 Hz, 1H), 6.07 (dd, $J1$= 9.8 Hz, $J2$ = 17.0 Hz, 1H), 5.53 (dd, $J1$ = 1.8 Hz, $J2$ = 10.0 Hz, 1H), 3.38(dt, J1= 5.6 Hz, J2 = 5.6 Hz, 2H), 2.41 (t, 2H), 2.20 (s, 6H).

Compound 2 and 3 were synthesized as described in previous literature [4].

Typical Synthesis of Betaine PILs. All monomers were kept as dilute stock solutions between 30-100 mg/mL in ethylacetate. Stock solutions of RAFT agent (using dibenzyl carbonotrithioate) were prepared at 220 mg/mL in DMF, and AIBN was prepared at 50 mg/mL in DMF. All reagents were weighed out volumetrically. In a typical polymerization, monomers **1** (35.5 mg, 0.25 mmol) and **3** (66.3 mg, 0.25 mmol) were added to an 8 mL vial. The solvent was removed in vacuo and 50 μL of dry DMF along with RAFT agent (2.63 mg, 0.0125 mmol), and AIBN (2.05 mg, 0.0125 mmol) were added. The contents of the vial were mixed, centrifuged at 5000 $\times g$ for 2 min, and then transferred to a 1 mL ampule. The ampule was subjected to 4 cycles of freeze-pump-thaw, and sealed under vacuum using a butane torch. The vial was heated to 70 °C

on an oil bath for 3.5 h. Aliquot of the polymer solution was analyzed using GPC to determine molecular weight and poly dispersity. After confirming the polymerization is complete, the polymer solution was transferred to a 8mL vial and DMF was pulled off by vacuum, which was followed by addition of anhydrous THF (2mL) and 5 times excess of 1,3-propane sultone (152.7mg, 1.25 mmol) or β-propiolactone (108.2 mg, 1.25 mmol). Gelation occurred within 6 hours but the reaction solution was stirred 24 hours at room temperature. The pellet was washed with THF three more times to remove unreacted1,3-propanesultone or β-propiolactone. THF was removed in vacuo and 0.5 mL of a 4 M HCl in MeOH solution was added to cleave the BOC protecting groups. After 1 h at RT, the HCl was removed in vacuo. The deprotected polymer was dissolved in MeOH, to which a solution of NaOH in H_2O (5 M) was added dropwise to adjust the pH to be between 9 and 10. The solvent was removed in vacuo, and then 2,2,2-trifluoroethanol was added to precipitate the salts. The solution was filtered through a 0.45 μm PTFE filter and the solvent removed in vacuo to yield the final polymer for QD ligand exchange.

Synthesis of QDs. QDs used in this study were synthesized with modifications of previously reported syntheses as described below.

Synthesis of CdSe(CdS) QDs-QD$_{570}$. CdSe cores with a first absorption peak at 480nm were synthesized using a previously reported method [31]. The cores were precipitated with acetone three times to remove excess ligands and salts, and left overnight at 4°C before overcoating. CdS shells were deposited on CdSe cores via modification of previously reported procedures [4]. Before the shell deposition, the cores (274 nmol) were filtered with a 0.2 μM PTFE syringe filter and annealed at 220 °C in a solvent mixture of oleylamine (3 mL) and octadecene (6 mL) until no spectral shift was observed. Cd and S precursor solutions were then introduced simultaneously at 240°C over 2 hours. The Cd precursor consisted of 0.3 mmol $Cd(oleate)_2$ and

0.6 mmol oleylamine in a solvent mixture of octadecene (1.5 mL) and TOP (3 mL). The S precursor consisted of 0.3 mmol hexamethyldisilathiane [$(TMS)_2S$] in 6 mL TOP. Addition of a total of 5 monolayers of CdS yielded QDs with emission at 570 nm and a quantum yield close to unity when diluted in octane.

Synthesis of CdSe($Cd_{0.3}Zn_{0.7}S$)-QD_{612}. The synthesis follows previously reported procedures [3, 32]. The QY of the QD_{612} was 50% in octane.

Synthesis of InAs/$Cd_{0.2}Zn_{0.8}S$-QD_{750}. The synthesis follows previously reported procedures [33]. The QY of the QD_{750} was 35% in octane.

Synthesis of norbornene modified SBPIL (polymer 11). To conjugate organic dyes to QDs, primary amine monomer (monomer **10**) was incorporated to the polymer (Scheme **4**, polymer **11**). (1S,2S,4S)-bicyclo[2.2.1]hept-5-en-2-yl acetic acid (norbornene) was activated by N,N'-Diisopropylcarbodiimide and hydroxybenzotriazole in anhydrous dimethylformamide(DMF) at room temperature. The activated norbornene was reacted with polymer **11** in 1×PBS. After the reaction was completed, the reaction mixture was filtered with a 0.2 μm Tuffryn syringe filter and dialyzed with DI water 4 times through a 5kDa molecular weight cut off (MWCO) spin concentrator. After the purification, a drop of 1M NaOH was added to deprotonate the imidazole groups and water was evaporated in vacuo. Then, the polymer solution was redissolved in 2,2,2-trifluoroethanol and filtered for further ligand exchange.

Ligand Exchange. 5 mg of the betaine PILs in 2,2,2-trifluoroethanol was added dropwise to QDs in THF. After the polymer addition, we added 1mL of chloroform and 200μL of water and stirred vigorously. Less than 1 minutes after stirring, we were able to see the QDs being transferred to the water phase (supplementary fig). Then, we pipette the QD layer out pulled

vacuum to remove leftover organic solvents and redisperse the QDs in 1X PBS which was followed by three times of dialysis to get rid of excess polymers.

5.7.3 Characterizations

Measurement of Quantum yield (QY). The QY of QD570 was measured relative to Rhodamine 610 (QY 68% in ethanol) with excitation at 505 nm and QY of QD605 was measured relative to Rhodamine 640 (QY 100% in ethanol with excitation at 535nm). Solutions of QDs in octane (native CdSe/CdS QDs) or PBS (QDs after ligand exchanged with betaine PILs) and dye in ethanol were optically matched at the excitation wavelength. Fluorescence spectra of QD and dye were taken under identical spectrometer conditions in quadruplicate and averaged. The optical density was kept below 0.1 at the λ_{max}, and the integrated intensities of the emission spectra, corrected for differences in index of refraction and concentration, were used to calculate the quantum yields using the expression $QY_{QD} = (Absorbance)_{dye}/(Absorbance)_{QD} \times (Peak\ Area)_{QD}/(Peak\ Area)_{Dye} \times (n_{QD\ solvent})^2/(n_{Dye\ solvent})^2 \times QY_{Dye}$.

Gel Filtration Chromatography (GFC). GFC was performed using an ÄKTAprime Plus chromatography system from Amersham Biosciences equipped with a self-packed Superdex 200 10/100 column or Superose 6 10/300 column (to characterize QDs after ligand exchange) or Superose 12 10/300 column (to characterize betaine PILs). PBS (pH 7.4) was used as the mobile phase with a flow rate of 1.0 mL/min for Supersex 200 and Superose 12 or 0.5 mL/min for Superose 6. Typical injection volume was 100 μL. Detection was achieved by measuring the absorption at 280 nm.

Agarose Gel Electrophoresis. Electrophoresis of QDs was performed using a OWL B1A (Thermo) with 1% Omnipur agarose (EMD) in TAE (40 mM Tris-acetate, 1 mM EDTA, pH 8.3) at 7.4 V/cm for 20 min. QDs were diluted to 150 nM in TAE and mixed with 6× loading buffer (30% glycerol in H_2O) before loading onto the gel. Gels were visualized using handheld UV lamp and homemade gel imaging system.

ζ-Potential Measurement. ζ-Potential was measured on Malvern Zetasizer Nano ZS90 instrument. zeta-potentials were measured in 0.1X PBS, in a Dip Cell, with conductivities between 0.5-1 mS/cm. QD samples(5 μM) were measured in 0.1× PBS buffer. Values are reported as the average of triplicate runs consisting of 100 scans each.

Dynamic Light Scattering (DLS). Light-scattering analysis was performed using Malvern Zetasizer Nano ZS90 instrument. All QD samples were between 0.5 and 2 μM and filtered through a 0.02 μm filter before analysis. Typical count rates were between 85 and 150 kHz. The resulting ACF was fitted using the DTS (Nano) software employing a non-negative least-squares fitting algorithm. Hydrodynamic radii were obtained from a mass-weighted size distribution analysis and reported as the mean of triplicate measurements.

5.7.4 *In vitro* Experiments

Cell Culture. HeLa cells were grown in DMEM (Mediatech) with 10% Fetal Bovine Serum (Invitrogen), 50 U/mL penicillin and 50 μg /mL streptomycin (Invitrogen). For the specific labeling with the QD-SA conjugates, the cells were transfected using 1 μL Lipofectamine 2000 (Invitrogen), 0.2 μg of BirA-ER plasmid and 0.2 μg of AP-YFP-TM plasmid per well of an 8-well chamber slide (LabTek). One mM biotin was added to the media during plasmid expression.

Cells were imaged under 4 °C PBS the day after transfection. 1% Bovine Serum Albumin (Sigma) was added to block nonspecific binding during specific binding studies of ligand-coated quantum dots. Commercial BSA is known to contain biotin, and the stock BSA solution was dialyzed with a 3 kDa cutoff dialysis tube three times for 8 h in PBS pH 7.4, in 4 °C.

5.7.5 *In vivo* Experiments

Nonspecific Binding of QDs to Serum. 5μM SBPIL QD_{570} CdSe(CdZnS) (20 μL) was mixed with 100% FBS and 1× PBS to final concentrations of FBS of 20%, 50%, and 95% (referred as 100% in the main text). The mixture was incubated for 4 h at 37 °C with gentle mixing. The resultant QD size distribution was then measured using gel filtration chromatography. The mixture was injected into a Superose 6 GL10/300 column (GE Healthcare, Piscataway, NJ) on an Agilient 1100 series HPLC with an in-line degasser, autosampler, diode array detector, and fluorescence detector (Roseville, CA). PBS (pH 7.4) was used as the mobile phase with a flow rate of 0.5 mL/min and an injection volume of 50 μL. In order to selectively measure the signal from the QD rather than FBS, the fluorescence at 570nm with excitation at 300nm was measured.

Intravital Microscopy. A mixture of nanoparticles coated with PEG (570 nm emission) and betaine (612 nm emission) ligands was prepared. Concentrations were adjusted with *in vitro* calibration to result in roughly equal photoluminescence intensity for all three nanoparticle samples under 840nm multi-photon excitation. These QDs were administered intravenously using a retro-orbital injection of 200μL with the adjusted concentrations, multi-photon imaging was performed as described previously [34] on a custom-built multi-photon laser-scanning microscope using confocal laser-scanning microscope body (Olympus 300; Optical Analysis Corp.) and a broadband femtosecond laser source (High Performance MaiTai, Spectra- Physics).

Image slices were taken at ~60mW at sample surface every 2.76μm up to 201μm deep and with 2.76x2.76μm pixels. Mosaic images were taken in raster pattern using a motorized stage (H101, Prior Scientific, Inc.) and customized automation software (LabView, National Instruments). Imaging studies were performed with a 20X magnification, 0.95NA water immersion objective (Olympus XLUMPlanFl, 1-UB965, Optical Analysis).

Clearance Half-lives. *In vivo* clearance kinetics of SBPIL QDs was measured in non-tumor bearing female SCID mice. Each mouse was anesthetized with a ketamine/xylazene solution before intravenous infusion of nanoparticles by retro-orbital injection. For each time points, we collected 13μL of blood via tail vein nick and mixed this sample with 3 μL 50 mM EDTA in a plastic 96-well plate. To measure particle concentrations in the blood over time, we imaged in these samples using multiphoton microscopy to measure average intensities.

Calculation of transvascular flux. Images were analyzed using custom analysis software developed in MATLAB (The Mathworks). First, 3D vessel tracing [35] was performed to create a vascular cast and a 3D map of voxel intensity versus distance to the nearest vessel over time. Images were also corrected for sample movement over time with 3D image registration. The normalized transvascular flux was calculated using the equation:

$$\frac{J_t}{S_v(C_v - C)} = P_{eff} = \lim_{t \to 0} \frac{\partial}{\partial t} \frac{\int_{r=R}^{\infty} C(r) r \partial r}{(C_v - C)R}$$

where J_t is the transvascular flux, S_v is the vessel surface area, C_v is the concentration of the probe in the vessel, C is the concentration of the probe immediately extravascular, P_{eff} is the effective permeability [34], t is time after the initial image, r is the distance from the vessel central axis, and R is the vessel radius at that point along the vessel. Fluorescence intensities

were used as these concentrations. The calculation was made as an average over the entire imaged volume for each tumor.

***In vivo* Biodistribution Study.** *In vivo* biodistribution and tumor accumulation of the SBPIL QDs were investigated by measuring the increase of cadmium concentration in various organs after the SBPIL QD injection. The cadmium concentration was measured using inductively coupled plasma mass spectroscopy (ICP-MS). For the ICP-MS experiments, heart, kidney, lunch, liver, spleen, intestine, and tumor of mice were collected 24 hours after the retro-orbital injection of the QDs and processed as follows. First, the organs were physically homogenized using a hand homogenizer and dissolved in concentrated nitric acid (TraceSELECT® Ultra, for ultratrace analysis, Fluka) in closed vessels at 120°C for 3 days. Digestion vessels, which were made of Teflon, were cleaned before use by soaking them in 25% nitric acid for 3 days. After 3 days of heating the nitric acid with the organds, the solutions became transparent (colorless or slightly yellowish). Then, concentrated nitric acid was boiled off by opening the caps and heating the vessels at 110°C for 4 hours. After all the nitric acids were removed, 0.2% nitric acid containing 1ppb In was added and the vessels were heated to 100°C for 1 hours with the caps closed to generate the final solutions that will be used for the ICP-MS measurements. Indium was added as an internal standard since concentration of In is extremely low in live mice.

5.8 Reference

1. Bentzen EL, Tomlinson ID, Mason J, Gresch P, Warnement MR, Wright D, Sanders-Bush E, Blakely R, Rosenthal SJ: **Surface Modification To Reduce Nonspecific Binding of Quantum Dots in Live Cell Assays**. *Bioconjug Chem* 2005, **16**(6):1488-1494.

2. Ballou B, Lagerholm BC, Ernst LA, Bruchez MP, Waggoner AS: **Noninvasive Imaging of Quantum Dots in Mice**. *Bioconjug Chem* 2004, **15**(1):79-86.

3. Liu W, Howarth M, Greytak AB, Zheng Y, Nocera DG, Ting AY, Bawendi MG: **Compact Biocompatible Quantum Dots Functionalized for Cellular Imaging**. *J Am Chem Soc* 2008, **130**(4):1274-1284.

4. Liu W, Greytak AB, Lee J, Wong CR, Park J, Marshall LF, Jiang W, Curtin PN, Ting AY, Nocera DG *et al*: **Compact Biocompatible Quantum Dots via RAFT-Mediated Synthesis of Imidazole-Based Random Copolymer Ligand**. *J Am Chem Soc* 2010, **132**(2):472-483.

5. Susumu K, Mei BC, Mattoussi H: **Multifunctional ligands based on dihydrolipoic acid and polyethylene glycol to promote biocompatibility of quantum dots**. *Nat Protocols* 2009, **4**(3):424-436.

6. Howarth M, Takao K, Hayashi Y, Ting AY: **Targeting quantum dots to surface proteins in living cells with biotin ligase**. *Proc Natl Acad Sci USA* 2005, **102**(21):7583-7588.

7. Groc L, Heine M, Cognet L, Brickley K, Stephenson FA, Lounis B, Choquet D: **Differential activity-dependent regulation of the lateral mobilities of AMPA and NMDA receptors**. *Nat Neurosci* 2004, **7**(7):695-696.

8. Snee PT, Somers RC, Nair G, Zimmer JP, Bawendi MG, Nocera DG: **A Ratiometric CdSe/ZnS Nanocrystal pH Sensor**. *Journal of the American Chemical Society* 2006, **128**(41):13320-13321.

9. Choi HS, Liu W, Misra P, Tanaka E, Zimmer JP, Kandapallil B, Bawendi MG, Frangioni JV: **Renal Clearance of Nanoparticles**. *Nat Biotech* 2007, **25**: 1165-1170.

10. Holmlin RE, Chen X, Chapman RG, Takayama S, Whitesides GM: **Zwitterionic SAMs that Resist Nonspecific Adsorption of Protein from Aqueous Buffer**. *Langmuir* 2001, **17**(9):2841-2850.

11. Chen S, Zheng J, Li L, Jiang S: **Strong Resistance of Phosphorylcholine Self-Assembled Monolayers to Protein Adsorption: Insights into Nonfouling Properties of Zwitterionic Materials**. *Journal of the American Chemical Society* 2005, **127**(41):14473-14478.

12. Ladd J, Zhang Z, Chen S, Hower JC, Jiang S: **Zwitterionic Polymers Exhibiting High Resistance to Nonspecific Protein Adsorption from Human Serum and Plasma**. *Biomacromolecules* 2008, **9**(5):1357-1361.

13. Liu W, Choi HS, Zimmer JP, Tanaka E, Frangioni JV, Bawendi M: **Compact Cysteine-Coated CdSe(ZnCdS) Quantum Dots for in Vivo Applications**. *J Am Chem Soc* 2007, **129**(47):14530-14531.

14. Breus VV, Heyes CD, Tron K, Nienhaus GU: **Zwitterionic Biocompatible Quantum Dots for Wide pH Stability and Weak Nonspecific Binding to Cells**. *ACS Nano* 2009, **3**(9):2573-2580.

15. Jin Q. XJ-P, Ji J., Shen J.-C.: **Zwitterionic phosphorylcholine as a better ligand for stabilizing large biocompatible gold nanoparticles**. *Chem Commun* 2008:3058-3060.

16. Muro E, Pons T, Lequeux N, Fragola A, Sanson N, Lenkei Z, Dubertret B: **Small and Stable Sulfobetaine Zwitterionic Quantum Dots for Functional Live-Cell Imaging**. *Journal of the American Chemical Society* 2010, **132**(13):4556-4557.

17. Zhang Z, Chen S, Jiang S: **Dual-Functional Biomimetic Materials: Nonfouling Poly(carboxybetaine) with Active Functional Groups for Protein Immobilization**. *Biomacromolecules* 2006, **7**(12):3311-3315.

18. Jia G, Cao Z, Xue H, Xu Y, Jiang S: **Novel Zwitterionic-Polymer-Coated Silica Nanoparticles**. *Langmuir* 2009, **25**(5):3196-3199.

19. Yang W, Xue H, Li W, Zhang J, Jiang S: **Pursuing "Zero" Protein Adsorption of Poly(carboxybetaine) from Undiluted Blood Serum and Plasma**. *Langmuir* 2009, **25**(19):11911-11916.

20. Abraham S, So A, Unsworth LD: **Poly(carboxybetaine methacrylamide)-Modified Nanoparticles: A Model System for Studying the Effect of Chain Chemistry on Film Properties, Adsorbed Protein Conformation, and Clot Formation Kinetics**. *Biomacromolecules* 2011, **12**(10):3567-3580.

21. Amabilino DB, Feyter SD, Lazzaroni R, Gomar-Nadal E, Veciana J, Rovira C, Abdel-Mottaleb MM, Mamdouh W, Iavicoli P, Psychogyiopoulou K *et al*: **Monolayer self-assembly at liquid–solid interfaces: chirality and electronic properties of molecules at surfaces**. *Journal of Physics: Condensed Matter* 2008, **20**(18):184003.

22. Wang GM, Sandberg WC, Kenny SD: **Density functional study of a typical thiol tethered on a gold surface: ruptures under normal or parallel stretch**. *Nanotechnology* 2006, **17**(19):4819.

23. Kondoh H, Kodama C, Sumida H, Nozoyec H: **Molecular processes of adsorption and desorption of alkanethiol monolayers on Au(111)** *J Chem Phys* 1999, **111**:1175-1184.

24. Rempel JY, Trout BL, Bawendi MG, Jensen KF: **Density Functional Theory Study of Ligand Binding on CdSe (0001), (000$\bar{1}$), and (11$\bar{2}$0) Single Crystal Relaxed and Reconstructed Surfaces: Implications for Nanocrystalline Growth**. *The Journal of Physical Chemistry B* 2006, **110**(36):18007-18016.

25. Han H-S, Devaraj NK, Lee J, Hilderbrand SA, Weissleder R, Bawendi MG: **Development of a Bioorthogonal and Highly Efficient Conjugation Method for Quantum Dots Using Tetrazine–Norbornene Cycloaddition**. *Journal of the American Chemical Society* 2010, **132**(23):7838-7839.

26. HOBBS SK, MONSKY WL, YUAN F, ROBERTS YG, GRIFFITH L, TORCHILIN PT, JAIN RK: **Regulation of transport pathways in tumor vessels: Role of tumor type and microenvironment**. *Proc Natl Acad Sci* 1998, **95**:4607-4612.

27. Monsky WL, Fukumura D, Gohongi T, Ancukiewcz M, Weich HA, Torchilin VP, Yuan F, Jain RK: **Augmentation of Transvascular Transport of Macromolecules and Nanoparticles in Tumors Using Vascular Endothelial Growth Factor**. *Cancer Research* 1999, **59**:4129-4135.

28. BROWN EB, CAMPBELL RB, TSUZUKI Y, XU L, CARMELIET P, FUKUMURA D, JAIN RK: **In vivo measurement of gene expression, angiogenesis and physiological function in tumors using multiphoton laser scanning microscopy**. *NATURE MEDICINE* 2001, **7**:864-868.

29. Simionescu M, Simionescu N: **Functions of the endothelial cell surface**. *Annu Rev Physiol* 1986, **48**:279-293.

30. Silvestro L, Ruikun C, Sommer F, Duc TM, Biancone L, Montrucchio G, Camussi G: **Platelet-activating factor-induced endothelial cell expression of adhesion molecules and modulation of surface glycocalyx, evaluated `by electron spectroscopy chemical analysis**. *Semin Thromb Hemost* 1994, **20**:214-222.

31. Peng ZA, Peng X: **Formation of high-quality CdTe, CdSe, and CdS nanocrystals using CdO as precursor**. *J Am Chem Soc* 2001, **123**:183-184.

32. Snee PT, Chan Y, Nocera DG, Bawendi MG: **Whispering-Gallery-Mode Lasing from a Semiconductor Nanocrystal/Microsphere Resonator Composite**. *Advanced Materials* 2005, **17**(9):1131-1136.

33. Allen PM, Liu W, Chauhan VP, Lee J, Ting AY, Fukumura D, Jain RK, Bawendi MG: **InAs(ZnCdS) Quantum Dots Optimized for Biological Imaging in the Near-Infrared**. *J Am Chem Soc* 2009, **132**(2):470-471.

34. Brown EB, Campbell RB, Tsuzuki Y, Xu L, Carmeliet P, Fukumura D, Jain RK: **In vivo measurement of gene expression, angiogenesis and physiological function in tumors using multiphoton laser scanning microscopy**. *Nature Medicine* 2001, **7**(7):864-868.

35. Tyrrell JA, Mahadevan V, Tong RT, Brown EB, Jain RK, Roysam B: **A 2-D/3-D model-based method to quantify the complexity of microvasculature imaged by in vivo multiphoton microscopy**. *Microvascular Research* 2005, **70**(3):165-178.

Acknowledgments

The last five years have taken me on the most challenging journey of my life. I remember the day I arrived at Logan airport with two enormous bags. I was alone in a foreign country starting a new life as a graduate student. Everything was new to me from language and culture to graduate student life[1]. I have to say I was overwhelmed and somewhat scared by all the challenges waiting for me. As I have expected, conducting research as a PhD student was a solitary battle with myself. To stand as an individual scientist, I endeavored to find inspiring projects and to overcome diverse challenges, which was very different from what I was used to-studying what other people had already discovered. Even though sometimes I felt being stuck in a dark tunnel, I was fortunate to meet so many wonderful mentors, friends, and colleagues with whom I had a very fruitful and enjoyable life at MIT. With their help and support, I have grown a great deal as a person and as a scientist.

First, I was very lucky to meet an advisor who became my role model both as a scientist and a teacher. Moungi Bawendi set a good example as a calm, honest, sincere and inspiring scientist. His crisp ideas and thoroughness led his students to become good scientists. His patience and encouragement allowed us to fully explore our own interests, but at the same time he was extremely good at nudging us to focus on the big picture and stay on the right path. Lastly, I would like to thank him for his extremely generous financial and emotional support. His encouragement let me explore the diverse fields of nano-science from single molecule spectroscopy to biological applications of fluorescent nanocrystals (QDs). Even though I focused on biological aspects of QDs after the first few years, my experiences in single molecule spectroscopy contributed to my desire to study spectroscopic method development for biological imaging during my postdoc. After spending five years under his guidance, I started to think that I want to run my lab (once I get a chance), as Moungi does.

Late nights and weekends in the lab have been fun and exciting because of wonderful people in our group. As a relatively big group, we have had a variety of people with different personalities but everyone has mingled and been supported each other very well: Wen, Peter, Brian, Zoran, Jing, Dan, JM, Jenn, Jose, Darcy, Cliff, Numpon, Jongnam, Juwell, Dorthe, Tara, Raoul, Jian, Dave, Andrew, Russ, He wei, Scott, Lisa, Ou, Jie, Hao, Juan, Liang-Yi, August, Jorge, Euan, Tara, John H., Hengfen and Elisabeth. Yearly ski trips, occasional Mulan trips, and social events such as "Bawendian movie night" and "secret Santa" tied us tight and led us to build friendship rather than just being colleagues. I will remember our high-fives for "little successes" and endless encouragement from Bawendians when I had "another failed experiment." Moreover, Bawendi lab has been such a great source of knowledge. People with expertise in various fields[2] were always willing to share their intelligence. When I needed help on theoretical approach to quantum dot physics, Gautham would give me brilliant answers, when I needed help on optics, Lisa would explain physical concepts in a simple and easy manner, when I needed help on organic synthesis or dot treatments, Wen would surprise me with his skillful solutions, when I had questions about QD growth mechanisms, Peter and Dan would provide better answers than review papers, etc. Besides the students

[1] When I applied graduate schools, I decided to change my research interest from computational chemistry to experimental nano-scinece.

[2] From device and fundamental quantum theory to organic synthesis!

and postdocs, there is another important Bawendian-Li Miao who is our group administrative assistant. She always kindly shared her stories and listened to mine. I will remember our random afternoon chats, a short trip to the hippy market near Porter Square and her coming to my piano concert all the way from Malden. I really appreciate her efforts to keep our lab running smoothly.

All the work in this thesis would have not been possible without my hardworking collaborators from MGH. I will remember endless discussion on data analysis with John, never-ending mice experiments with Jayeeta and my first real biology paper about hematopoietic stem cell niches with Walid. I am very thankful for their effort and patience.

My old friends in Korea, Eugene and Minkyung, were the ones whom I called whenever I needed to chat about life and concerns about the future. As old friends, we were always on each other's side and support others struggling to achieve their dreams. Their friendship reminds me the Korean proverb "friends and wines improve with age."

Friends I met at MIT have enriched my life in graduate school. Alvin has been my music/concert partner. I have learned how to interpret and enjoy music in a more systematic manner with his elaborate explanations. Numerous concerts we have attended, impromptu piano duet gatherings, thorough music theory sessions, and endless practice for our piano duet concert at the Kresge auditorium at MIT (Rachmaninoff Suite 2) would be always remembered. His expertise in art (and of course in computer science, his major) always surprised me. It was really fun to discover the hidden beauty of artworks with him. Leeping, who was in my year in the Chemistry Department, was my weekly lunch buddy. Lunch hours with him were full of discussions on science and life. I will remember our lunches at the MS building, Mulan, Flour, etc. Most of my personal life was shared with Sungah, who is in Harvard dental school now even though she started as a graduate student at MIT with me. Because we have been going through similar stages of life and had similar personal stories, we became good friends and each other's big supporters. I will not forget the times we laughed, cried, and were serious and light-hearted together. The p-chem crew of my year-Tony, Kit, Johanna, Yogi, Eric, Barratt and Harold- has been also good companions for 5 years. By going through the same hardship-solving problem sets and having consecutive failing experiments for several years at the basement, we started to build tight bonds with each other. All-day-long grading sessions, dinners, late night parties, and White Mountain hiking trips that we have done together will be remembered as delightful memories of my graduate school life.

Much credit has to be given to Pastor Choi and Mrs. Choi for their prayer and emotional support. Their family (including Rebecca, Henry, Caleb and Steve) has become my "Boston family". They not only took a good care of me but also taught me what it is like to become a real Christian. Also, everyone in Milahl group and Stepstone Church, I appreciate your prayers and support! (Se-eun, David, Hyesung, Ha Neul, Jidam, Huisung, Dongeun, Doosuk, Seenae, pastor Kim S, pastor Hong C, Chong, etc.)

Even though Boston is on the other side of the world from Korea, there have been more than 100 people from Seoul Science High School, which made me feel less like a stranger. It was very soothing to have my old friends here: Hyung Kyoo, Sungwhan, Jungook, Semi, etc. Lunches/dinners/partying nights we had together reminded us of the good-old-days and were always refreshing. Especially, authentic Korean dinners (cooked by Sungwhan!), parties, and Tanglewood visits that I had with Sungwhan and Jaeeun were a great source of energy in my later graduate school years.

Having a cousin here also made Boston feel like my second home. Times spent with Kwan, taught me that family cannot be replaced even with close friends or a partner.

I have been lucky to meet all great roommates at the Sidney-Pacific dormitory but especially I would like to mention Michelle with whom I spent a year and half from 2009 to 2011. All our common characteristics made us very tight 'roomies'. We talked about almost everything happening in our lives and sympathized with each other. I will remember our late night chats, graduation dinner, her sweet cards and her family.

Aside from all the wonderful people, I cannot think of graduate school without music. The emerson program at MIT Music Department organized a weekly piano lesson by Hengjin Park and yearly concert for me. Hengjin introduced the beauty of Scriabin, Debussy, Ravel, Shostakovich, Prokofiev, and Bartok to me and taught me the hidden charm of Bach, Mozart, Beethoven, Liszt, etc. She opened a door that led me to a much deeper and richer world of music. I really appreciate Hengjin for her teaching and support. Musical inspiration I have got from late-night practice in the practice suite on the second floor of Building 4 helped me to keep the balance between rationality and sensibility during my PhD. I am glad that music has become my lifelong companion and has provided so much comfort and beauty in my life.

My dad, a chemistry professor, is the one who made me want to become a scientist since I was 5. His passion and enthusiasm about his job made me think that there is something special about science that makes him love his job so much. With the stories he used to tell me such as the history of chemistry, how chemists designed new materials and synthesize them, and personal history of famous scientists, I have wanted to become of a part of scientific history. Not only did he help me finding my passion in science, he also gave me endless encouragement and support during my PhD. He always showed great interest in my research and provided a great deal of comments and emotional support when I felt 'stuck'. How lucky I am to have a father who can fully understand what I am going through during my PhD! My mom and my little brother also have provided great support throughout my graduate career (and life). Their love and encouragement lifted my spirit and made me endure the hard times. As my best friend, mom always understood stressful environments I am surrounded by and reminded me that I should love and trust myself. Without having her in Boston during the last month of my PhD, writing the dessertation and preparing for the defense would have been much more difficult. It is amazing how much energy I get from her home-cooked food and the short conversations we had during the breaks.

Last but not least, I would like to thank my fiancée Gyu Weon for his kindness, support and love. The great trust he showed in me enabled me to trudge through the difficult times when I was not sure if I was good enough to take a step forward. I look forward to spending my life with him.

Thanks again to all who were there for me throughout the whole time and made my life possible up to this point. Without you this thesis would not be possible. I will remember you all.

Hee-Sun